UNIVERSIDAD POLITÉCNICA DE MADRID
Escuela Técnica Superior de Ingenieros de Telecomunicación

SAW-driven Plasmonics and Acoustoelectric Transport in Graphene

DOCTORAL THESIS

Submitted for the degree of Doctor by:

Raúl Izquierdo López
MSc in Photonics

Madrid, 2024


UNIVERSIDAD POLITÉCNICA DE MADRID
Escuela Técnica Superior de Ingenieros de Telecomunicación

Doctoral Degree in Electronic Systems Engineering

SAW-driven Plasmonics and Acoustoelectric Transport in Graphene

D O C T O R A L T H E S I S

Submitted for the degree of Doctor by:

Raúl Izquierdo López
MSc in Photonics

Under the supervision of:
Dr. Jorge Pedrós Ayala
Dr. Fernando Calle Gómez

Madrid, 2024

Title: SAW-driven Plasmonics and Acoustoelectric Transport in Graphene

Author: Raúl Izquierdo López

Doctoral Programme: Electronic Systems Engineering

Thesis Supervision:

Dr. Jorge Pedrós Ayala, Profesor Contratado Doctor, Universidad Politécnica de Madrid

Dr. Fernando Calle Gómez, Catedrático de Universidad, Universidad Politécnica de Madrid

External Reviewers:

Thesis Defense Committee:

Thesis Defense Date:

This thesis has been partially supported by Comunidad de Madrid through project NMAT2D-CM (P2018/NMT-4511) and Programa Propio UPM through Ayudas para Contratos Predoctorales 2020 and Convocatoria de ayudas dirigidas al personal investigador en formación predoctoral para realizar una estancia de investigación internacional igual o superior a tres meses 2022. This thesis has also received funding from the Spanish Ministry of Science and Innovation (MICINN) through project 2D-SAWNICS (PID2020-120433GB-I00) and from project MAD2D-CM-UPM (MRR Materiales Avanzados-UPM1) funded by Comunidad de Madrid, the Recovery, Transformation and Resilience Plan, and NextGenerationEU from the European Union.

A mi familia y amigos

"It's still magic even if you know how it's done."
Terry Pratchett

Acknowledgement

Me gustaría agradecer esta tesis, en primer lugar, a mi familia, por haber estado ahí en todo momento para lo que necesitara, tanto para celebrar los logros como para las palabras de ánimo cuando han hecho falta. También quiero agradecerles a mis directores de tesis, para empezar, por haber depositado en mi su confianza y haberme dado la oportunidad de realizar esta tesis. Además, a Jorge quiero agradecerle haberme transmitido su dedicación, su perfeccionismo y su paciencia, y a Fernando, su apoyo siempre que lo he necesitado y su motivadora visión de la ciencia.

A Alberto, quiero darle las gracias por haber conseguido que mis primeros pasos en la sala blanca fueran más fáciles, y por toda su ayuda a lo largo de la tesis. A Rajveer, por las conversaciones sobre los resultados y la planificación de los experimentos y por compartir conmigo su conocimiento. Y por supuesto, al resto de integrantes del grupo de grafeno y materiales 2D.

I would like to thank Prof. Bernhard Lendl and Dr. Andreas Schwaighofer for their hospitality during my research stay at the Technical University of Vienna (TUW) and for sharing with me their knowledge on the vibrational spectroscopy of proteins. I want to extend my gratitude to the entirety of the Chemical Analysis and Vibrational Spectroscopy group at TUW, for making me feel like another member of the team, helping me in the lab and inviting me to discover the city.

I would also like to thank Prof. Samuel Margueron and Prof. Ausrine Bartasyte from the Femto-ST Institute for providing me with thin-film lithium niobate samples, without which part of this thesis wouldn't have been possible, as well as for the advice they have offered in regard to them.

También quiero dar las gracias a los técnicos del ISOM, Manu, Jesús, Fernando, Óscar, Eli, Victoria, por asegurarse de que todo funcione a la perfección y estar siempre dispuestos a echar una mano. También a Montse e Isidoro, sin los cuales todos los trámites habrían sido mucho más difíciles. Y por supuesto, al resto de integrantes del ISOM. Especial mención a aquellos con los que he compartido buena parte del camino (Andrés, Edu, Pablo, Alejandro G, Laura, Nuño, Malte, Jovana, Lazar, Alejandro R, Rodri, Sergio, ...), por los viernes, los cafés, las tartas y las excursiones que han hecho mucho más ameno este periodo.

Por último, pero no menos importante, a mis amigos, por haber estado siempre disponibles para tomar algo, para que les dé la chapa (o para que me la den ellos), o simplemente para pasar el rato.

Esta tesis no habría sido posible sin la gente aquí mencionada y, seguramente, otros a los que posiblemente haya olvidado mencionar.

Abstract

Graphene has attracted a lot of attention since its discovery in 2004 because of its unique electronic and optical properties. Moreover, being just one atom thick, it is very sensitive to effects occurring at the surface of the substrate hosting it. This thesis explores the role of surface acoustic waves (SAWs) in piezoelectric materials as an actuator to modulate dynamically the electronic and optical properties of graphene. In particular, the acoustoelectric effect caused by the piezoelectric field of the SAW, the emergence of a pseudo-Hall voltage due to gauge fields arising in graphene because of the strain field of the SAW, and the use of the surface deformation carried by the SAW as a virtual diffraction grating to couple far-field light into surface plasmon-phonon polaritons (SPPPs) have been addressed. Two-port SAW resonators operating in the GHz frequency range with graphene Hall bars placed in between the transducers have been fabricated in LiNbO3 substrates. These devices have been used to study the acoustoelectric transport in graphene via the measurement of the acoustoelectric voltage arising in the direction of SAW propagation and of the pseudo-Hall voltage, consequence of the strain-induced pseudo-magnetic field, appearing in the direction transverse to SAW propagation. Finally, the SAW-generation and graphene electrostatic doping capabilities of alternative thin-film LiNbO3 heterostructures, obtained by wafer bonding techniques, where the metallic bonding interlayer is used as a buried electrode, have been successfully evaluated with the objective of extending the studies on the conventional and unconventional acoustoelectric transport phenomena under different graphene doping conditions. A theoretical study on the role of a SAW as a dynamic diffraction grating for the coupling of mid-infrared (mid-IR) far-field light into graphene SPPPs has also been conducted. This study has been directed towards the design and modelling of a SAW-driven plasmonic biosensor. The designed biosensor consists of a graphene/h-BN/graphene van der Waals heterostructure on a piezoelectric AlN/Al/AlN substrate. In such a structure, the hybridization of the graphene plasmons with the optically active phonons of AlN and h-BN has been exploited to probe the fingerprinting region of organic compounds, whereas the buried Al electrode enables the field-effect gating of graphene with the top AlN layer as a gate dielectric, which permits to tune the SPPP frequency. A theoretical model based on coupled harmonic oscillators has been developed to quantify the interaction of the SPPP with the vibrational resonances of the analytes, even if this interaction is too faint to induce a Fano resonance. The combination of the designed biosensor and the coupled oscillators model has proven to allow fingerprinting ultrathin biolayers down to the monolayer limit, as shown for significant biological substances such as an A/G-IgG protein bilayer or a VGA peptide monolayer. Finally, a home-built mid-IR spectroscopy and mapping setup based on quantum cascade lasers (QCLs) and a photoconductive HgCdTe detector has been designed, assembled, and tested. ZnSe refractive optics have been used to focus the 4-millimeter diameter beam of the QCLs into a 15-micron-size spot on the surface of the sample. Moreover, a motorised stage has been included to not only record single spectra but also full spectral maps. A Python script has been developed to coordinate the different elements of the setup, allowing in-phase optical measurements with a lock-in amplifier. This setup will contribute to the development of novel graphene-based plasmonic devices such as the designed biosensor.

Resumen

El grafeno ha atraído una gran atención desde su descubrimiento en 2004 debido a sus singulares propiedades electrónicas y ópticas. Además, con un grosor de un solo átomo, es muy sensible a los efectos que tienen lugar en la superficie el sustrato sobre el que se encuentra. Esta tesis explora el papel de las ondas acústicas de superficie (SAWs) en materiales piezoeléctricos como actuadores para modular dinámicamente las propiedades electrónicas y ópticas del grafeno. En concreto, se ha tratado el efecto acustoeléctrico causado por el campo piezoeléctrico de la SAW, la aparición de un voltaje pseudo-Hall resultante de los campos gauge que aparecen en grafeno debidos al campo de deformación mecánica de la SAW y el uso de la corrugación de la superficie producida por la SAW como una red de difracción virtual para acoplar luz de campo lejano a polaritones de plasmón-fonón superficial (SPPPs). Se han fabricado resonadores SAW de dos puertos operando en el rango de los GHz, con barras Hall de grafeno situadas entre los transductores, sobre sustratos de LiNbO3. Estos dispositivos se han utilizado para estudiar el transporte acustoeléctrico en grafeno a través de la medida del voltaje acustoeléctrico que aparece en la dirección de propagación de la SAW, y del voltaje pseudo-Hall que aparece en la dirección transversal a la propagación de la SAW, debido al campo pseudo-magnético inducido por la deformación. Finalmente, se han evaluado con éxito la capacidad para generar SAWs y para el dopaje electrostático del grafeno en heteroestructuras alternativas basadas en capas finas de LiNbO3 obtenidas mediante técnicas de wafer bonding, todo ello con el objetivo de extender los estudios acerca del transporte acustoeléctrico convencional y no convencional con distintos niveles de dopaje del grafeno. Se ha realizado un estudio teórico del uso de una SAW como red de difracción dinámicas para el acoplo de luz de campo lejano a SPPPs en el infrarrojo medio (MIR). Este estudio se ha orientado hacia el diseño y modelado de un biosensor plasmónico activado por SAWs. El biosensor diseñado consiste en una heteroestructura de van der Waals de grafeno/h-BN/grafeno sobre un sustrato piezoeléctrico de AlN/Al/AlN. En dicha estructura, se ha aprovechado la hibridación de los plasmones del grafeno con los fonones ópticamente activos del AlN y del h-BN para acceder al rango donde se encuentra la huella infrarroja de los compuestos orgánicos, mientras que el electrodo de Al enterrado habilita el dopaje por efecto campo del grafeno, utilizando la capa superior de AlN como dieléctrico de puerta, lo que permite ajustar la frecuencia del SPPP. Se ha desarrollado un modelo teórico basado en osciladores armónicos acoplados para cuantificar la interacción del SPPP con las resonancias vibracionales de los analitos, incluso cuando esta interacción es demasiado débil para inducir una resonancia de Fano. La combinación del biosensor diseñado con el modelo de osciladores acoplados ha demostrado la posibilidad de identificar capas orgánicas ultrafinas hasta el límite de la monocapa, como se muestra en casos de sustancias biológicas significativas como una bicapa de proteínas A/G-IgG o una monocapa de péptido VGA. Finalmente, se ha diseñado, construido y probado un sistema de espectroscopía y mapeo en el MIR basado en láseres de cascada cuántica (QCLs) y un detector fotoconductivo de HgCdTe. Se han utilizado componentes ópticos refractivos de ZnSe para focalizar el haz de salida de los QCLs, de 4 milímetros de diámetro, en un spot de 15 micras en la superficie de la muestra. Además, se ha incluido un soporte motorizado que permite adquirir, además de espectros individuales, mapas espectrales. Se ha desarrollado un programa en Python para coordinar los distintos elementos del sistema, posibilitando medidas ópticas en fase mediante un amplificador lock-in. Este

sistema contribuirá al desarrollo de novedosos dispositivos plasmónicos basados en grafeno como el biosensor diseñado.

Table of Contents

List of Figures

List of Tables

Abbreviations and acronyms

2DEG 2-Dimensional Electron Gas

2DHG 2-Dimensional Hole Gas

A/G-IgG A/G protein and goat anti-mouse inmunoglobulin (A/G-IgG) bilayer

CBP 4,4'-bis(N-carbazolyl)-1,1'-biphenyl

CNP Charge Neutrality Point

COM Coupled Oscillators Model

CVD Chemical Vapour Deposition

DFB Distributed Feedback

DFB-QCL Distributed Feedback Quantum Cascade Laser

DIW Deionized Water

DLG Double Layer Graphene

EBL Electron Beam Lithography

EC-QCL External Cavity Quantum Cascade Laser

FET Field-Effect Transistor

FEUDT Floating Electrode Unidirectional Transducer

FOM Figure of Merit

FTIR Fourier Transform Infrared

GS Ground-Source

GSG Ground-Source-Ground

HPPP Hyperbolic Plasmon-Phonon Polariton

IDT Interdigital Transducer

IPA Isopropyl alcohol / Isopropanol

IV Current-Voltage

MCT Mercury Cadmium Telluride

ML Monolayer

MP Magnifying Power

NMP N-methyl-2-pyrrolidone

PEC Proximity Effect Correction

PMMA Polymethyl Methacrylate

PSF Point Spread Function

RF Radiofrequency

Q Quality factor

QCL Quantum Cascade Laser

SAW Surface Acoustic Wave

SEIRA Surface Enhanced Infrared Absorption

SEM Scanning Electron Microscope

SLG Single Layer Graphene

SOLT Short Open Load Through

SPA Semiconductor Parameter Analyzer

SPP Surface Plasmon Polariton

SPPP Surface Plasmon-Phonon Polariton

TLM Transmission Line Method

TMM Transfer Matrix Method

TTI Triple Transit Interference

VGA Valine Gramicidin A

VNA Vector Network Analyzer

Chapter 1

Introduction

Graphene is a two-dimensional (2D), one-atom thick semimetallic material with exotic properties such as chiral Klein tunnelling (Katsnelson et al., 2006), which contributes to the large carrier mobility of graphene, or the quantum Hall effect (Novoselov et al., 2005), which appears even at room temperature (Novoselov et al., 2007). Moreover, its intrinsic 2D nature makes graphene a perfect 2D electron (hole) gas (2DE(H)G), extremely well-suited for transport and electron correlation studies. In the field of optics, as a conductive material, graphene supports surface plasmon polariton resonances (Low and Avouris, 2014), which are located in the mid-infrared region of the electromagnetic spectrum. In addition, because of the reduced thickness of this material, its electronic and optical properties are strongly influenced by mechanical deformations of the substrate below them (Fandan, 2020). Thus, this thesis is focused on the use of surface acoustic waves (SAWs) for the modification of the electron transport and optical properties of graphene. In this chapter, the state of the art in graphene, SAWs, plasmonics, and the effects that SAWs cause on 2D materials are described.

1.1 State of the Art

1.1.1 Graphene

Graphene is an allotrope of carbon composed by a one atom-thick hexagonal structure of carbon atoms with a separation a of 1.42 Å between them. This hexagonal structure is made out of two interpenetrating triangular lattices. The structure can also be seen as a triangular lattice with a basis of two atoms per unit cell. After a tight binding analysis (Neto et al., 2009; Sarma et al., 2011), it can be found that the dispersion around the K and K' points, the inequivalent corners of the Brillouin zone at $(\frac{2\pi}{3a}, \frac{2\pi}{3\sqrt{3}a})$ and $(\frac{2\pi}{3a}, -\frac{2\pi}{3\sqrt{3}a})$ respectively, yields

$$E_{\pm}(q) = \pm\hbar v_F|q| + O(q^2), \tag{1.1}$$

where the +(-) sign refers to the conduction (valence) band, q = k - K is the distance to the K point in the reciprocal space and $v_F = 3a\Delta/2\hbar \sim 10^6$ m/s the Fermi velocity, being $\Delta = 2.8$ eV the nearest-neighbour hopping energy. This dispersion implies a semimetallic behaviour

of the material, since the valence and conduction bands converge at the K and K' points. Furthermore, the dispersion relation is linear in the vicinity of these points, which means that, if the effective mass of the charge carriers is described as $m^* = (\frac{1}{\hbar^2}\frac{\partial^2 E}{\partial q^2})^{-1}$, the charge carriers behave as massless fermions that follow the Dirac equation. Thus, the K and K' points are often referred to as Dirac points, and the energy-momentum dispersions around them are called Dirac cones. These Dirac points are often defined as the energy reference of the system (E(K)=E(K')=0 eV). At thermal equilibrium, the Fermi level of graphene is located at the Dirac point, thus the Fermi energy is $E_F = 0$ eV, and the intrinsic carrier concentration of graphene is:

$$n_i = p_i = \frac{\pi}{6}(\frac{k_B T^2}{\hbar v_F})^2, \tag{1.2}$$

where k_B is the Boltzmann constant and T is the temperature. At room temperature, the intrinsic carrier density yields $n_i, p_i \sim 9 \times 10^{10} cm^{-2}$ (T. Fang et al., 2007). Moreover, graphene is known to show a remarkable field effect when placed on an insulator/conductor structure, allowing the electrostatic tuning of its Fermi energy, even switching between electron and hole transport (Novoselov et al., 2004, 2005). This process is illustrated in Figure 1.1. Applying a gate voltage V_G between the graphene and the bottom conductor, a surface charge density is induced in the graphene sheet that shifts its Fermi level. This system can be modelled as a parallel plate capacitor, and the charge density at the surface follows:

$$n = \frac{1}{A}\frac{Q}{e} = \frac{1}{A}\frac{CV_G}{e} = \frac{\varepsilon_0 \varepsilon}{de} V_G, \tag{1.3}$$

where A, d and Q are the area, the distance between the plates and the charge stored in the capacitor, C its capacitance, V_G the gate voltage applied to the system, e the electron charge, and ε_0 and ε are the permittivity of vacuum and the relative permittivity of the insulator, respectively.

The typical structure for the electrostatic modulation of graphene consists of a 300-nm-thick SiO_2 layer on doped Si, which also provides a good visibility of the graphene sheet. For this structure, the induced carrier density calculated by Equation 1.3 results in $n = 7.2 \times 10^{12} cm^{-2}$ for a gate voltage of 100 V.

However, the charge neutrality point (CNP) is generally not at $V_G = 0$ V, since graphene usually presents adsorbed residues of substances used during the transfer process, such as water, acetone, or polymers. These compounds typically give a p-doped character to graphene and therefore the CNP is usually located at positive V_G values (if the biasing scheme in Figure 1.1 is followed).

1.1.2 Surface Acoustic Waves

Acoustic Waves in Elastic Media

In elastic solids, the displacement ($\mathbf{u} = u_x\hat{x} + u_y\hat{y} + u_z\hat{z}$) of a single particle induces a disturbance that propagates in the medium, just as if the material were composed of point

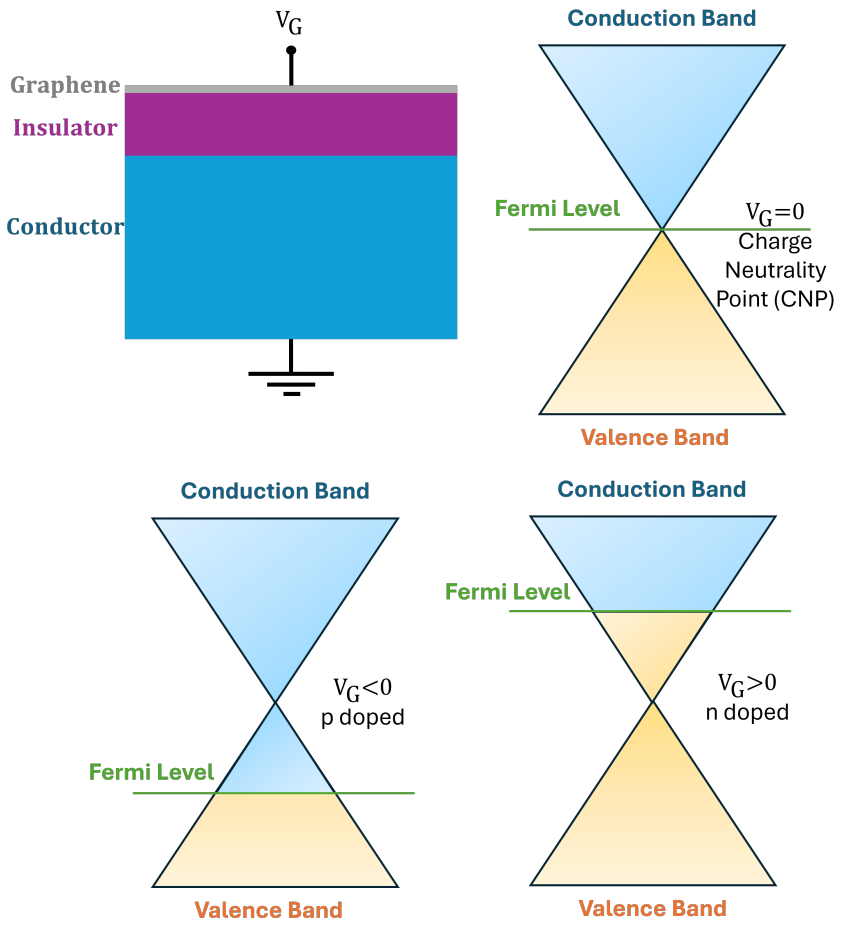

Figure 1.1: Illustration of the electrostatic doping of graphene and its effect on the Fermi level modulation across the carrier energy-momentum dispersion.

masses linked by springs. In order to get rid off the contributions to displacement from mere traslation of the solid, the displacement gradient matrix can be defined:

$$\nabla \mathbf{u} = \begin{pmatrix} \frac{\partial u_x}{\partial x} & \frac{\partial u_x}{\partial y} & \frac{\partial u_x}{\partial z} \\ \frac{\partial u_y}{\partial x} & \frac{\partial u_y}{\partial y} & \frac{\partial u_y}{\partial z} \\ \frac{\partial u_z}{\partial x} & \frac{\partial u_z}{\partial y} & \frac{\partial u_z}{\partial z} \end{pmatrix}. \tag{1.4}$$

Now, this matrix contains information about both the interparticle displacement and local rotations. By adding its transpose to it, the latter contribution is cancelled out, leading to the strain tensor $\mathbf{S}$, whose elements are defined by:

$$S_{ij} = \frac{1}{2}\left(\frac{\partial u_i}{\partial x_j} + \frac{\partial u_j}{\partial x_i}\right). \tag{1.5}$$

Therefore, strain can be defined as the change in length of the material per unit length as a consequence of applied stress. In addition, stress is defined as the force per unit area applied

to an infinitesimal volume of material. In the limit of small deformations, the relation between stress and strain is linear and can be represented by the stress tensor $\boldsymbol{T}$:

$$T_{ij} = \sum_{k,l=1}^{3} c_{ijkl} S_{kl}, \tag{1.6}$$

where c_{ijkl} are the elastic stiffness coefficients (Ballantine, 1997). In 1D, this relation is equivalent to Hooke's law.

The propagation modes allowed by such kind of system strongly depend on the boundary constraints of the material, since the displacement of a particle surrounded by other particles is not equivalent to that of a particle in a boundary. Therefore, different modes exist depending on the boundaries of the material, such as bulk waves (propagate in the bulk of the material unaffected by boundaries), surface waves (confined to the surface of the material) or plate waves (confined to a slab of material), as illustrated in Figure 1.2.

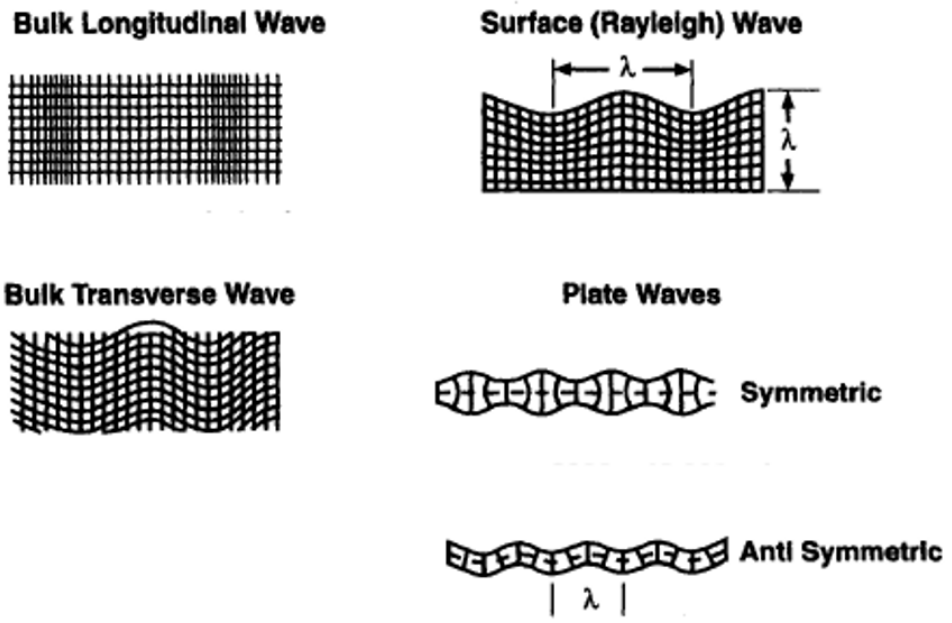

Figure 1.2: Types of propagating waves in a solid depending on the boundaries they encounter. Extracted from Ballantine, 1997.

Rayleigh Waves

Rayleigh waves are a kind of SAW that were first mathematically described by Lord Rayleigh (Rayleigh, 1885). In Rayleigh waves, particles follow an elliptical motion, which can be mathematically described by:

$$\mathbf{u}(x,z,t) \approx u_0 e^{i(\omega t - kx)} e^{-k|z|}, \tag{1.7}$$

where u_0, ω and k are the amplitude, frequency and wavenumber of the wave, respectively (C. K. Campbell, 1998), x is the propagation direction, and z is the direction perpendicular to the surface. From this equation, it is clear that the displacement produced by SAWs is exponentially attenuated with depth, decreasing by a factor of 1/e at one wavelength distance. These waves are commonly studied in geophysics (Foti, 2015), although they can also be artificially generated. There are different ways to generate SAWs with a plane wavefront, such as optical generation through photothermal processes produced by laser interference (Smith et al., 2014), photomask imaging (Harata et al., 1990), or light impinging on a metallic grating (Matsuda et al., 2020), where light absorption produces local heating and thus thermal expansion of the material; or through the transduction of electrical signals in piezoelectric substrates. In the latter case, since the deformation of the material creates an electric field, a propagating wave piezoelectric potential Φ arises from the SAW propagation, in a similar manner to the displacement wave described in Equation 1.7:

$$\Phi(x,z,t) \approx |\Phi| e^{i(\omega t - kx)} e^{-k|z|}. \tag{1.8}$$

This potential, unlike the particle displacement, is not confined to the surface, but rather extends out of the piezoelectric material. Moreover, the gradient of the piezoelectric potential produces a piezoelectric field that propagates together with the strain field of the SAW.

Interdigital Transducers

For the generation of SAWs on piezoelectric materials, interdigital transducers (IDTs, Voltmer and White, 1965) are used. They consist of two periodic gratings of metallic contacts, each of them with a period of the desired SAW wavelength, intertwined between them. Then, one of the gratings is grounded and a radiofrequency (RF) signal is applied with respect to this ground level on the other grating. Consequently, an electric field periodic in space and time is applied to the piezoelectric crystal, resulting in a deformation periodic in space and time. If this deformation matches the energy-momentum relation of a SAW mode, the deformation propagates along with its corresponding piezoelectric field. The efficiency in the energy conversion from the electrical signal to the SAW is determined by the electromechanical coupling coefficient (K^2) of the substrate, which depends on the piezoelectric coefficient, Young modulus and dielectric permittivity of the piezoelectric material.

Regular IDTs are bidirectional, which means that both forward- and backward-propagating SAWs are generated. This can be beneficial when using IDTs as RF electronic components, but for other applications it may be convenient that all the SAW power is directed in the same sense. A way of achieving this is the use of floating electrode unidirectional transducers (FEUDTs,Yamanouchi and Furuyashiki, 1984), in which one or more electrodes are not connected to either bus bar. These devices generate a unidirectional SAW, but limit the operation frequency because the minimum feature size that has to be fabricated for a specific wavelength is several times smaller than for a standard IDT. Another way consists in combining

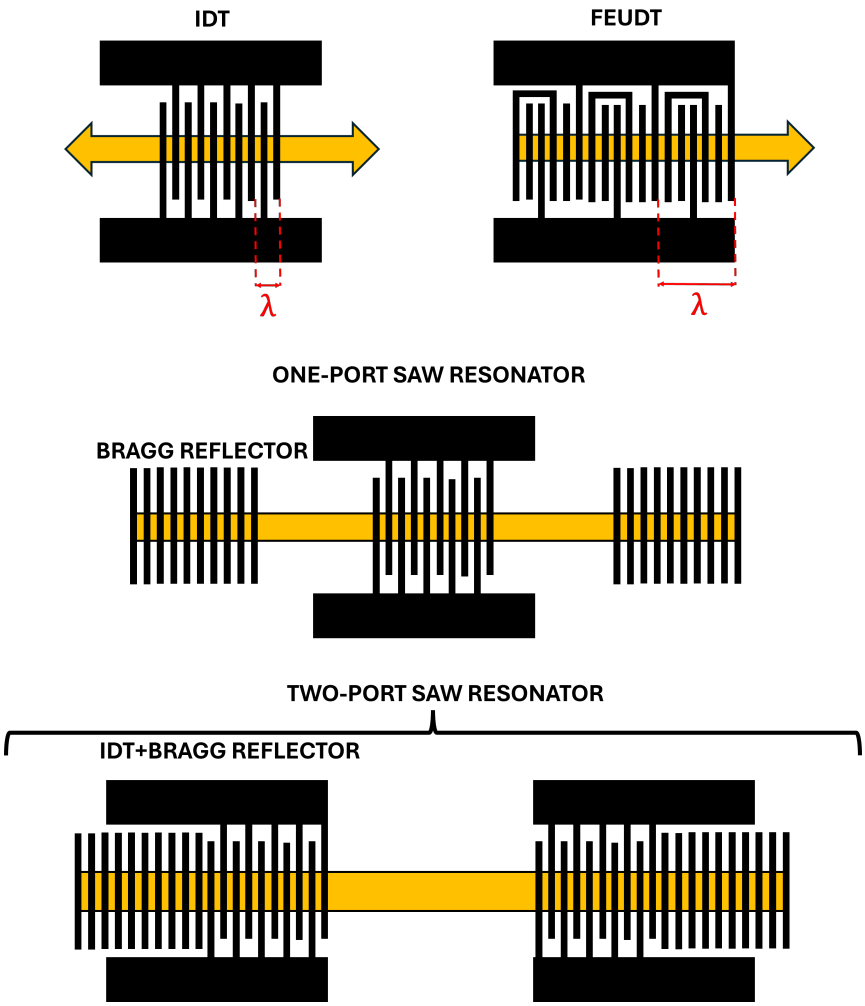

Figure 1.3: Illustration of an IDT, a FEUDT, a one-port SAW resonator formed by an IDT and two sets of Bragg reflectors and a two-port SAW resonator formed by two IDTs with Bragg reflectors.

the bidirectional IDT with a reflector behind it. For that, Bragg reflectors are usually chosen, since they suppress waves traversing the reflector through destructive interference, whereas the interference of the reflected waves is constructive. These reflectors, widely used in optics as dielectric mirrors (Saleh and Teich, 2019), are implemented in SAW devices in the form of an array of metallic electrodes with a period of half the SAW wavelength (Morgan, 2007). The number of reflector elements in the grating necessary to achieve total reflection depends on the electromechanical coupling coefficient of the material (C. K. Campbell, 1998). Alternatively, the metallic electrodes can be substituted by grooves etched in the substrate, which can then be left empty or filled with metal.

Moreover, a two-port SAW resonator can be built by placing two IDTs emitting towards each other. If both IDTs have a Bragg reflector behind them, a SAW cavity is built. This cavity can generate standing SAWs, which present a higher amplitude than the propagating ones, resulting from the constructive interference of the counterpropagating SAWs emitted by each

IDT. Standing SAWs can also be generated by one-port resonators, with the IDT enclosed between two Bragg reflectors. Figure 1.3 shows an illustration of the different types of SAW transducers mentioned above.

1.1.3 Mid-IR Surface Plasmon Polaritons

Mid-IR Spectroscopy

The mid-infrared (mid-IR) range (3-20 μm wavelength) is of great importance for the spectroscopy of organic compounds since it contains the vibrational fingerprints of the functional groups that form organic molecules, that is, the set of absorption resonances related to the molecular bonds that uniquely identify a substance. Figure 1.4 shows an example of the vibrational resonances that can used to identify different kinds of compounds. Furthermore, the position and relative intensity of these resonances can be used to infer the conformation of the molecules. In the case of proteins and peptides, the mid-IR range gives access to their secondary structure, as well as to local interactions, adsorption or binding processes in a label-free manner (Barth, 2007; López-Lorente and Mizaikoff, 2016). As a result, a multitude of different techniques have been developed to access this region of the electromagnetic spectrum. Examples of these techniques are vibrational circular dichroism (VCD) (Nafie et al., 1976; Lüdeke et al., 2011), infrared reflection absorption spectroscopy (IRRAS) (Mendelsohn et al., 2010), Fourier transform infrared (FTIR) spectroscopy, in transmission or reflection configurations, with or without a prism to perform attenuated total reflectance (ATR) measurements (Mirabella, 1985). Interferometric measurement schemes have also been implemented in different studies, using Mach-Zehnder interferometers to record absorption or dispersion of compounds (Hayden et al., 2018) or measuring photothermally-induced phase shifts (Kristament et al., 2018). Furthermore, indirect measurements can also be acquired using nanospectroscopy techniques such as AFM-IR (Dazzi and Prater, 2017).

However, sensing ultrathin biolayers is challenging because of the low absorption cross section resulting from the strong size mismatch between the free radiation (wavelength $\sim \mu$m) and the biomolecules (size $\sim$ nm). This limitation can be overcome using surface plasmon polaritons (SPPs).

Graphene Surface Plasmon Polaritons

SPPs are modes of electromagnetic radiation that are spatially confined at the interface between a conductor and a dielectric. They originate from the coupling between light and collective electron oscillations and present a shorter wavelength than the free space light that generate them. As a result, their mode volume is smaller and thus exhibit a higher electric field intensity that strengthens light-matter interactions at the nanoscale, being the principle of surface-enhanced infrared absorption (SEIRA) spectroscopy (Adato and Altug, 2013; Neuman et al., 2015; Yi et al., 2020).

Traditionally, metals have been used to generate SPPs, but in recent years, graphene has emerged as a prominent SEIRA platform that supports SPPs in the mid-IR range, providing much greater confinement factors than metals, due to its 2D nature, while maintaining long lifetimes (Li et al., 2014; Rodrigo et al., 2015; H. Hu et al., 2016; Lee et al., 2019). Moreover,

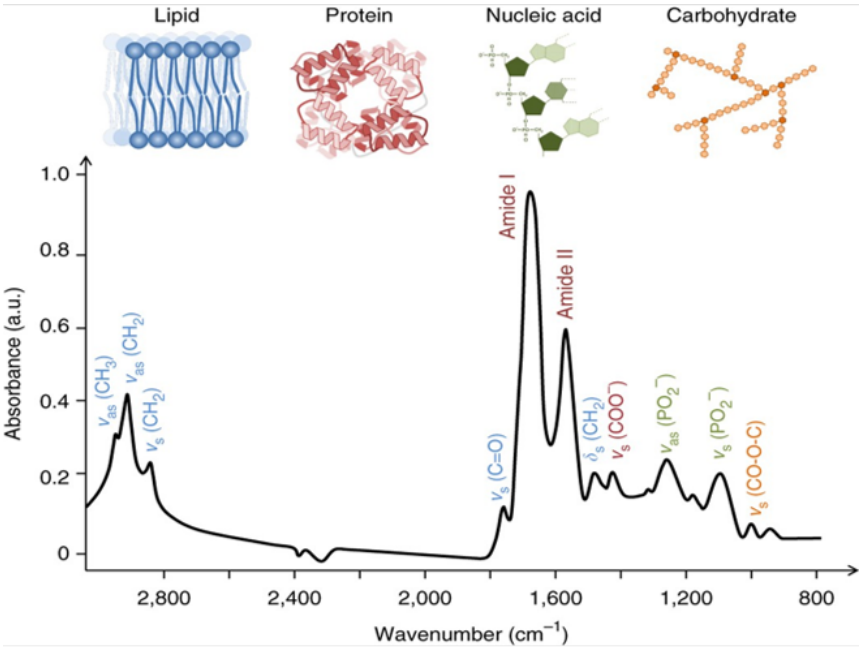

Figure 1.4: Mid-IR spectrum containing the vibrational resonances that identify different kinds of biological compounds. The spectrum, extracted from Baker et al., 2014, was acquired from a human breast carcinoma.

as opposed to metals, its carrier density can be tuned electrically, allowing to modulate the SPP frequency. On the other hand, charge carriers can interact with the surface phonons of polar substrates through the Fröhlich coupling, leading to hybridisation into SPPPs. This hybridisation can increase the polariton lifetime when graphene is stacked with other polar 2D dielectric materials such as hexagonal boron nitride (h-BN) (Brar et al., 2013; Fandan et al., 2018), or polar substrates (Schiefele et al., 2013).

However, the shorter wavelength of SPP modes implies a momentum mismatch with free-space light. Therefore, the extra momentum necessary to couple both modes needs to be provided with some other mechanism. In metals, it is common to use dielectric prisms in contact with the conductor/dielectric structure. Since the velocity of light is smaller within the prism than in air, the momentum k of the light in the prism and that of the SPP can be matched for some specific incidence angle θ, so that (Maier, 2007):

$$k = \frac{\omega}{c} n_p \, sin\theta, \tag{1.9}$$

where ω and c are the frequency and velocity of light, respectively, and n_p is the refractive index of the prism.

Since graphene SPPs manifest a wavelength even shorter than that of metal plasmons, the momentum that needs to be supplied is larger than the one that can be provided by a prism. Therefore, coupling light into graphene SPPs (or SPPPs) typically requires either complex near-field techniques (Fei et al., 2011; Zhang et al., 2022) or patterning nanostructures such

as diffraction gratings (Ju et al., 2011; Brar et al., 2013; Z. Fang et al., 2014), with the latter restricted to the excitation of localised plasmons where edge scattering reduces the plasmon lifetime.

1.1.4 Effects of SAWs in Graphene

Acoustoelectric Effect

The acoustoelectric effect resulting from the interaction of SAWs with charge carriers in metals and semiconductors was first described by Parmenter, 1953. Later on, studies both theoretical (Ingebrigtsen, 1970) and experimental have been performed on the acoustoelectric effect resulting from the interaction between SAWs and a 2-dimensional electron gas (2DEG) in AlGaAs/GaAs structures either standalone (Shilton et al., 1995; Simon, 1996) or transferred onto $LiNbO_3$ (Rotter et al., 1998) to benefit from the high electromechanical coupling of this piezoelectric substrate. This effect presents two facets, depending on how it affects the SAWs or on how it affects the charge carriers.

From the SAW point of view, energy and linear momentum are transferred to the carriers, resulting in an attenuation α of the SAW amplitude and in a velocity shift in the SAW propagation Δv, respectively. Both effects are well described in the aforementioned studies by the equation:

$$\frac{\Delta v}{v_0} - i\frac{\alpha}{q} = \frac{K^2/2}{1 + i\sigma_{xx}/\sigma_M}, \tag{1.10}$$

where σ_{xx} is the conductivity of the 2DEG, $\sigma_M = (\varepsilon_1 + \varepsilon_2)v_0$ is a parameter that depends on the dielectric permittivities of the surrounding media (ε_i), and v_0 is the SAW velocity when $\sigma_{xx} \to \infty$. Figure 1.5 shows the velocity shift and the SAW attenuation described in Equation 1.10 as a function of the conductivity.

These same effects have been reported in graphene. Moreover, since the conductivity of graphene can be modified *in situ*, different attenuation regimes can be explored (Bandhu and Nash, 2016). Furthermore, carriers in motion can also transfer their energy to the SAWs, resulting in SAW amplification when they drift in the same direction and sense as the SAW and with a drift velocity larger than the velocity of the SAW. This has been reported in both semiconductor materials (Hutson et al., 1961; Collins et al., 1968), even obtaining a net gain of the signal through the delay line (Hackett et al., 2023), and graphene (Carmichael et al., 2018; Insepov et al., 2015).

With regard to the effect on the carriers, the transfer of energy and momentum from the SAW results in the emergence of an acoustoelectric current in the semiconductor. This current can be measured in a short-circuit configuration, although an acoustoelectric voltage can also be measured between the contacts. In graphene, this was first measured by Miseikis et al., 2012, where the acoustoelectric current I_{AE} was reported to have a linear dependence on the SAW power P_{SAW}, as experimentally found by Shilton et al., 1995 and Rotter et al., 1998 and theoretically predicted by Ingebrigtsen, 1970:

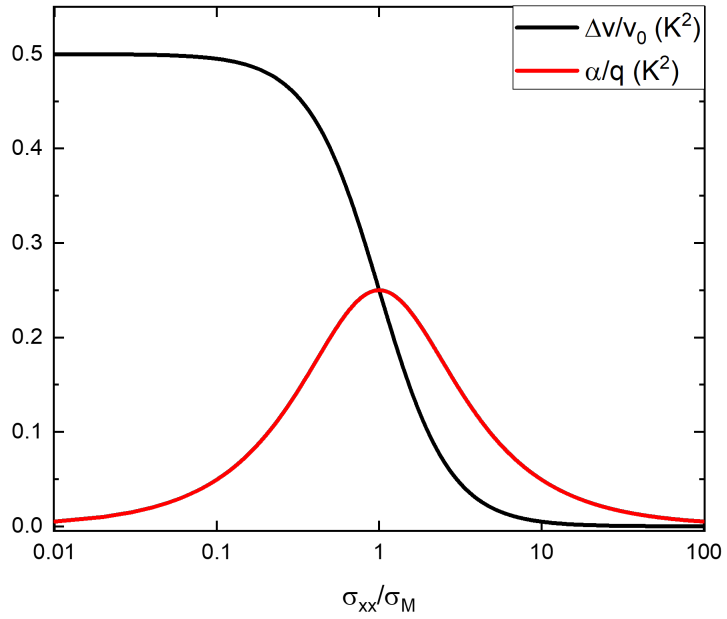

Figure 1.5: Velocity shift and SAW attenuation as a function of the conductivity according to Equation 1.10.

$$I_{AE} = -\mu \frac{P_{SAW}}{v_0} \alpha, \tag{1.11}$$

where μ is the carrier mobility. This trend has been consistently reproduced in other works (Bandhu et al., 2013; Hernández-Mínguez et al., 2016; Costanza et al., 2023). Moreover, according to Equation 1.10, which indicates that the attenuation is proportional to the wavevector, the acoustoelectric current will be linearly dependent on the wavevector of the SAW (Hernández-Mínguez et al., 2018).

The dependence of the acoustoelectric current in graphene on its conductivity has also been studied. As shown in Bandhu and Nash, 2016, when the gate voltage is swept from large values (either positive or negative) toward the CNP, the acoustoelectric current increases in the same way as the velocity shift and the attenuation, since there is an energy and momentum exchange between the SAW and the carriers. The maximum attenuation is reached, according to Equation 1.10 and as shown in Figure 1.5, at a gate voltage value such that the conductivity of graphene is equal to σ_{M}, and, if the voltage is swept to cross the CNP, the acoustoelectric current changes sign, as the carriers change polarity.

Strain-Induced Gauge Fields

Strain can be considered in the tight binding model of graphene as a change in the electron hopping energy and the lattice parameter, which leads to the emergence of a gauge vector

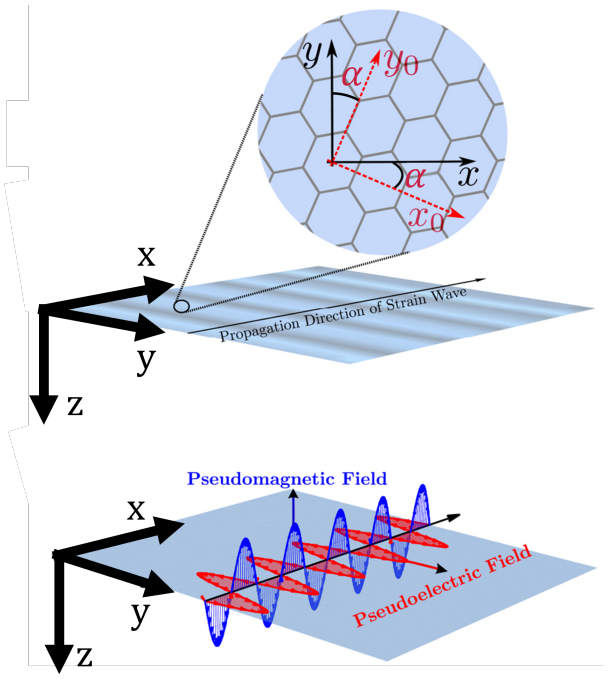

Figure 1.6: Illustration of the gauge fields in graphene under the action of a strain wave. Extracted from Oliva-Leyva and Naumis, 2016, with the axes renamed to keep the notation of the thesis.

potential $\mathbf{A_S}$ resulting in pseudo-magnetic and pseudo-electric fields (Guinea et al., 2008; Vozmediano et al., 2010; Naumis et al., 2017), as illustrated in Figure 1.6. Regarding the pseudo-magnetic field $\mathbf{B_S}$, only its out-of-plane (z) component can affect the transport of charge carriers across a graphene channel. Thus:

$$\mathbf{B_S} = \nabla \times \mathbf{A_S} \Rightarrow B_{Sz} = \frac{\partial A_{Sy}}{\partial x} - \frac{\partial A_{Sx}}{\partial y}, \tag{1.12}$$

while the pseudo-electric field can be calculated as:

$$\mathbf{E_S} = -\frac{\partial \mathbf{A_S}}{\partial t}. \tag{1.13}$$

Moreover, following Zhai et al., 2010 and Sela et al., 2020, the components of $\mathbf{A_S}$ are related to the components of the strain tensor S_{ij} by:

$$\begin{pmatrix} A_{Sx} \\ A_{Sy} \end{pmatrix} = \frac{\Delta}{ev_F} \frac{d(\ln \Delta)}{d(\ln a)} \begin{pmatrix} \cos 3\alpha & \sin 3\alpha \\ -\sin 3\alpha & \cos 3\alpha \end{pmatrix} \begin{pmatrix} S_{xx} - S_{yy} \\ -2S_{xy} \end{pmatrix}, \tag{1.14}$$

being e the electron charge, v_F the Fermi velocity of graphene, and α the angle between the y direction and the armchair direction of graphene. Therefore, the pseudo-magnetic field emerging in strained graphene follows:

$$B_{Sz} = (\frac{\partial^2 u_y}{\partial y^2} - \frac{\partial^2 u_y}{\partial x^2} - 2\frac{\partial^2 u_x}{\partial x \partial y})\cos 3\alpha + (\frac{\partial^2 u_x}{\partial y^2} - \frac{\partial^2 u_x}{\partial x^2} + 2\frac{\partial^2 u_y}{\partial x \partial y})\sin 3\alpha. \tag{1.15}$$

Hence, it is evident that a strain gradient is needed in order to generate a pseudo-magnetic field in graphene. Moreover, several experimental studies on graphene strained in various ways have shown the appearance of quantised Landau levels in strained graphene even in absence of an external magnetic field. Hence, Levy et al., 2010 reported pseudo-magnetic fields with magnitudes greater than 300 T in graphene nanobubbles grown by chemical vapour deposition (CVD) on a platinum substrate. Yeh et al., 2011 studied the emergence of Landau levels via scanning tunnelling microscopy in naturally occurring ripples in graphene grown by chemical vapour deposition on copper foil, that are heavily attenuated when transferring graphene to a SiO_2 substrate. In a similar experiment, Kang et al., 2021 described pseudo-magnetic fields of up to 100 T in an optical pump-probe experiment on CVD graphene transferred to a substrate with an array of nanopillars on its surface, which creates a non-uniform strain pattern in graphene. This strain generated pseudo-Landau levels that delay the hot carrier relaxation time.

Furthermore, pseudo-magnetic fields have also been detected in acoustoelectric transport measurements through the emergence of a pseudo-Hall voltage in the direction transverse to SAW propagation. This was just reported during the realisation of this thesis by P. Zhao et al., 2022, where SAWs were used to induce a periodic corrugation with an amplitude tunable with the applied RF power. In this way, the RF power was adjusted to compensate the Hall voltage caused by an externally applied magnetic field, being able to neutralise magnetic fields of ±6 T with RF powers of 0.2-0.25 mW.

Coupling Light to Electronic Excitations

SAWs have also been shown to work as a dynamic diffraction grating for coupling far-field light into SPPs. This concept was first experimentally demonstrated by Sun et al., 1991, where the prism and the SAW were used combined to generate SPPs in the visible range. For that, IDTs were fabricated on the base of a $LiNbO_3$ prism and a silver layer was deposited between them. Later, Ruppert et al., 2010 showed this coupling without the need of a prism, just with SAWs acting as a grating to launch SPPs in a gold layer and far-field light impinging directly from the air. The principle behind this is that the surface corrugation produced by the SAWs provides the necessary momentum for the plasmonic coupling, while diffracting the incident radiation (Lean, 1973). The magnitude of the diffracted light increases with the reflection coefficient, which shows a peak when the SPPs are excited. Further details are given in Section 2.8.

In the case of graphene, the SAW-assisted coupling of far-field light into SPPs has been theoretically proven, revealing that SPPs interact with the optical phonons of the piezoelectric substrates, such as AlN and ZnO, leading to hybrid surface plasmon-phonon polaritons (SPPPs) (Schiefele et al., 2013; Fandan et al., 2018). Moreover, graphene can be integrated with other 2D materials such as h-BN, which presents two reststrahlen bands, where a SAW can also couple light into hyperbolic plasmon-phonon polaritons (HPPPs) (Fandan et al., 2018) In addition, this method suppresses the need for intricate near-field techniques or

patterning of the plasmonic material, which leads to a degradation of its quality. In addition, an on-chip IDT generating the SAW allows to switch electrically the polariton launching, thus facilitating the implementation of differential measurement schemes without rotating the polarisation of light.

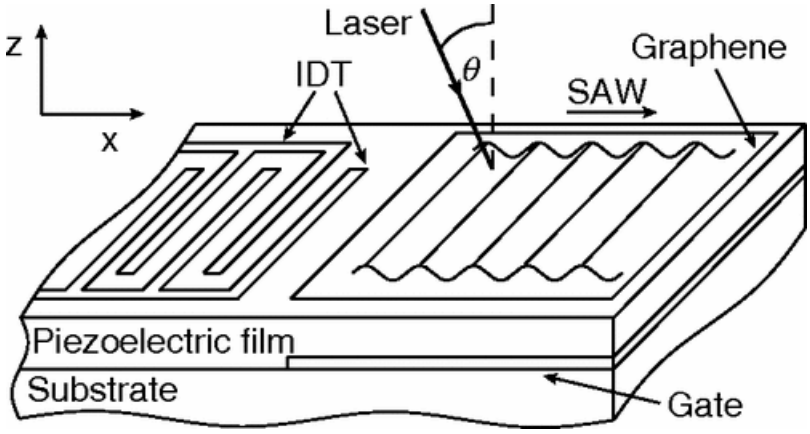

Figure 1.7: Illustration of a SAW-assisted plasmonic device. Reproduced from Schiefele et al., 2013.

Furthermore, this method has been proposed as a way to excite surface plasmon-exciton polaritons or plexcitons in 2D semiconductors such as MoS_2 or black phosphorus (Fandan et al., 2021). In this case, a thin metallic layer is placed below the 2D semiconductor with two functions: first, to support the SPPs that will hybridise with the excitons from the 2D material to form plexcitons, and second, to cancel out the piezoelectric field from either the substrate or the 2D material itself (if piezoelectric) so that the plexciton can propagate long distances carried by the strain field without dissociating the exciton.

1.2 Goal and Objectives

The goal of this thesis is to explore the capabilities of SAWs as actuators to modify the physical properties of graphene. Thus, the interaction of graphene with the different modulations accompanying SAWs (surface deformation and strain and piezoelectric fields) will be addressed. Two main objectives will be aimed, both having in common graphene as the material platform and SAWs as actuators: first, the alteration of the electronic transport properties of graphene in presence of SAWs, and second, the use of SAWs as dynamic diffraction gratings for the development of graphene-based plasmonic devices.

For the modulation of the electronic transport in graphene, contributions originating from both the piezoelectric and the strain fields of the SAW will be studied. Hence, this will include the acoustoelectric effect via the piezoelectric field in the direction of SAW propagation, as well as the pseudo-Hall effect arising in the direction perpendicular to SAW propagation due to the pseudo-magnetic or gauge field induced by the strain field of the SAW. SAWs are expected to exhibit several advantages compared to previous approaches used to generate strain-induced pseudo-magnetic fields. Unlike nanodefects such as bubbles, wrinkles or buckles (Levy et al., 2010), SAWs provide a deterministic approach, giving control over the location

and intensity of the strain. Moreover, SAWs offer a dynamic control over the strain, that lack static approaches using patterned substrates (Kang et al., 2021). However, the integrity of the piezoelectric substrate limits the amount of strain that can be generated by SAWs.

With respect to the excitation of SPPs, the capability of a SAW for coupling far-field light into SPPs will be used to design a graphene-based plasmonic biosensor activated by SAWs to probe the mid-IR fingerprint region of biolayers such as proteins or peptides. The combination of a SAW and a gate bias is aimed at providing tunability and dynamic control of propagating SPPs without reducing the plasmon lifetime due to edge scattering, unlike strategies relying on graphene patterning (Yan et al., 2013). This is expected to allow for simple, robust, on-chip biosensors, as opposed to near-field techniques. Moreover, a home-built mid-IR spectroscopy and imaging (mapping) system will be designed, assembled, and tested with the aim of permitting the future implementation of such plasmonic devices.

1.3 Outline of the Thesis

The structure of this thesis is organised as follows:

Chapter 2 describes the methods, both theoretical and experimental, that have been used to carry out the research reported in this thesis.

Chapter 3 describes the fabrication of SAW devices and how they modify the electronic transport in a graphene channel based on the effects associated to the piezoelectric and strain fields accompanying the SAW. Specifically, the acoustoelectric carrier transport and the emergence of a pseudo-Hall voltage in the transverse direction are reported. Moreover, different thin-film-LiNbO3-based structures are studied in search of an efficient piezoelectric substrate allowing a buried gate for the modulation of graphene.

Chapter 4 presents a theoretical study of mid-IR SPPPs in graphene-based heterostructures using the transmission matrix method, along with the design and modelling of a SAW-driven plasmonic biosensor for fingerprinting ultrathin biolayers down to the monolayer limit. A couple oscillators model is used to extract quantitative information from the biosensor response. The performance of the biosensor is modelled with relevant analytes as a protein bilayer or peptide monolayers.

Chapter 5 describes the design, assembly, and start-up of a home-built mid-IR spectroscopy and mapping setup based on QCLs. The design of the beam path for achieving maximum spatial resolution and efficient photodetection is presented. This system is aimed to allow, in the future, the characterisation of the SAW-driven plasmonic devices described in Chapter 4.

Finally, Chapter 6 contains the conclusions that can be drawn from the research described in the previous chapters, as well as the future studies that can be derived from the reported results.

Chapter 2

Methods

This chapter describes the tools and techniques that have been used in the development of this thesis, related to both the experimental and the theoretical aspects, from the fabrication and characterisation of devices to the modelling of the physical phenomena under study.

2.1 Electron Beam Lithography

The devices used in this thesis have been fabricated by electron beam lithography (EBL; Crestec CABL 9500C, 50 kV acceleration voltage), followed, when necessary, by metal deposition by Joule or electron beam evaporation, depending on the materials required, and lift-off. The fabrication process starts with the sample cleaning by means of oxygen plasma and piranha solution (1:1), followed by rinsing in deionised water (DIW) and drying under nitrogen flow. Then, the sample is rinsed in isopropyl alcohol (IPA) and dried again with nitrogen. Prior to the EBL, a dilution of ZEP520A positive electron beam resist is spin coated on the sample at 5000 rpm to achieve a thickness of ∼220 nm, followed by baking in a hotplate at 160 ºC. Since the substrate used ($LiNbO_3$) is highly insulating, to reduce charging effects, a highly conductive solution (Resonac ESPACER 300Z) is also spin coated at 3000 rpm, followed by a bake at 100 ºC. Once the sample is prepared, EBL is performed with a beam current of 2 nA, which provides enough resolution to define properly the devices, while maintaining a large throughput. After exposure, the sample is first rinsed in DIW to remove the ESPACER 300Z, dried with nitrogen, and then developed at room temperature in ZED-N50 for 1 minute, followed by drying with nitrogen. After metallisation, n-methyl-2-pyrrolidone (NMP) is used to remove the electron beam resist in the lift-off procedure. The device fabrication process is summarised in Figure 2.1.

For IDTs, the metal choice consists of 30 nm of gold on top of a 10-nm-thick titanium adhesive layer, deposited via electron beam evaporation. Alternatively, the adhesive layer can be made from 10 nm of chromium. In this case, the metals are deposited via Joule evaporation just because of the availability of target slots in the electron beam evaporation chamber. Nevertheless, no difference in the performance of IDTs has been observed in using Cr or Ti as the adhesive layer, their atomic masses being similar (52 and 48 Da) and significantly lower than the thicker Au layer (197 Da).

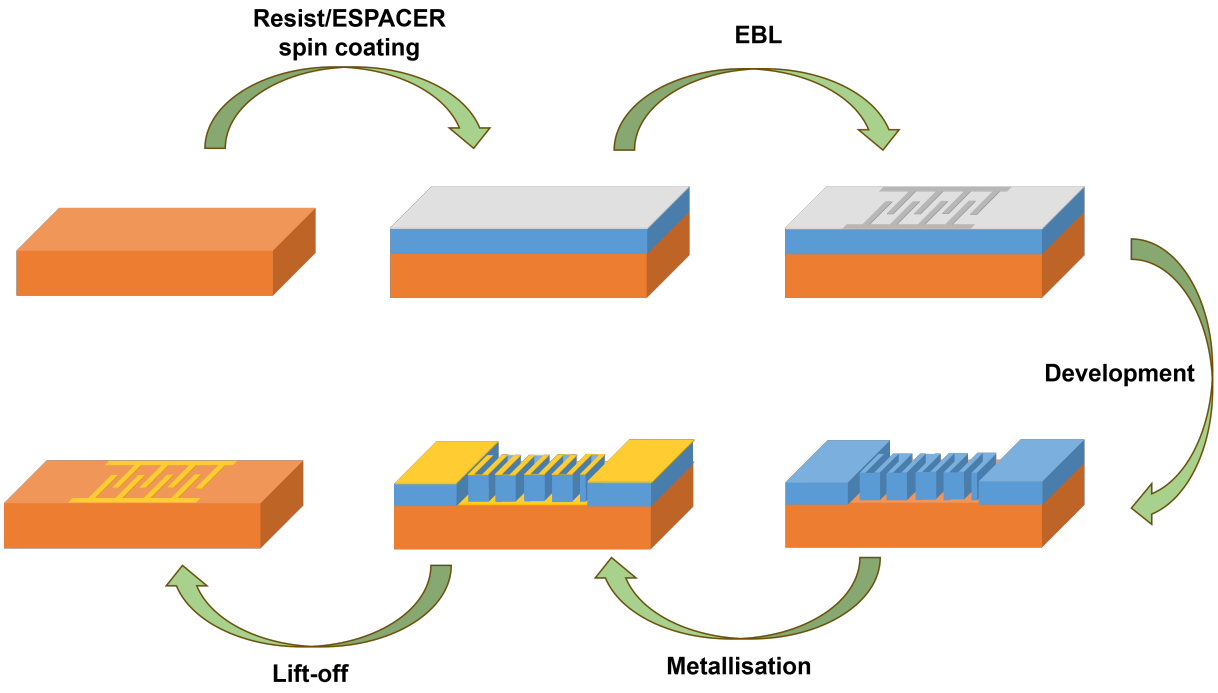

Figure 2.1: Schematic of a fabrication process involving lithography, metallization and lift-off.

2.2 Proximity Effect Correction

When the electron beam reaches the resist in a lithography, the volume of the resist affected by it is not limited to the extent of the spot size. Instead, the surroundings of the spot are modified by the secondary electrons generated in the resist and the substrate by the scattering of the primary electron beam. To account for this, *Tracer* and *Beamer* softwares by GenISys GmbH ("GenISys GmbH", Last accessed 2024) have been used to improve the fabrication process. *Tracer* can be used to calculate the scattering paths of secondary electrons in the resist-substrate stack (Figure 2.2(a,b)) and to calculate the point spread function (PSF) of the electron beam, that is, the actual 3D profile of the exposed region. Then, the original CAD design of the device and the PSF are given as inputs in *Beamer* to calculate the proximity effect correction (PEC), that is the dose correction necessary to keep the sizes and shapes of the original design, fracturing the original design into smaller trapezoids that will receive a tailored dose or exposure (Figure 2.2(c)).

These corrections are made as a factor that multiplies the base dose of the resist-substrate combination. A method to obtain the base dose consists in fabricating periodic arrays of stripes with 50% fill factor at different doses, followed by metal deposition and lift-off. Then, the sample is inspected with the scanning electron microscope (SEM), looking for a dose at which the stripes have the same width as pitch, this being the base dose. Note that the larger the area of the array, the more precise the base dose measurement will be, typically needing areas whose lateral size is hundreds of times the period of the array. Therefore, IDTs are not suitable for the base dose calculations.

However, because of the relatively large feature size of the IDTs in the SAW devices fabricated

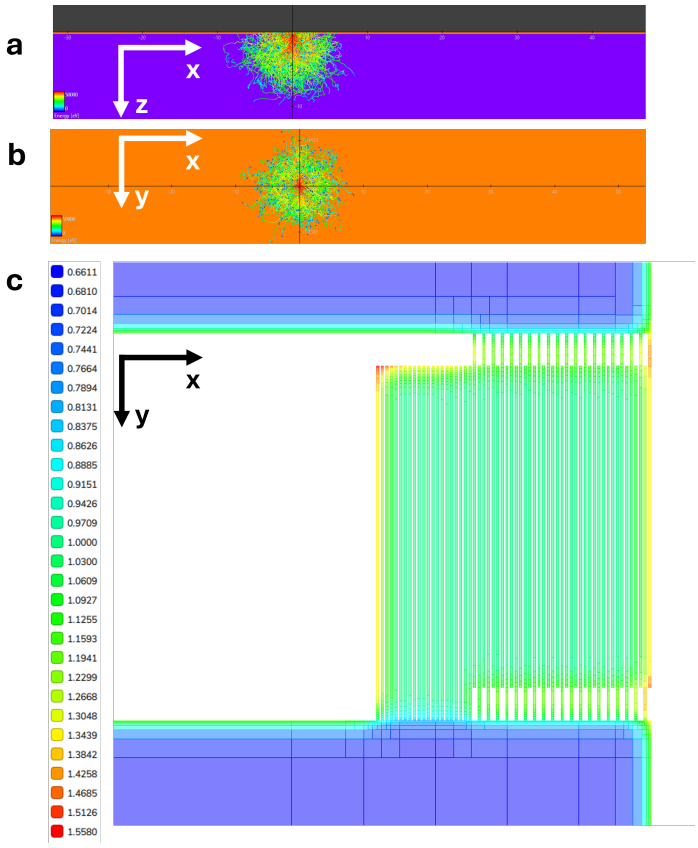

Figure 2.2: *Tracer* simulations of electron trajectories in the planes perpendicular **a** and parallel **b** to the surface of the sample. **c** Dose corrections calculated with *Beamer* in the design of an IDT. The colours represent the correction factor by which the base dose must be multiplied.

in this thesis, these proximity effect corrections have not been critical. Nevertheless, these corrections have proven to be specially useful in finding the correct dose when fabricating isolated structures such as the narrow electrical contacts to probe the changes induced by the SAW in a Hall bar. In any case, since the licences for these softwares were acquired when three years of this thesis had already passed, these programmes had a limited use in this thesis and there has not been much work towards the optimisation of the PEC corrections.

2.3 Graphene Transfer and Patterning

In this thesis, CVD graphene grown on copper foil (Boscá et al., 2023) has been transferred to $LiNbO_3$ substrates with the fabricated devices. For that, the graphene/Cu piece is spin coated with a 160-nm-thick polymethyl methacrylate (PMMA) protective layer. Graphene that may have grown on the backside of the Cu film is etched by an oxygen plasma before the transfer. The target substrate and the PMMA/graphene/Cu structure are then set in an automatic transfer system (Boscá, Pedrós, Martínez, Calle, and Palacios, 2015; Boscá et al., 2016), schematically illustrated in Figure 2.3, in which the Cu film is etched using an ammonium persulfate solution, and successive rinsing steps in DIW are performed, until

the PMMA-covered graphene sheet is floating in DIW with the substrate at the bottom. Finally, the DIW is totally drained and the graphene sheet is transferred onto the substrate. After transfer, the sample is held overnight in vacuum to remove the water left between the graphene and the substrate, so that graphene is completely attached to the substrate by van der Walls forces. Finally, the PMMA layer is removed with an acetone/IPA cleaning, after which AllResist AR 600-71 remover is used to eliminate eventual PMMA residues on the surface of graphene (Tyagi et al., 2022).

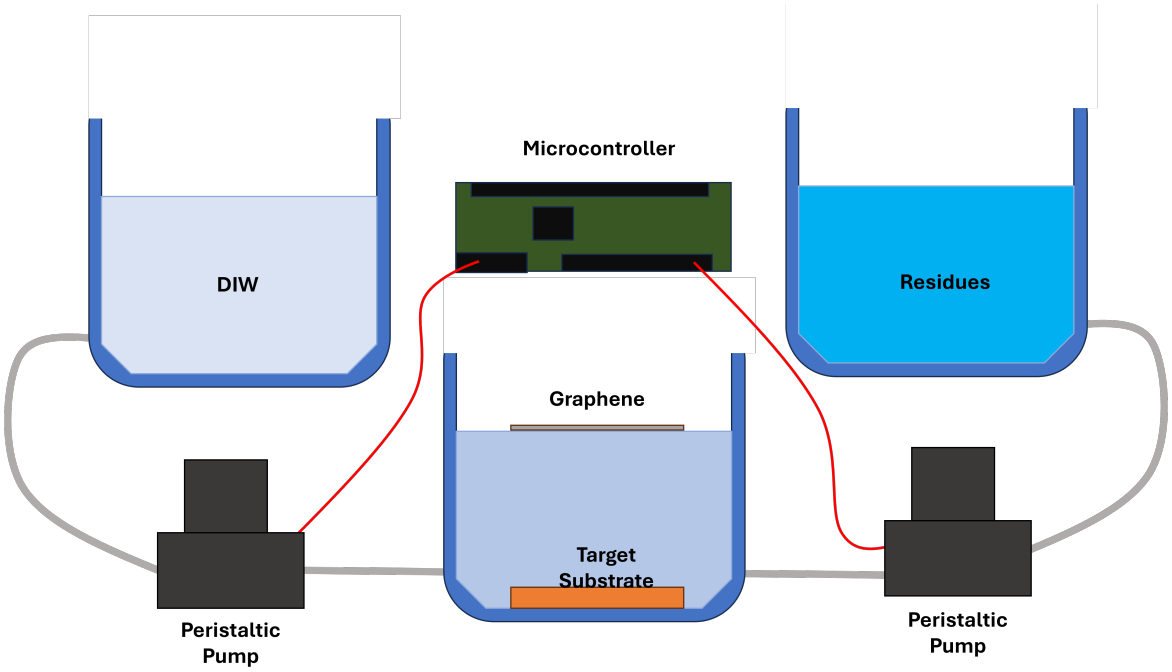

Figure 2.3: Schematic of the automatic transfer system.

After transfer, graphene was patterned as either a mesa or Hall bars. The pattern was defined via EBL and an oxygen plasma is used to remove areas from the cleared areas. Since NMP can damage the graphene, the ZEP520A resist is substituted by PMMA, which is developed in the AllResist AR 600-55 PMMA developer and can be removed later with acetone after etching.

2.4 DC Characterisation

DC electrical measurements, mainly current-voltage (IV) curves, addressing the output and transfer characteristics in graphene-based FET-like devices (Boscá, Pedrós, Martínez, and Calle, 2015), have been performed using an Agilent 4156C semiconductor parameter analyser (SPA) in combination with an Agilent 41501B pulse generator and expander unit module, where the latter has been used to achieve higher gate voltage values (up to ±200 V). Standard measurements have been carried out at room temperature using a Karl Suss PSM6 probe station with 4 DC probes, while measurements requiring vacuum and/or low temperature. Transport measurements, benefiting from a reduced electron scattering at low temperature

and, hence, enhanced signal-to-noise ratio, have been performed in a Janis CCR10-1 cryogenic probe station (see Figure 2.4) featuring 3 DC probes for DC and 2 coplanar ground-source-ground (GSG) RF probes, enabling measurements at temperatures as low as 15 K. Moreover, this probe station counts with a heater which allows to increase the temperature of the samples up to 500 K. This feature was used to perform alternate low-temperature/high-temperature cycles in vacuum in order to desorb residues and contaminants from the surface of graphene.

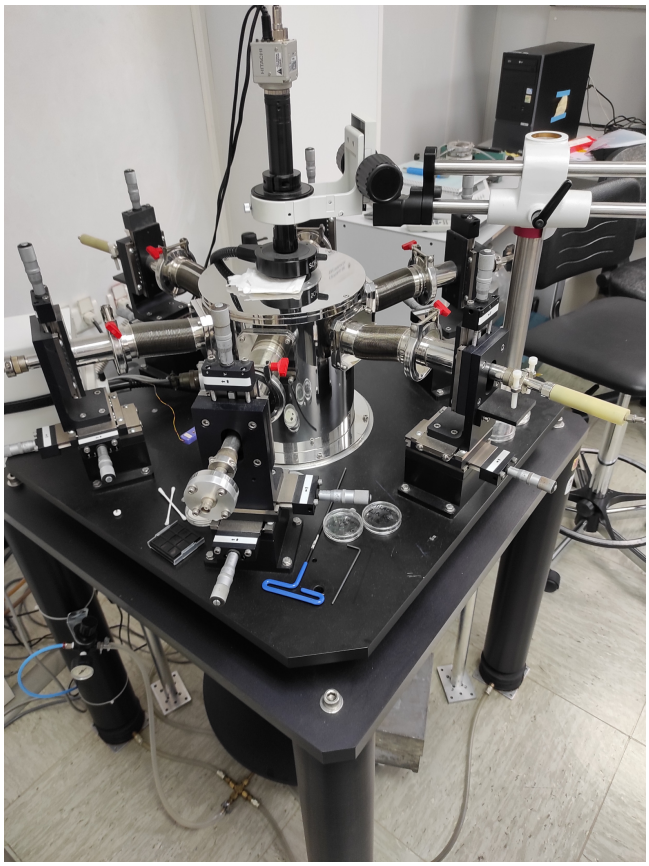

Figure 2.4: Photograph of the Janis CCR10-1 probe station used for low temperature and vacuum measurements.

2.5 RF Characterisation

The RF response of the SAW devices has been measured using a Vector Network Analyser (VNA) (Agilent N5230A PNA-L) in combination with a Cascade Summit 9000 series coplanar probe station with Ground-Source (GS) or GSG probes. A SOLT (Short Open Load Through) calibration kit has been used to substract the effect from the cables connecting the VNA output ports to the probes. The RF characterisation used in this thesis consists of measuring the S parameters, defined as the ratios between the applied and measured voltages at the ports as depicted in Figure 2.5 (note that + denotes the direction towards the other port):

$$
\begin{aligned}
S_{11} &= \left.\frac{V_1^-}{V_1^+}\right|_{V_2^+=0} \\
S_{22} &= \left.\frac{V_2^-}{V_2^+}\right|_{V_1^+=0} \\
S_{21} &= \left.\frac{V_2^-}{V_1^+}\right|_{V_2^+=0} \\
S_{12} &= \left.\frac{V_1^-}{V_2^+}\right|_{V_1^+=0}
\end{aligned}
\tag{2.1}
$$

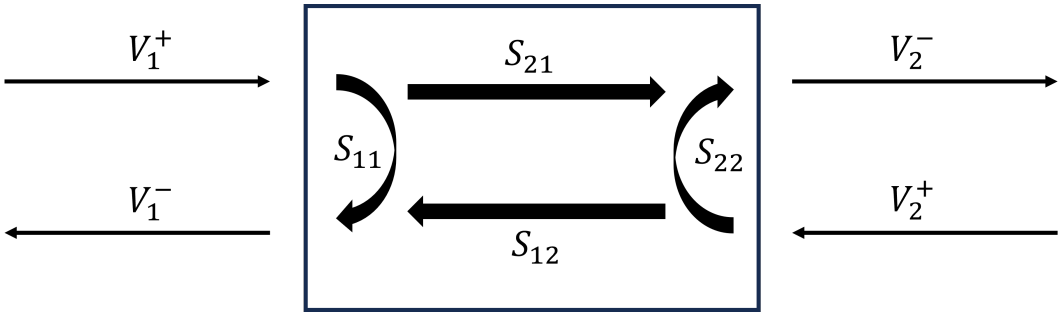

Figure 2.5: Schematic of the S parameters in a two-port network.

Thus, S_{11} and S_{22} represent the reflection of the RF signal at the input ports, while S_{21} and S_{12} represent the transmission from the input ports through the network to the output ports. The VNA can sweep the frequency of the signal, resulting in a spectrum for each of the S_{ij} parameters. Since the SAW wavelength is fixed by design (depending on the IDT period) and the sound velocity depends on the material, distinctive features will appear in the spectra of the S parameters at the frequencies corresponding to the propagating modes. Therefore, a dip will appear in the spectra of S_{11} and S_{22} at the frequency at which the SAW propagates, as the reflection will decrease at this frequency. In contrast, a peak will be observed in S_{21} and S_{12} at the frequencies at which the SAW is able to propagate from one port to the other. Furthermore, the depth of the dips in the reflection parameters and the height of the peaks in the transmission parameters are proportional to the electric-to-acoustic power conversion in the IDTs and to the capability of the system to deliver this power from one port to the other, respectively.

Metas VNA Tools software ("Metas VNA Tools", Last accessed 2024) and the scikit-rf Python library (Arsenovic et al., 2022) have been employed for the visualisation and processing, respectively, of the data measured with the VNA.

2.6 Scanning Electron Microscopy

A SEM (FEI Inspect F50) has been used to characterise the devices fabricated in this thesis. Due to the small size of the fingers of the IDTs (being 700 nm the largest ones fabricated,

corresponding to a SAW wavelength λ_{SAW} of 2.8 μm), an optical microscope, although sufficient to verify if a lift-off procedure has been successful, does not allow one to measure neither the wavelength nor the metallisation ratio of the devices. The SEM scans the surface of the sample with a high-energy electron beam and collects the secondary electrons emitted by the atoms of the sample, revealing its topography and allowing to distinguish materials of different conductivity. Since accelerated electrons carry a significantly larger linear momentum than visible light, the SEM allows to resolve smaller structures than an optical one; the higher the acceleration voltage, the higher the resolution. However, since $LiNbO_3$ is a highly insulating material, it suffers from charge accumulation problems when inspected with an SEM, such as sparkles or drift, which distort the image as seen in Figure 2.6:

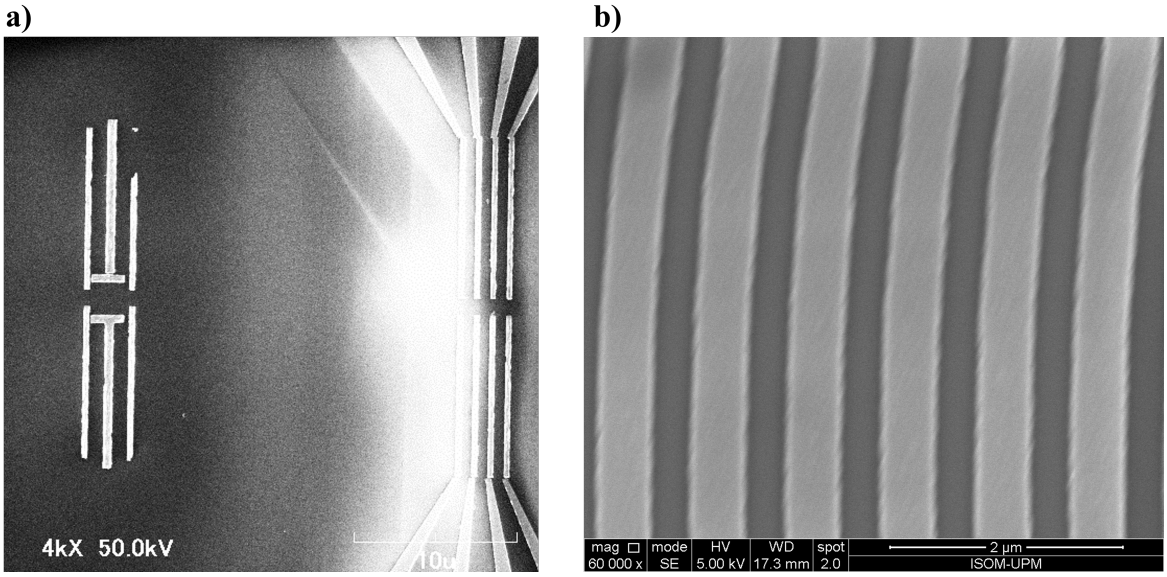

Figure 2.6: **a** Sparkle causing image saturation after a brief exposure to the electron beam. **b** Charge-accumulation-induced lateral drift resulting a distorted image with straight lines looking curved and less sharp edges. Note that (b) does not present sparkles, as the electron acceleration voltage is just 5 KV against 50 kV in (a).

This can be solved by lowering the acceleration voltage at the expense of reducing the resolution. However, a 2 kV acceleration voltage is enough to resolve lines down to 100 nm, and the high conductivity contrast between gold in the devices and the $LiNbO_3$ substrate, which is highly insulating, ensures a high enough contrast in the image. In addition, this contrast can be enhanced by increasing the exposure time and integrating over several scans. Most of the SEM images displayed in this thesis have been acquired using a 3 μs exposure time and a 10x line integration in the scans.

2.7 Transfer Matrix Method

The transfer matrix method (TMM) allows one to calculate the optical properties of a stack of materials from the permittivity and thickness of each of the layers that compose the stack, assuming that the first medium (usually air) and the last (typically the substrate)

are semi-infinite in the direction in which the light propagates. For this, the transfer matrix can be defined as a matrix that relates the amplitudes of the input and output forward and backward propagating fields.

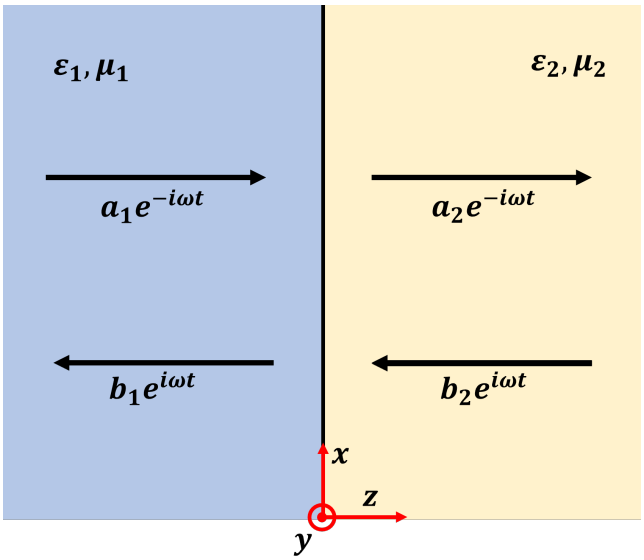

Figure 2.7: Schematic of light propagation accross an interface

In order to calculate the light propagation through a stack, two different cases need to be distinguished: propagation in a homogeneous material and propagation through the interface between two materials, which are considered by propagation matrices and transmission matrices, respectively. Propagation through a homogeneous medium merely introduces a phase shift between the forward a_j (backward b_j) propagation coefficients in both media, thus the amplitudes of the fields at position z and at position z+d can be related by (Zhan et al., 2013):

$$\begin{pmatrix} a_z \\ b_z \end{pmatrix} = P_d \begin{pmatrix} a_{z+d} \\ b_{z+d} \end{pmatrix} = \begin{pmatrix} e^{-ik_z d} & 0 \\ 0 & e^{ik_z d} \end{pmatrix} \begin{pmatrix} a_{z+d} \\ b_{z+d} \end{pmatrix}, \tag{2.2}$$

where the propagation matrix across the entire n^{th} layer of the stack is denoted as P_n.

On the other hand, the transmission matrix represents how crossing an interface between two media affects the electromagnetic radiation. The transmission matrix can be obtained from the boundary conditions at the interface:

$$\begin{aligned} \mathbf{n} \times (\mathbf{E_2} - \mathbf{E_1})|_{z=0} &= 0 \\ \mathbf{n} \times (\mathbf{H_2} - \mathbf{H_1})|_{z=0} &= \mathbf{j} \end{aligned} \tag{2.3}$$

where n is the vector normal to the surface of the interface, E and H denote the electric and magnetic fields, respectively, and j represents a possible current density at the interface. For p-polarisation, these equations lead to (Zhan et al., 2013):

$$\begin{pmatrix} a_i \\ b_i \end{pmatrix} = B_{ij} \begin{pmatrix} a_j \\ b_j \end{pmatrix} = \frac{1}{2} \begin{pmatrix} 1 + \frac{\varepsilon_i k_{jz}}{\varepsilon_j k_{iz}} + \frac{\sigma k_{jz}}{\varepsilon_0 \varepsilon_j \omega} & 1 - \frac{\varepsilon_i k_{jz}}{\varepsilon_j k_{iz}} - \frac{\sigma k_{jz}}{\varepsilon_0 \varepsilon_j \omega} \\ 1 - \frac{\varepsilon_i k_{jz}}{\varepsilon_j k_{iz}} + \frac{\sigma k_{jz}}{\varepsilon_0 \varepsilon_j \omega} & 1 + \frac{\varepsilon_i k_{jz}}{\varepsilon_j k_{iz}} - \frac{\sigma k_{jz}}{\varepsilon_0 \varepsilon_j \omega} \end{pmatrix} \begin{pmatrix} a_j \\ b_j \end{pmatrix} \tag{2.4}$$

Graphene, being an extremely thin conductive material, can be thought of as a surface charge density $\mathbf{j} = \sigma \mathbf{E}$ between two layers (Zhan et al., 2013), where σ is the frequency-dependent conductivity of graphene, which can be modelled as:

$$\sigma(\omega) = \frac{i \left| E_F \right| e^2}{\pi \hbar (\omega + \frac{i}{\tau})} \tag{2.5}$$

where E_F is the Fermi energy and τ is the electron relaxation time. A τ value of 0.4 ps has been assumed, which corresponds to a mobility value of μ=10000 $\mathrm{cm^2 V^{-1} s^{-1}}$. In the case of an interface in which there is no graphene, the conductivity value in the transmission matrix must be assumed as 0.

When the structure is composed by an arbitrary number of layers, propagation and transmission matrices can be combined as follows:

$$\begin{aligned} \begin{pmatrix} a_0 \\ b_0 \end{pmatrix} = \ B_{01} \begin{pmatrix} a_1 \\ b_1 \end{pmatrix} = B_{01} P_1 B_{12} \begin{pmatrix} a_2 \\ b_2 \end{pmatrix} = \\ = B_{01} P_1 B_{12} P_2 \dots B_{N-1,N} P_N \begin{pmatrix} a_N \\ b_N \end{pmatrix} = M \begin{pmatrix} a_N \\ b_N \end{pmatrix} \end{aligned} \tag{2.6}$$

where M is the transfer matrix. From the latter, the Fresnel reflection and transmission coefficients can be calculated, respectively, as follows:

$$r = \frac{M_{21}}{M_{11}} \ ; \ t = \frac{1}{M_{11}} \tag{2.7}$$

The SPP dispersion can be calculated as the poles of the imaginary part of the reflection coefficient, since at the plasmon frequency and wavevector the absorption takes a maximum value.

2.8 SAWs as a Dynamic Diffraction Grating

In the case of using a SAW as a virtual dynamic diffraction grating for coupling light into SPPs, it is necessary to calculate the power diffracted by the SAW in order to evaluate the reflection and transmission of the stack, and, ultimately, the SPP extinction. According to Lean, 1973, the $\mathrm{m^{th}}$ order diffracted power by a surface with sinusoidal corrugation is:

$$I_m = \left| r J_m \left(2 k_{z0} \delta \right) \left[1 + \frac{m \pi}{\lambda_{SAW} k_{zm}} \frac{1 + r}{r} \right] \right|^2 , \tag{2.8}$$

where r is the Fresnel reflection coefficient of the surface, J_m is the m^{th} order Bessel function, k_{z0} and k_{zm} are the wavevectors of the incident and m^{th} order diffracted beams and λ_{SAW} and δ are the SAW wavelength and amplitude, respectively. The light scattered by the SAW into the m^{th} diffraction order has the wavevector components:

$$k_{||m} = \frac{\omega}{c} sin\theta + m\frac{2\pi}{\lambda_{SAW}}; k_{zm} = \sqrt{(\frac{\omega}{c})^2 - k_{||m}^2}. \tag{2.9}$$

For all calculations in this thesis, a SAW amplitude of 1 nm has been assumed. Moreover, since $2k_{z0}\delta \ll 1$, then $|J_m(2k_{z0}\delta)|^2 \approx (2k_{z0}\delta)^2$ and the calculation can be restricted to the first diffraction order. In addition, in the case of graphene $2\pi/\lambda_{SAW} >> \omega/c$ and thus in all cases normal incidence has been considered, where the SPP wavelength is just given by the SAW wavelength.

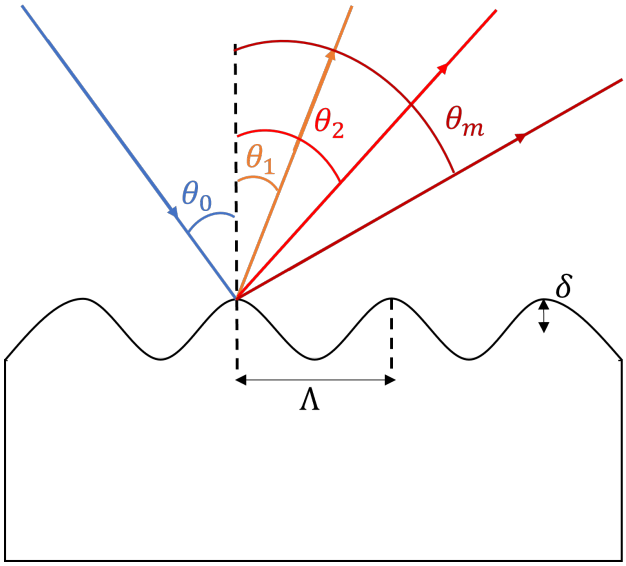

Figure 2.8: Schematic of the diffraction of far field light by a SAW. Different diffraction angles are displayed, corresponding to the different diffraction orders of the corrugated surface. The wavelength (Λ) and amplitude (δ) of the SAW are indicated.

Therefore, the reflectance and transmittance of a stack whose surface is deformed by a SAW are, respectively:

$$R = |r|^2 - I_1 \quad ; \quad T = |M|\,|t|^2 - I_1 \tag{2.10}$$

2.9 Frequency-dependent Permittivity

With aims to calculate the optical properties of heterostructures using the TMM, the permittivity of each layer needs to be known. The frequency-dependent permittivity of some materials used in this thesis have been extracted from the literature, such as h-BN (Dai et al., 2014), AlN (Kazan et al., 2009) or recombinant protein A/G and goat anti-mouse

inmunoglobulin (A/G-IgG) bilayers (Rodrigo et al., 2015). h-BN is an anisotropic material with two reststrahlen bands defined by its two IR active phonon modes: the in-plane ($\parallel$) A_{2u} phonon modes, with frequencies $\omega_{TO,\parallel} = 0.096$ eV and $\omega_{LO,\parallel} = 0.102$ eV, and the out-of-plane ($\perp$) E_{1u} phonon modes, with frequencies $\omega_{TO,\perp} = 0.169$ eV and $\omega_{LO,\perp} = 0.199$ eV. The frequency-dependent permittivity of h-BN has been modelled as (Dai et al., 2014, Supplementary Information):

$$\varepsilon_{h-BN,k}(\omega) = \varepsilon_{\infty,k}\left[1 + \frac{\omega_{LO,k}^2 - \omega_{TO,k}^2}{\omega_{TO,k}^2 - i\omega\gamma_k - \omega^2}\right], \tag{2.11}$$

where $k = \parallel, \perp$, $\varepsilon_{\infty,\parallel}$= 2.95 and $\varepsilon_{\infty,\perp} = 4.87$ are the high-frequency dielectric constants; and $\gamma_\parallel = 0.49$ meV and $\gamma_\perp$= 0.62 meV are the damping rates.

AlN is only slightly anisotropic compared to h-BN, so here, for simplicity, it is assumed to present an isotropic behaviour with a unique reststrahlen band located between $\omega_{TO} = 0.083$ eV and $\omega_{LO} = 0.111$ eV. The frequency-dependent permittivity of AlN has been modelled as (Kazan et al., 2009):

$$\varepsilon_{AlN}(\omega) = \varepsilon_\infty + (\varepsilon_0 - \varepsilon_\infty)\frac{\omega_{TO}^2}{\omega_{TO}^2 - i\omega\gamma - \omega^2}, \tag{2.12}$$

where ε_0= 7.37 and $\varepsilon_\infty = 3.93$ are the static and high-frequency dielectric constants, respectively, and $\gamma = 0.64$ meV is the damping rate.

However, the frequency-dependent permittivity of other materials used as analytes cannot be directly found in the literature, as in the case for 4,4'-bis(N-carbazolyl)-1,1'-biphenyl (CBP) or Valine Gramicidin A (VGA). In these cases, the literature (Beck et al., 2015 for CBP, Lavoie et al., 2002 for VGA) has been consulted to extract the frequency-dependent optical transmission $T(\omega)$ of layers of known thickness d, so the frequency-dependent imaginary part of the refractive index $\kappa(\omega)$ of the material can be obtained from the Beer-Lambert law:

$$\kappa(\omega) = \frac{1}{4\pi\omega d} log(\frac{1}{T(\omega)}), \tag{2.13}$$

The real part of the refractive index can be then computed using the Kramers-Kronig method, see Lucarini et al., 2005. Now that the complex refractive index $\tilde{n}(\omega)$ is known, the frequency-dependent permittivity $\varepsilon(\omega)$ can be obtained as:

$$\varepsilon(\omega) = \varepsilon_1(\omega) + i\varepsilon_2(\omega) = \tilde{n}^2(\omega) = (n(\omega) + i\kappa(\omega))^2$$

$$\varepsilon_1(\omega) = n^2(\omega) + \kappa^2(\omega) \tag{2.14}$$

$$\varepsilon_2(\omega) = 2n(\omega)\kappa(\omega)$$

Finally, in order to simplify the calculation and to smooth the dielectric functions, the data

are fitted to a sum of as many Lorentzian oscillators as relevant absorption peaks the material exhibits:

$$\varepsilon(\omega) = \varepsilon_\infty + \sum_{k=1}^{N} \frac{h_k^2}{\omega_k^2 - i\omega\gamma_k - \omega^2}, \tag{2.15}$$

where ε_∞ is the high frequency permittivity and h_k, ω_k, and γ_k are, respectively, the amplitude, resonance frequency, and relaxation rate of each oscillator. The parameters of the Lorentz oscillators used to model the three analytes discussed in this thesis (CBP, VGA, A / G-IgG) and the graphs of their frequency-dependent permittivity can be found in Table 2.1 and Figure 2.9, respectively, whether they have been taken from the literature or calculated using the Kramers-Kronig method.

Analyte	ω_1	γ_1	h_1	ω_2	γ_2	h_2	ω_3	γ_3	h_3	ε_∞
CBP	1449	7.99	99.8	1479	5.91	33.5	1504	13.06	105.4	2.8
VGA	1452	20.8	34.4	1535	52.4	109	1637	28.4	114	3.56
A/G-IgG	1530	61.6	194	1655	59.1	258	-	-	-	2.1

Table 2.1: Parameters for modelling the permittivity of the analytes, where h_k, ω_k, and γ_k are all given in units of cm^{-1}.

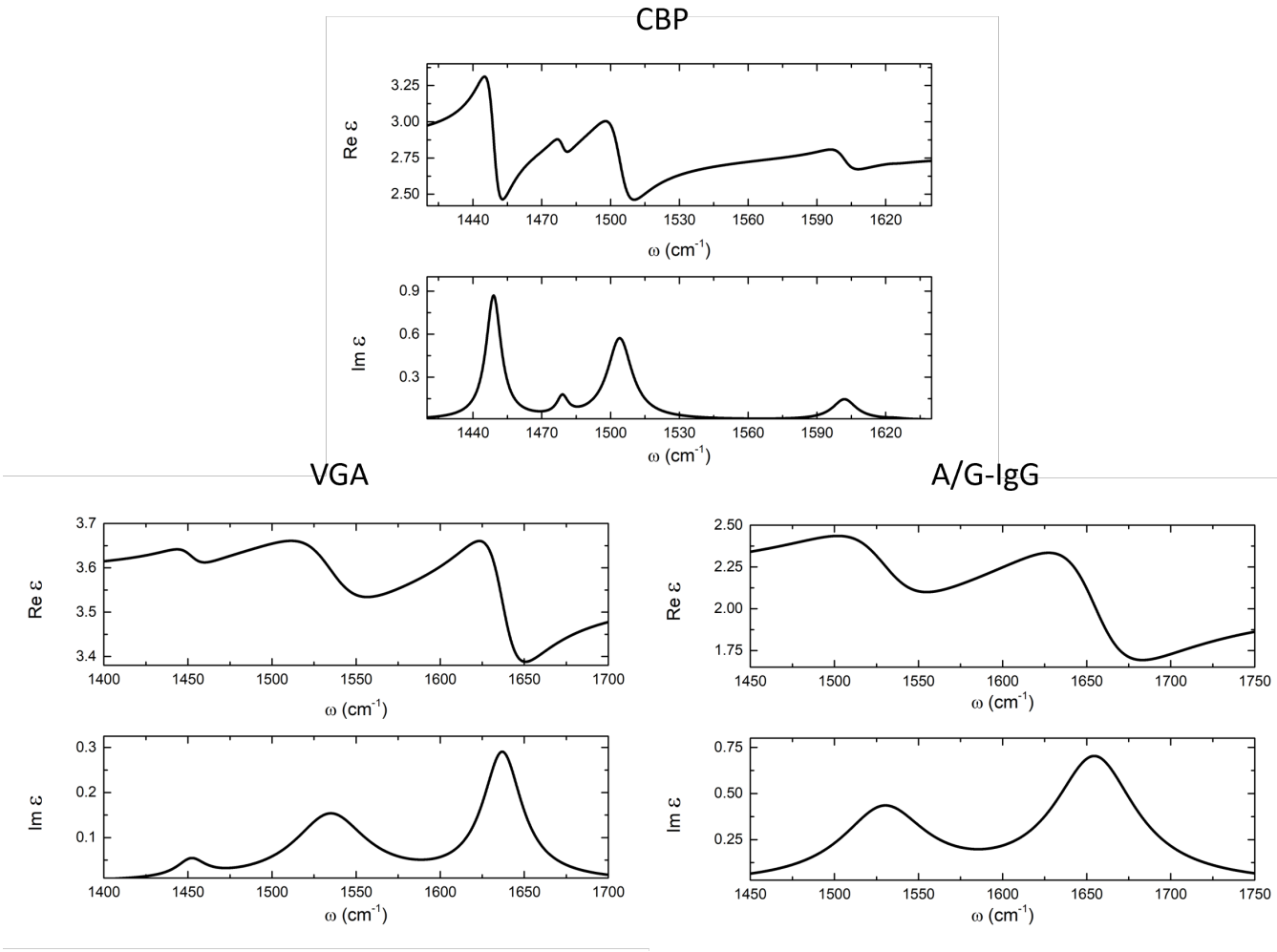

Figure 2.9: Frequency-dependent real and imaginary parts of the permittitivy of the analytes used in this thesis.

Chapter 3

Acoustoelectric Transport in Graphene

In this chapter, first, the design and fabrication of two-port SAW resonators in $LiNbO_3$ substrates is addressed. Then, their use to study the contributions of the SAW piezoelectric and strain fields in charge transport experiments in graphene Hall bars is reported. Finally, heterostructures based on thin-film $LiNbO_3$ are examined as an alternative to bulk substrates with the objective of using buried electrodes to electrostatically modulate the Fermi level of graphene. Here, SAW devices with wavelengths in the micrometre range (2.8-1.6 μm) have been targeted, as they are easily accessible through EBL and provide large enough acoustoelectric signals. The larger wavelength of the range has been used for bulk substrates, whereas the lower one has been employed in thin-film structures in order to prevent detrimental effects from the metallic interlayer and the substrate.

3.1 Design and Fabrication of SAW Devices

Two-port SAW resonators have been fabricated by EBL (see Section 2.1) on 128° rotated Y-cut X-propagating black $LiNbO_3$ (b-$LiNbO_3$) substrates. This material and crystal cut have been chosen because of their remarkably high electromechanical coupling coefficient $K^2 = 5\%$ (C. K. Campbell, 1998). The $LiNbO_3$ is called 'black' since its colour is modified by the doping introduced in the crystal for cancelling out its pyroelectric effect, which, otherwise, makes the fabrication process more complicated.

Since devices have been fabricated using EBL, the first step was to set the working conditions of the lithographic equipment. SAW frequencies in the range of 1-3 GHz are targeted, corresponding to minimum feature sizes of several hundreds of nm, so relatively large beam currents (2 nA) and medium-sized writing fields (600 μm) can be used with no resolution limitations, thus having an increased throughput when compared to lower beam currents. Once the beam current and field size to be used were determined, dose tests were performed following the procedure in 2.1 to determine the optimum exposure time for the resist-substrate combination. Initially, a dose that maximised the performance of the devices was sought. Therefore, tests consisting of repeating the aforementioned device in a matrix where the exposure time was different for each element (or set of elements, having several devices under the same exposure time to reduce the device-to-device variability). The devices were then

metallized and measured with the VNA. Ideally, the dose test should cover a wide enough range of dose values so that there are devices clearly under-exposed and clearly overexposed. Since the resist used for fabrication is a dilution of the original, dose tests were also performed over time to ensure that at any time the dose used was the optimum, which usually ranges between 50 and 60 ns of exposure to the electron beam. Later in the thesis, once *Beamer* and *Tracer* tools were available, the dose tests were aimed at obtaining the base dose as described in Section 2.2 so that it could be used in a proximity-effect-corrected device design rather than using a constant dose for the whole device.

There are several design parameters that influence the electrical behaviour of the two-port SAW resonators, such as the number of electrodes in the IDT, the IDT aperture, the IDT period or the number of electrodes in the reflectors. These parameters are described briefly in the following subsections.

3.1.1 Number of Electrode Pairs

The number of electrode pairs in the IDT affects the performance of the SAW device in various ways. The larger the number of electrode pairs, the larger the capacitance of the device, therefore affecting its impedance. Moreover, increasing the number of electrodes also reduces the resonance bandwidth (measured between first nulls on either side of the centre frequency) according to:

$$BW = \frac{2f_0}{N_p}, \tag{3.1}$$

where f_0 is the centre frequency of the passband and N_p is the number of electrode pairs. Due to the high electromechanical coupling factor of $LiNbO_3$, a small N_p is sufficient to efficiently generate SAWs (C. Campbell, 1989). In Figure 3.1 (a-c), the S parameters of two-port SAW resonators with a 2.8 μm wavelength and different N_p values are presented. The transmission parameters reach a higher peak value in the devices with 10 and 20 electrode pairs, with the latter being slightly more efficient. However, the reflection parameters show greater dips at the resonance frequency for the 20-electrode-pair device. Moreover, the passband narrows as the number of finger pairs is increased, as shown in Figure 3.1 (d), confirming the $1/N_p$ trend described by Equation 3.1, although the values differ slightly. This difference may be attributed to the lack of resolution when calculating the centre frequency of the passband. Therefore, due to the increased performance in terms of the S_{ii} parameters and to the slight improvement in the S_{ij} parameters, the number of electrodes in the subsequent devices was set to 20 pairs.

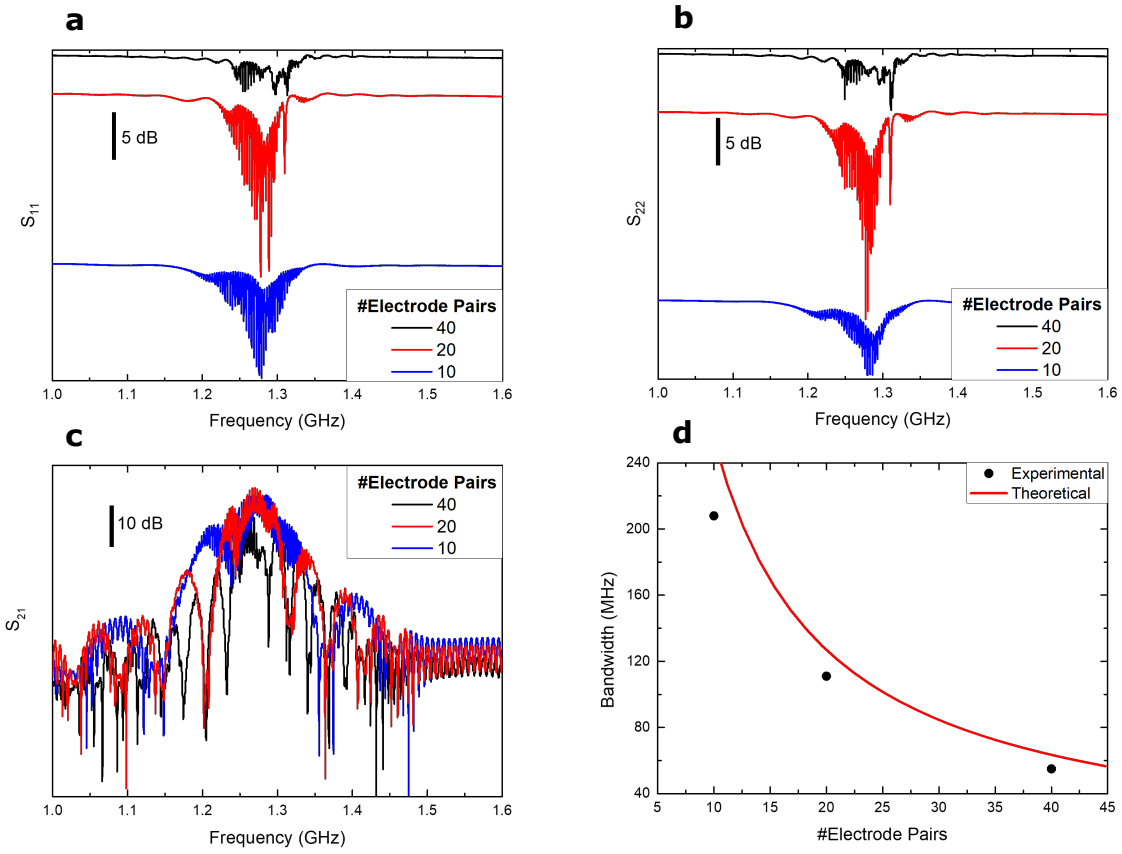

Figure 3.1: S parameters of two-port SAW resonators with a wavelength of 2.8 μm, an aperture of 120 μm, a 20-strip Bragg reflector, and different number of electrode pairs. **a** S_{11}, **b** S_{22}, **c** S_{21}. **d** Dependence of the bandwidth of the resonance of S_{21} as a function of the number of electrode pairs of the IDT. The experimental data points are extracted from (c), whereas the theoretical curve follows Equation 3.1.

3.1.2 IDT Aperture

In this work, SAWs are not going to be used as an electronic filter but rather as a means to manipulate the physical properties of 2D materials. Because of this, a slight decrease in the electrical performance of the device can be accepted as a trade-off for an increase in the effect caused by the SAW. In particular, IDT apertures ranging from 120 to 30 μm have been studied as alternatives to reduce the beam width and therefore increase the acoustic power density. Figure 3.2 depicts the S parameters of IDTs with 120, 80, 50 and 30 μm aperture, showing a 2-3 dB decrease in the S_{21} parameters, while the power density will increase by 1.5 (80 μm aperture), 2.4 (50 μm) or 4 times (30 μm) due to the reduction in the SAW beam width. However, it is important to note that decreasing the aperture leads to an increase of the diffraction of the beam, thus reducing the power density. Therefore, following the design rule in C. K. Campbell, 1998, which states that the IDT aperture should have a size between 10 and 100 times the SAW wavelength (28-280 μm in this case), the 30-μm-aperture devices have been discarded due to the proximity to the lower limit of this range and an IDT aperture

of 50 μm was chosen.

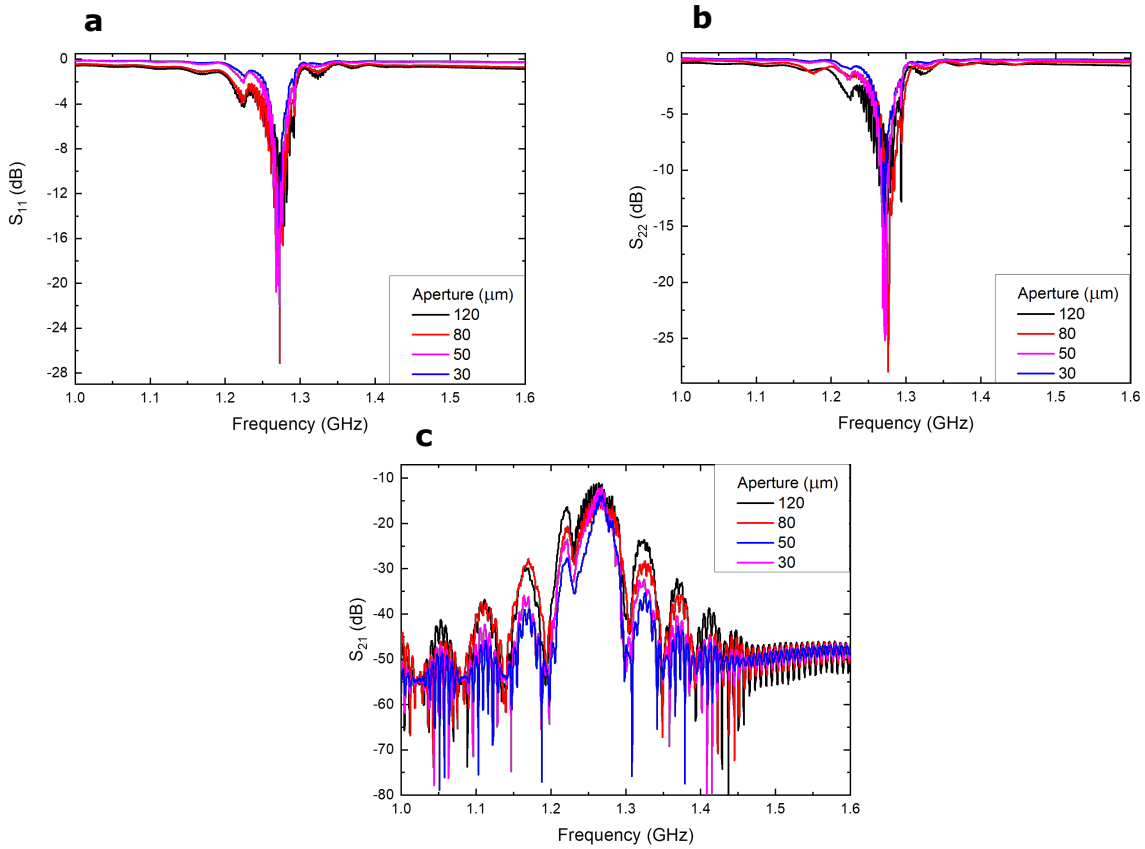

Figure 3.2: Comparison of two-port SAW resonators with a wavelength of 2.8 μm, 20 electrode pairs, 20-strip Bragg reflectors and various values of the IDT aperture. **a** S_{11}, **b** S_{22}, and **c** S_{21}.

3.1.3 IDT Period

IDTs with periods of 2.8 μm and 1.6 μm were fabricated. Small wavelengths (large wavevectors) are desired as they lead to greater signals in acoustoelectric effects (Bandhu et al., 2013; P. Zhao et al., 2022) and allow to probe higher energy ranges of the plasmonic dispersion (Schiefele et al., 2013; Fandan et al., 2018). Figure 3.3 shows a comparison between the S parameters of the SAW devices with periods of 1.6 μm and 2.8 μm, which present similar values, although propagation losses in SAW devices tend to increase with frequency.

A chirped IDT design has also been tested, where the wavelength of the IDT has been gradually changed from 2.8 μm down to 1.6 μm, in steps of 200 nm with 4 electrode pairs per wavelength, with the objective of fabricating a device with a wide resonant band. As shown in Figure 3.4, it resulted in weak S_{ii} parameters showing the individual resonances of the different electrode periods included in the device, but the passband in the S_{21} parameter is not as wide as expected. Hence, although the device can provide continuous SAW generation with S_{21} above -30 dB across a 370 MHz band, it loses efficiency at frequencies above 1.7 GHz.

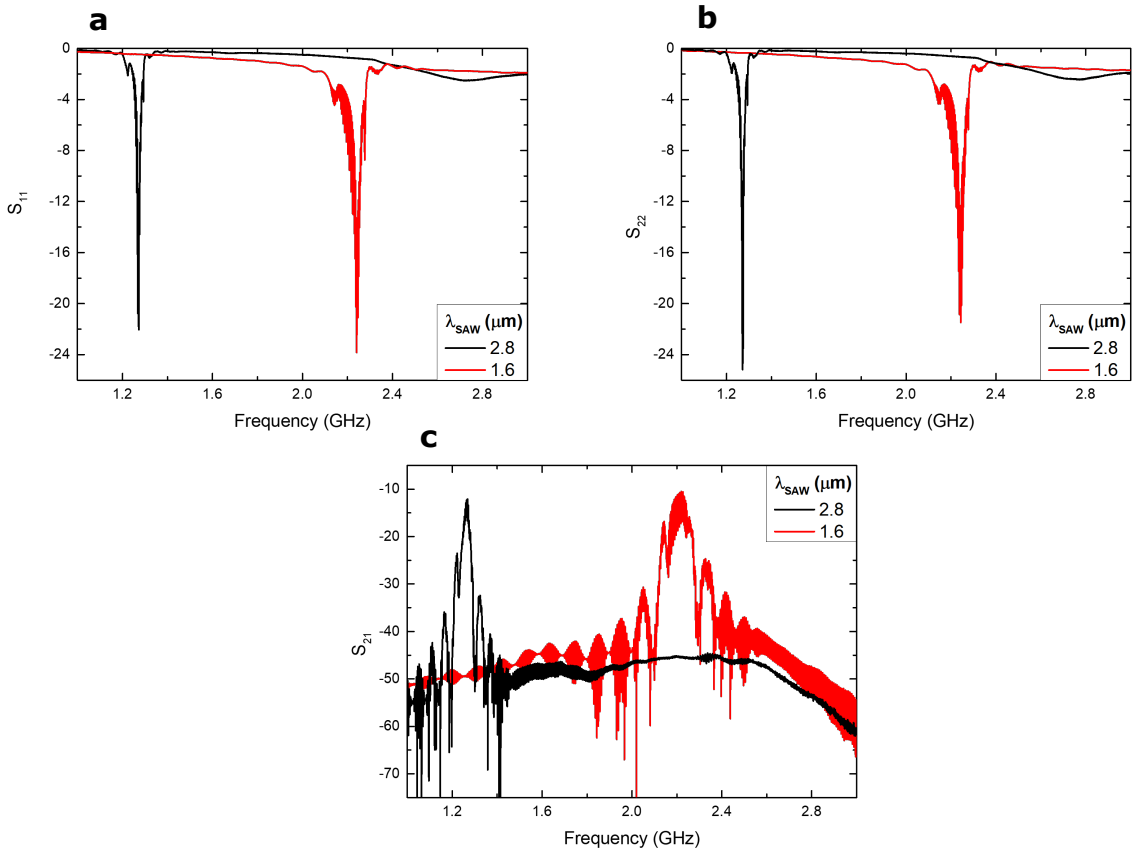

Figure 3.3: Comparison of two-port SAW resonators with 2.8 μm and 1.6 μm SAW wavelength, 20 electrode pairs, 20-strip Bragg reflectors, and 50 μm IDT aperture. **a** S_{11}, **b** S_{22}, and **c** S_{21}.

Because of that, single wavelength devices were preferred for obtaining larger acoustoelectric signals (as a result of their higher wavevector). However, an optimised chirped IDT may prove useful in measuring the wavelength dependence of the acoustoelectric effects, since it provides a flat broad transmission band in a single device.

3.1.4 Reflectors

The two-port SAW resonators include, aside from the IDTs, two sets of Bragg reflectors formed by a grating of metallic strips (with the same metal thickness as the electrodes of the IDTs) with a period of half the SAW wavelength. Since $LiNbO_3$ presents a high K^2 value, the number of strips needed in the reflector for total reflectivity is rather low, in the range of tens, according to C. Campbell, 1989. Therefore, Bragg reflectors with 20 strips were included in the SAW devices.

However, in the previous figures depicting the S parameters of two-port SAW resonators, one can notice a ripple in the passband, which can cause differences in performance of up to several dB. A time analysis of the response of the SAW resonators has been performed, as presented in Figure 3.5. The S_{21} parameter, which contains information on the propagation

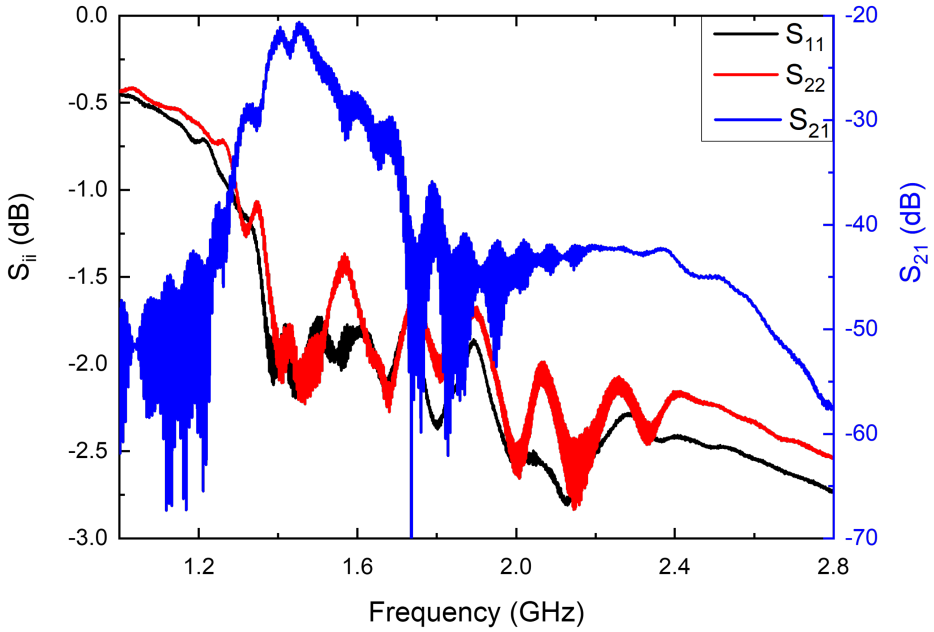

Figure 3.4: S parameters of a chirped SAW delay line without reflectors in the 1.6-2.8 μm wavelength range.

of the SAW between IDTs, has been converted to the time domain ($\bar{S}_{21}$, Figure 3.5(a)). Five different peaks are observed in the time domain signal.

The first peak, which occurs near 0 propagation time, corresponds to the electromagnetic feedthrough or crosstalk between the IDTs, the effect resulting from the direct coupling between the IDTs through electromagnetic radiation. Therefore, it takes place at the speed of light, making this effect almost instantaneous. The second peak is located at $\tau = 154$ ns time delay, which, taking into account the 543.2 μm (194 λ_{SAW}) separation between the IDTs, results in a propagation velocity of 3550 m/s. The velocity calculated from the frequency peak (1.268 GHz) is 3540 m/s, concluding that this first peak is due to the SAW propagation from the input IDT to the output one.

Now, the third peak appears at a delay of $\sim 3\tau$. Therefore, this peak can be attributed to a propagation three times the distance that separates the IDTs, meaning that this contribution comes from the wave reaching the output IDT, reflecting back towards the input IDT, and there reflecting back again to the output. In addition to the time at which the signal appears, there is a 17 dB difference in amplitude with the second peak, which means that this is not the main contribution to the signal. However, it is large enough to affect the resonance with an interference pattern. The signal modulation coming from the interference of this signal with the fundamental one is referred to as triple transit interference (TTI) in the literature (C. K. Campbell, 1998).

Finally, the last two peaks are more difficult to explain because of their internal structure,

but they are far more attenuated than the rest of them. From the position of their maxima, at $\sim 5\tau$ and $\sim 7\tau$, they could be attributed to higher-order reflections (the wave travelling between the IDTs 5 and 7 times, respectively).

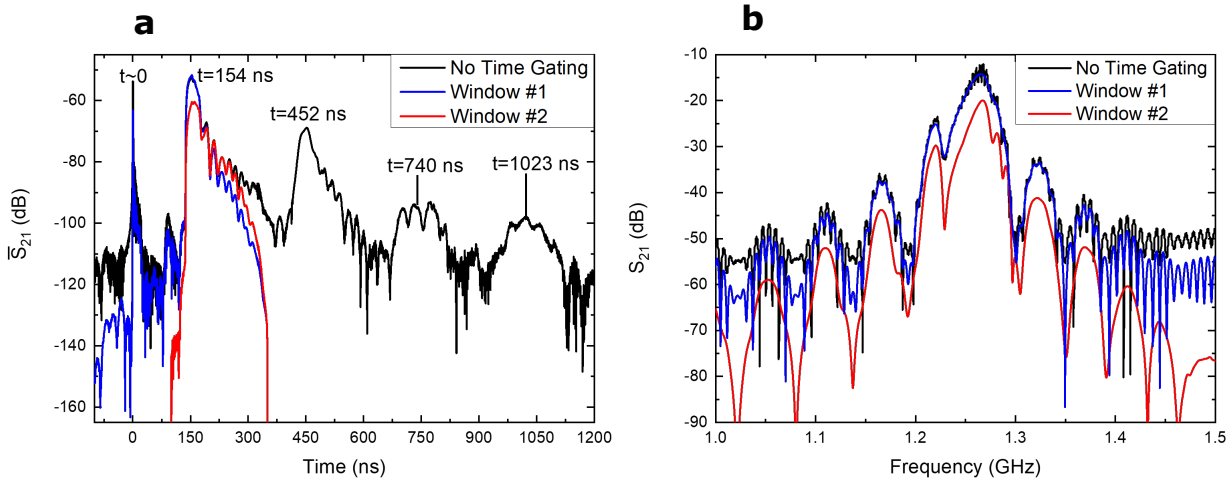

Figure 3.5: Time-gating analysis of the S_{21} parameter of a two-port SAW resonator with 20-strip reflectors. **a** Time domain signal before and after applying various Hann-type time windows for the filtering. **b** S_{21} bafore and after filtering in the time domain.

In the frequency domain (Figure 3.5 (b), black curve), a 3.5-MHz-frequency modulation dominates in the passband, whereas a 7-MHz-frequency modulation appears in the side lobes. These frequencies agree well with those corresponding to the TTI ($1/\tau$) and the electromagnetic crosstalk ($1/2\tau$), according to C. K. Campbell, 1998.

A first Hann window, from -100 to 350 ns, was used to filter out the triple transit contribution, resulting in a great reduction of the modulation appearing in the passband, that is, the one attributed to TTI, while the 7 MHz modulation in the side lobes, attributed to electromagnetic crosstalk, remains. A second Hann window spanning from 100 ns to 350 ns has been used to eliminate also the influence from the crosstalk. This completely eliminates the modulation in the side lobes.

TTI appears in SAW delay lines due to the re-emission of the energy received from the SAW by the IDTs. Several solutions are usually deployed in SAW filter design, such as introducing an impedance mismatch between the IDTs or using IDTs with split-electrode geometries (Morgan, 2007). However, none of these solutions is recommended in the case of this study. Both IDTs should be impedance matched in the case that standing SAWs would need to be used. On the other hand, split-electrode IDTs have been disregarded to avoid increasing the lithographic resolution of the device without obtaining the increase in the acoustoelectric voltage that would be gained with a shorter SAW wavelength. Moreover, split-electrode IDTs present an intense 3^{rd} harmonic, that reduces the intensity of the fundamental mode, and that is naturally cancelled in single-electrode IDTs with 50% metallisation ratio (C. Campbell, 1989).

Nonetheless, it has been experimentally observed by colleagues in the research group that

the use of a Bragg reflector with a high number of floating strips considerably reduces the ripple caused by TTI. Thus, Figure 3.6 presents the S parameters of a 1.6 μm wavelegnth two-port SAW resonator with a 300-strip Bragg reflector compared to those of a SAW delay line with the same design but without reflector, showing a great reduction of the TTI ripple (from 12 to 4 dB in S_{21}) when using the 300-strip Bragg reflector. This, in principle, seems counterintuitive, since an enhanced reflector would increase the SAW amplitude and thus, also the amplitude of the TTI ripple. Nevertheless, this experimental finding has been consistently observed across a number of samples.

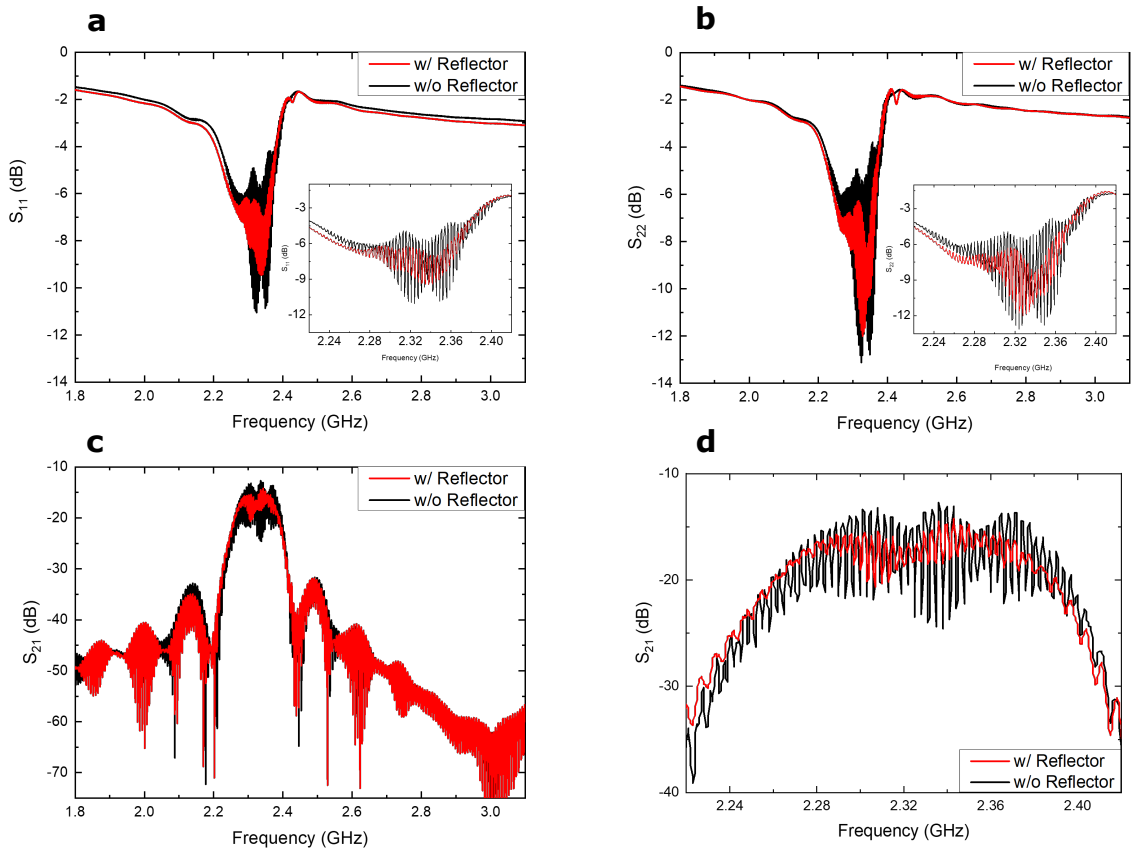

Figure 3.6: S parameters of a 1.6 μm SAW device without reflectors and with 300-strip reflectors. **a** S_{11}, **b** S_{22}, and **c** S_{21} Insets in (a) and (b) show a magnified view around the resonance, while **d** is a magnified view of (c).

3.2 Acoustoelectric and Pseudo-Hall (Gauge) Voltages in Graphene

The two-port SAW resonators described in the previous section were fabricated along with a set of electrical contacts between the IDTs that allow probing the electrical properties of graphene, which was transferred to the sample and patterned in the form of Hall bars. The distance between the IDT centres has been set to 543.2 μm (194 λ_{SAW}) in order to

accommodate 16 metallic contacts between them, as shown in Figure 3.7.

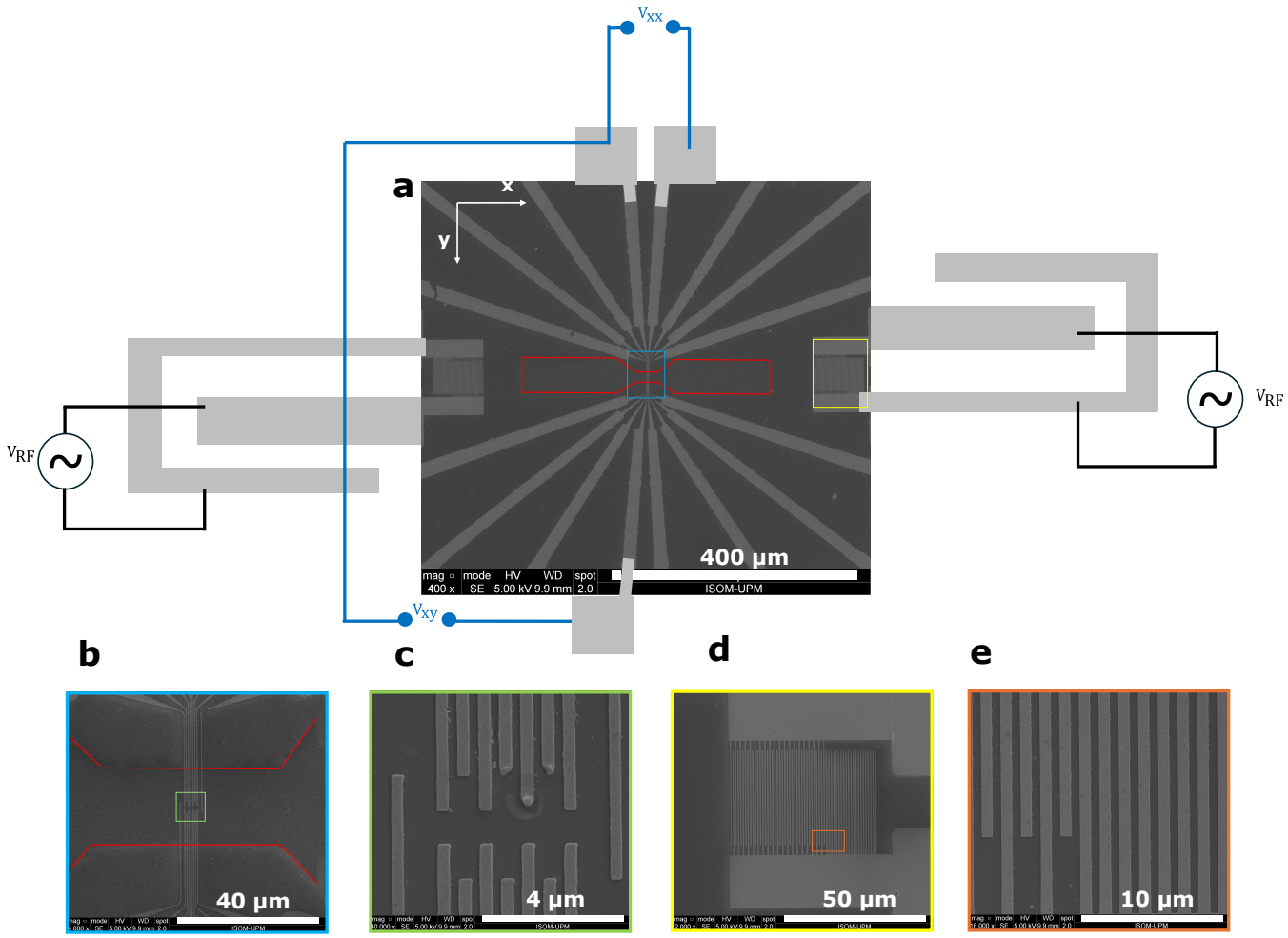

Figure 3.7: SEM images of the devices used for the acoustoelectric measurements. **a** General view with graphene outlined in red for a better appreciation. The RF signals fed to the IDTs, as well as the longitudinal (V_{xx}) and transverse (V_{xy}) voltages measured at the Hall bar are schematically displayed. **b** Detail of the graphene-covered zone outlined in red in (a). **c** Detail of the metallic contacts, zone outlined in green in (b). **d** Magnified view of the right IDT, which is outlined in green in (a). **e** Detail of the electrodes of the right IDT, in the area outlined in orange in (d).

The SAW resonators were characterised by means of their S parameters, shown in Figure 3.8 (a). They exhibit a slight decrease in performance compared to the ones shown previously in this chapter. This can be due to several facts, such as the lack of calibration when used in the cryostat, which also causes the modulation that can be seen out of the resonance, the second lithography level, which increases the thickness of the pads, or the elongation of the RF pads, which is needed to prevent the DC and RF probes from colliding. Note also the TTI present in the resonance, which will prove to be a difficulty when selecting the optimal operation frequency. Furthermore, the electrical behaviour of graphene in the SAW path was characterised by measuring IV curves between the electrical contacts that were used for

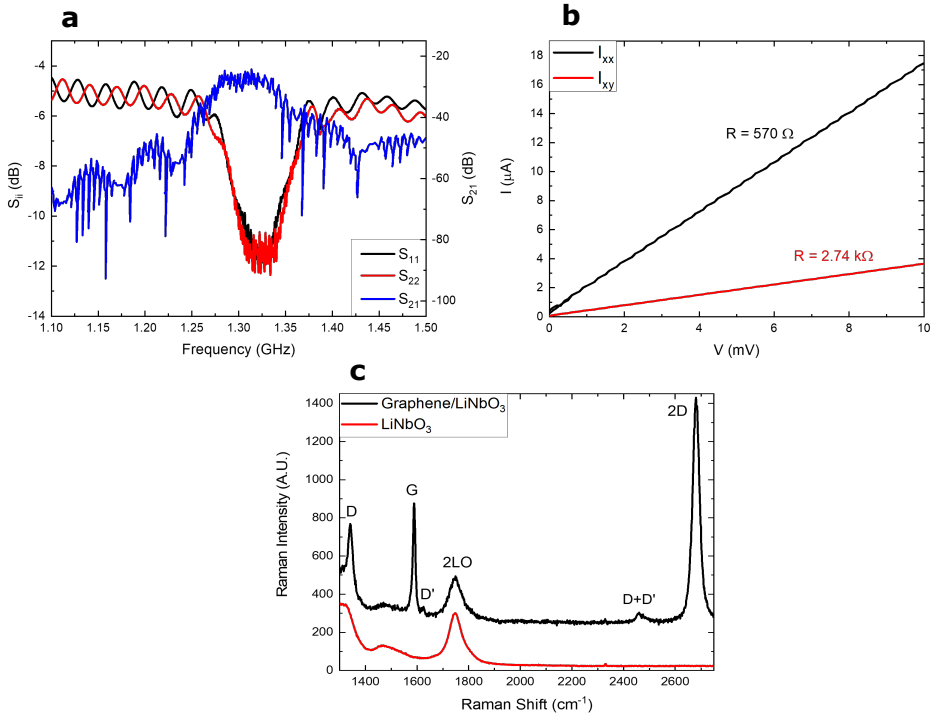

Figure 3.8: RF and DC (16 K), and Raman (RT) characterization of the devices used for acoustoelectric measurements: **a** S parameters of a SAW resonator and **b** I-V curve of a graphene channel parallel (black) and perpendicular (red) to the SAW propagation direction. **c** Raman spectra recorded on graphene (black) and on the bare $LiNbO_3$ substrate (red).

the acoustoelectric measurements. An example of these curves is shown in Figure 3.8 (b), measured at the channels in the x (I_{xx}) and y (I_{xy}) directions accross which the acoustoelectric and pseudo-Hall voltage measurements presented in this chapter have been acquired. It is also clear that the current is different in the x (along the SAW) direction and the y (perpendicular to the SAW) direction, due to the different channel dimensions. In addition, the quality of graphene and its monolayer character was confirmed by Raman spectroscopy, as shown in Figure 3.8(c). Raman spectra were measured on the bare $LiNbO_3$ substrate (red curve) and on the graphene Hall bar (black curve). In the spectrum of the substrate, only the 2LO peak from $LiNbO_3$ stands out (Fandan et al., 2020). Conversely, in the spectrum on graphene, the characteristic G and 2D peaks appear, related, respectively, to the presence of carbon and 2D graphene, as well as the D peak, which is related to the amount of defects in graphene (Ferrari et al., 2006). The ratio between the intensity of the 2D peak and the G peak takes a value of 2.1, indicating the monolayer nature of graphene (Bleu et al., 2019).

The first measurement to be performed was the acoustoelectric transport in the longitudinal direction, leading to an acoustoelectric voltage (V_{xx}). For that, the VNA was set so that a constant frequency signal was alternately sent through the ports 1 and 2 of the VNA, each of them connected to an IDT, with a switching period of 30 seconds. Meanwhile, the differential voltage between two consecutive electrodes along the x direction in the graphene Hall bar

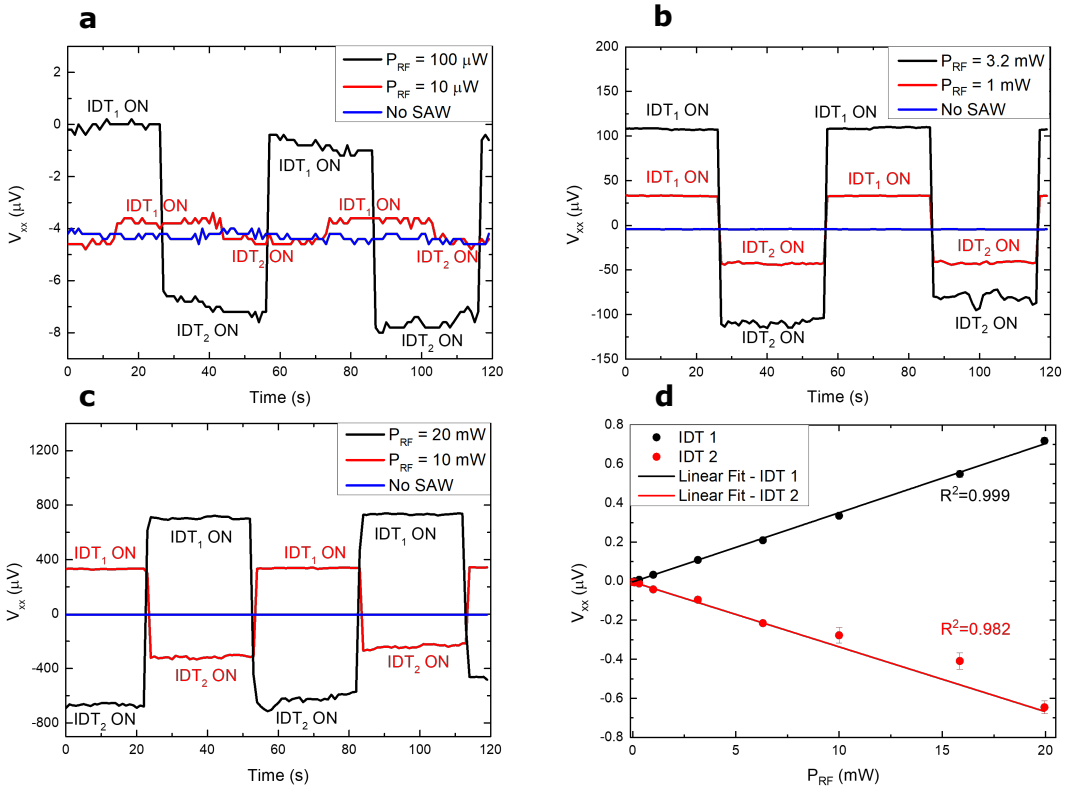

Figure 3.9: Acoustoelectric voltage (V_{xx}) generated across a 600 nm graphene channel at different incident RF power (P_{RF}) levels and a temperature of 16 K. Figures **a**, **b** and **c** show increasing power values compared to the base voltage when SAW is not present, whereas **d** represents the average voltage at the high/low states from the previous graphs.

was continuously monitored without setting any voltage between them. As seen in Figure 3.9, this differential voltage alternates between positive and negative values depending on which VNA port is active at each moment. The first measurement was taken with no RF power being delivered to the IDTs (blue curve in Figure 3.9 (a)), so any response deviating from this background level can be attributed to the carrier transport induced by the piezoelectric field of the SAW. In fact, at an RF excitation power as low as 10 μW (-20 dBm), a faint modulation of $\sim$ 400/800 pV is already detected, depending on the active IDT. When the RF power applied to the IDTs is increased, so is the amplitude of the voltage measured between the probes, clearly well above the level recorded when the SAW is not active. Values as high as $\sim$ 0.8 mV have been reached at a RF excitation power of 20 mW (13 dBm), the maximum power that the VNA can provide in a steady manner.

The generated voltage V_{xx} changes sign depending on which IDT is active, proving its acoustoelectric origin. However, it does not seem to be fully symmetric with respect to the IDT that is generating the SAW. This comes from the efficiency difference in the IDTs, with IDT 1 generating slightly higher acoustoelectric voltages. By averaging the acoustoelectric voltage throughout the time span in which each IDT is active, the acoustoelectric voltage can be graphically represented against the excitation RF power (see Figure 3.9 (d)). This

plot shows a linear trend for both IDTs when the applied RF power is expressed in Watts, with coefficients of determination (R^2) of 0.999 and 0.982 for IDT 1 and IDT 2, respectively. This agrees with previously reported results, both in graphene (Miseikis et al., 2012; Bandhu et al., 2013; Santos et al., 2013; Bandhu and Nash, 2014; Bandhu and Nash, 2016; Hernández-Mínguez et al., 2016) and in 2DEGs in semiconductor heterostructures (Shilton et al., 1995; Rotter et al., 1998, among others).

In addition to the acoustoelectric carrier transport associated with the piezoelectric field of the propagating SAW, the strain the SAW generates on the graphene layer is expected to induce a pseudo-magnetic field (Guinea et al., 2008; Levy et al., 2010; Vozmediano et al., 2010; Yeh et al., 2011; Kang et al., 2021). In turn, this pseudo-magnetic field is believed to produce a pseudo-Hall voltage in the direction transverse to SAW propagation (that is a V_{xy} voltage) when a current is flowing through graphene along the SAW propagation direction. It has to be mentioned that, during the realisation of this thesis, another research group reported already the observation of the pseudo-Hall voltage in SAW devices in graphene (P. Zhao et al., 2022) very similar to the ones described here.

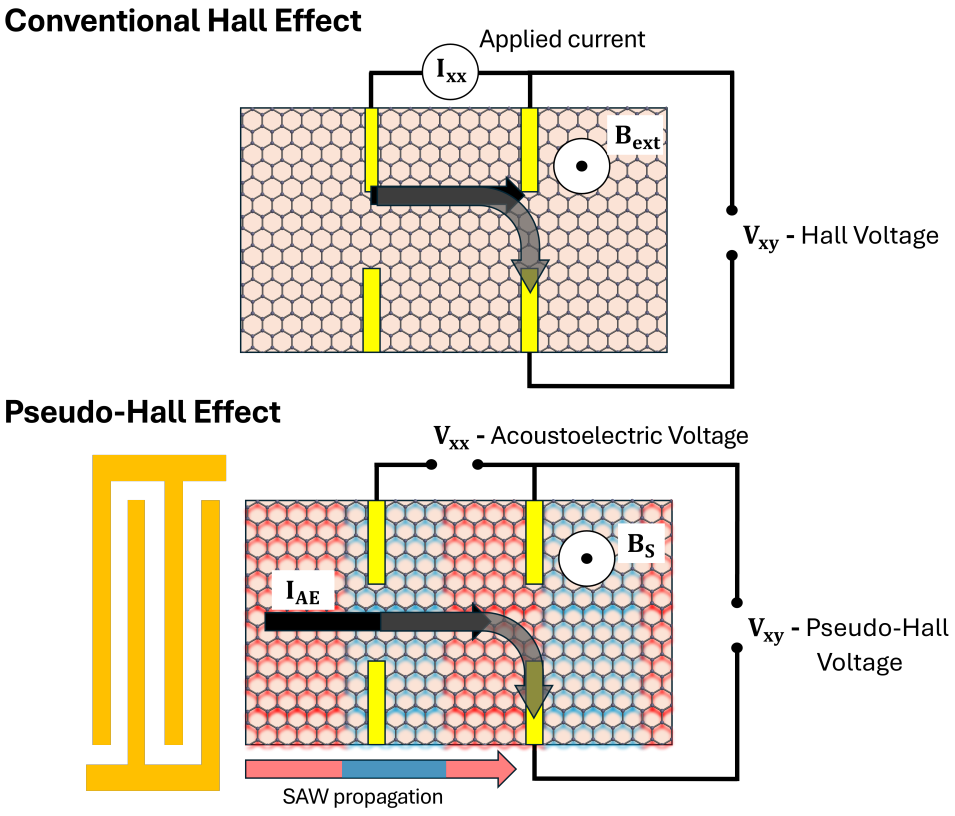

Figure 3.10: Schematic representation of conventional Hall and SAW-induced pseudo-Hall effects.

Thus, the fabricated device was used to study this pseudo-Hall voltage generated in graphene by the SAWs. The cryostat used for the measurements can only allocate 2 RF and 3 DC probes, thus imposing constraints on 4-probe DC measurements. Because of this, an experiment analogue to the acoustoelectric transport one was devised to measure the pseudo-Hall voltage,

but probing two electrical contacts transverse to the SAW propagation. In this way, the acoustoelectric current would replace the externally generated current of a conventional Hall effect experiment, as illustrated in Figure 3.10. This would allow for the observation of the pseudo-Hall voltage, but the acoustoelectric current and the pseudo-magnetic field would be correlated.

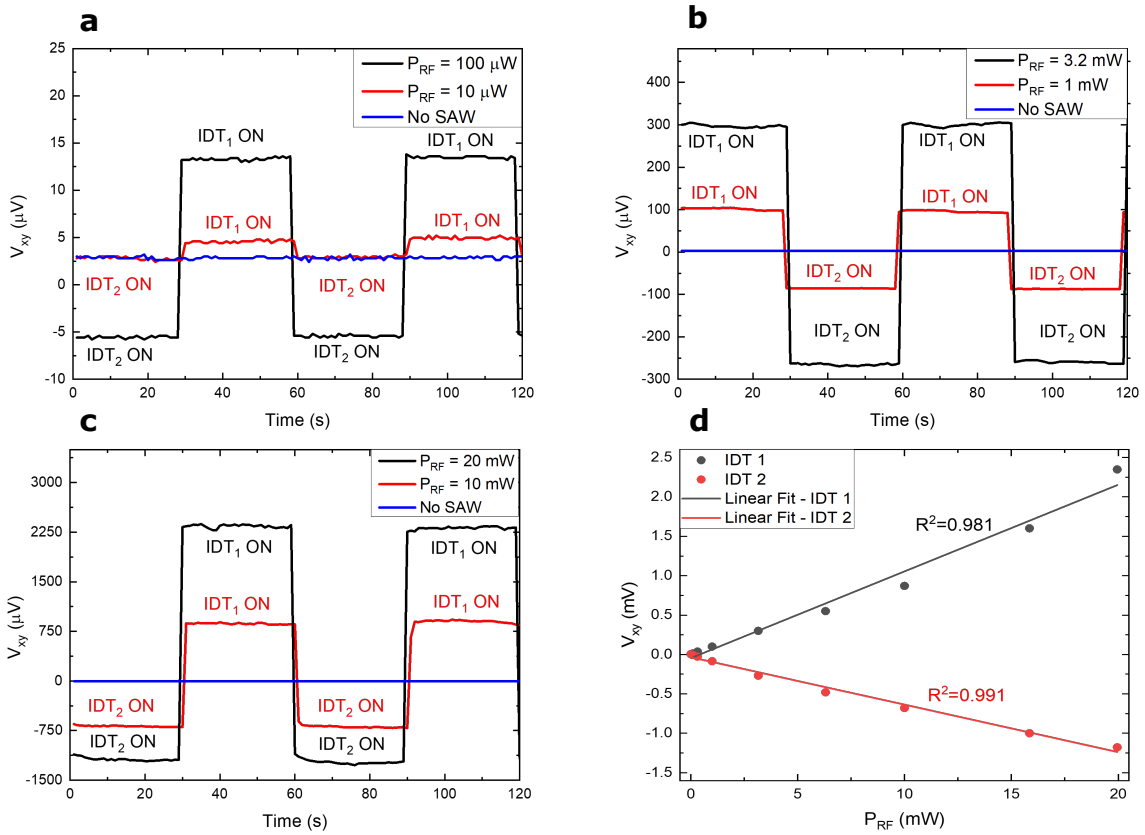

Figure 3.11: Pseudo-Hall voltage (V_{xy}) generated across a 3 μm graphene channel at different incident RF power (P_{RF}) levels and a temperature of 16 K. Figures **a**, **b** and **c** show increasing power values compared to the base voltage when SAW is not present, whereas **d** represents the average voltage at the high/low states from the previous graphs.

The results of these measurements are shown in Figure 3.11. Indeed, a V_{xy} voltage is observed between contacts in the direction perpendicular to the SAW propagation. In this case, the asymmetry that arises from the use of different IDTs is greater than in the case of the acoustoelectric voltage, but a pseudo-Hall voltage can be appreciated at incident RF power levels as low as 10 μW (-20 dBm), although only with one IDT. However, the magnitude of the pseudo-Hall voltage is greatly increased when increasing the incident RF power (see Figures 3.11 (a-c)). In this case, a change of sign is also observed depending on which IDT is active. Since the pseudo-magnetic effect relies on the strain generated by the SAW, it is irrespective of the SAW propagation direction. Therefore, this change of sign is solely due to the fact that the sense of the longitudinal current is generated by the piezoelectric field;

Hence, it depends on the sense of propagation of the SAW and thus on the active IDT, as was observed in Figure 3.9.

In Figure 3.11 (d), the pseudo-Hall voltage is represented as a function of the RF power fed to the IDTs. The graph also shows the linear regression to these data, showing a poorer correlation with a linear behaviour (R^2 values of 0.981 and 0.991 for IDT 1 and IDT 2, respectively) than the acoustoelectric voltage. A similar linear trend was experimentally reported contemporaneously to this experiment (P. Zhao et al., 2022). In this experiment, however, a substrate consisting of a thin (900-nm-thick) Y-cut $LiNbO_3$ layer on a SiO_2/Si substrate was used, that supports Bleustein-Gulyaev shear waves, instead of the Rayleigh mode used in this thesis. Pseudo-Hall voltage values as high as 2.25 mV have been measured at the highest incident power applied of 20 mW (13 dBm). Note that the channel length in this case is 3 μm, five times higher than the one in the acoustoelectric voltage measurements, and thus higher voltages are measured due to the increased resistance.

However, it has to be noted that there is a difference between the RF power applied by the VNA and the actual acoustic power that acts on the electron transport in the graphene channel between the IDTs, due to factors such as losses in the power delivery from the VNA port to the IDT, lack of calibration due to the reduced space in the cryostat, electrical-to-mechanical power conversion, and the transmission losses in the SAW path. Therefore, and since the graphene channel is in the centre between the IDTs, the actual SAW power in the region of interest can be calculated as (Fandan et al., 2020):

$$P_{SAW}(mW) = 10^{\frac{S_{21}(dB)/2}{10}} \times 10^{\frac{P_{RF}(dBm)}{10}}, \tag{3.2}$$

Using this equation to estimate the SAW power, the shape of the curves in Figures 3.9(d) and 3.11(d) should not change (see Figure 3.12), as this just rescales the values of the x axis by a factor that takes into account the value of S_{21}, which does not vary with power.

In this thesis, a Rayleigh wave has been considered as opposed to the Bleustein-Gulyaev wave employed by P. Zhao et al., 2022. Consequently, regarding the terms in Equation 1.15, $u_y = \partial u_j/\partial y = 0$. Therefore, following Equation 1.7, the in-plane displacement of a Rayleigh wave can be described by:

$$u_x = u_0 \cos(kx - \omega t), \tag{3.3}$$

and the pseudo-magnetic field it induces follows:

$$B_{Sz} = -\frac{\Delta}{ev_F}\frac{d(\ln\Delta)}{d(\ln a)}\frac{\partial^2 u_x}{\partial x^2}\sin(3\alpha) = \frac{\Delta}{ev_F}\frac{d(\ln\Delta)}{d(\ln a)}k^2 u_0 \sin(3\alpha)\cos(kx - \omega t). \tag{3.4}$$

Nevertheless, as argued by P. Zhao et al., 2022, such oscillatory pseudo-magnetic field would yield a zero net value when averaged over time, thus the origin of the pseudo-Hall voltage lies in second-order interactions between gauge fields. Taking into account the vector components of these fields, only the cross product between the pseudo-electric and pseudo-magnetic fields

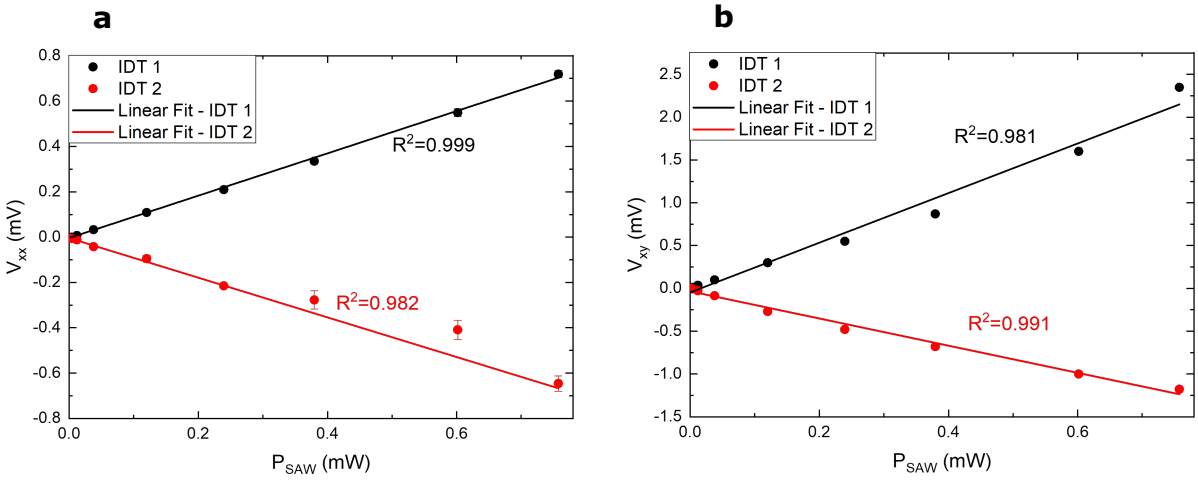

Figure 3.12: SAW-driven **a** acoustoelectric (V_{xx}) and **b** pseudo-Hall (V_{xy}) voltages in graphene as a function of SAW power (P_{SAW}) calculated with Equation 3.2, at temperature of 16 K.

($< \mathbf{E_S} \times \mathbf{B_S} >$) can lead to a transverse voltage with a nonzero time-averaged value. For that, the x-component of the pseudo-electric field is calculated as:

$$E_{Sx} = -\frac{\partial A_{Sx}}{\partial t} = -\frac{\partial}{\partial t}\left(\frac{\Delta}{ev_F}\frac{d(\ln\Delta)}{d(\ln a)}\cos(3\alpha)ku_0\sin(kx-\omega t)\right) = \\ = \frac{\Delta}{ev_F}\frac{d(\ln\Delta)}{d(\ln a)}\cos(3\alpha)\omega ku_0\cos(kx-\omega t). \tag{3.5}$$

Note that, although the Rayleigh and Bleustein-Gulyaev waves have different polarisations, the y-component of the pseudo-electric field does not contribute to the transverse voltage. Moreover, the cross-product between the gauge fields turns out to be the same. Hence, the steady-state pseudo-Hall voltage V_{xy} induced by a Rayleigh wave will be described by the same expression reported by P. Zhao et al., 2022 for a shear wave:

$$V_{xy} = \mu d < \mathbf{E_S} \times \mathbf{B_S} >= \frac{\mu d}{4}\left(\frac{\Delta}{ev_F}\frac{d(\ln\Delta)}{d(\ln a)}\right)^2(ku_0)^2\omega k\sin(6\alpha). \tag{3.6}$$

In addition, the same kind of SAW devices on b-$LiNbO_3$ substrates used in this section have been provided to colleagues from the Magnetic Devices Group at ISOM for them to study the dynamics of magnetic domain walls in ferromagnetic nanostrips under the action of a SAW. For that, magnetorresistance measurements were recorded to elucidate whether a magnetic domain had been nucleated with a current pulse, making histograms of the probability of nucleation under different external electric field values in absence or presence of SAW, as well as the dependence with the propagation direction of the SAW. Furthermore, micromagnetic simulations were carried out to study the temporal evolution in the system, concluding that

the SAW may be transferring linear momentum to the domain wall, which would cause the domain wall to propagate in a spring-like motion across the nanostrip (Rivelles et al., 2024).

3.3 Electrostatic Modulation of Fermi Level

By electrostatically tuning the Fermi energy of graphene through a gate voltage (Novoselov et al., 2004, 2005), a deeper study of the acoustoelectric carrier transport in graphene can be carried out. However, bulk $LiNbO_3$ samples (with a typical thickness of 500 μm) are too thick to permit the use of a back gate. Therefore, thin $LiNbO_3$ layers on various substrates with metallic interlayers have been used for the fabrication of SAW devices with buried gates. These heterostructures have been fabricated by Professors Samuel Margueron and Ausrine Bartasyte from the FEMTO-ST Institute (Besançon, France) using wafer bonding techniques (Clementi et al., 2021; Ouhabaz et al., 2024). In particular, the objective is of these structures is to permit the modulation of the Fermi level of graphene up to the CNP, so carrier inversion can be achieved, with aims to study the SAW-induced acoustoelectric and pseudo-Hall effects close to the CNP and under different doping conditions, providing either a 2DEG or a 2DHG. The capacitance provided by 300 nm of SiO_2 ($\varepsilon \sim 3.9$) is approximately twice as that provided by a $LiNbO_3$ layer ($\varepsilon \sim 50$, Preciado et al., 2015) with a thickness of 5-10 μm. Thus the CNP is expected to be reached within a gate voltage range of 0-200 V, even if the graphene has initially a certain residual doping arising from the transfer process or ambient contaminants.

3.3.1 $LiNbO_3$/Cr/Au/Cr/SiO_2/Si

The first structure studied consisted of a 5-μm-thick $LiNbO_3$ layer obtained by grinding a commercial 500-μm-thick wafer, which had been wafer-bonded through a 200-nm-thick Cr/Au/Cr metal layer to a 525-μm-thick Si wafer coated with 1.2 μm of SiO_2. The top layer was chosen to be undoped $LiNbO_3$, instead of black $LiNbO_3$ as in the bulk case previously described, so that it would have a higher dielectric constant and therefore worked better as a dielectric for the electrostatic doping of graphene. In this structure, the Cr/Au/Cr interlayer can act as a buried gate electrode. However, two potential issues were addressed in the first place: the compatibility of this structure with the previously described device fabrication process in black (doped) $LiNbO_3$, in which samples must be heated up and cooled down in the 20-200 °C range; and the preservation of the low-loss performance of SAW devices fabricated on a thin $LiNbO_3$ film on top of a metal layer instead of on the bulk $LiNbO_3$ previously used.

Hence, pieces of this material were subjected to heating and cooling cycles on the same hotplate and at the same rates and temperatures used during the fabrication process, while checking periodically under the optical microscope for the appearance of cracks in the material as a result of either the thermal expansion mismatch between the top and bottom layers or the combination of the piezoelectric and pyroelectric effects on the top $LiNbO_3$ layer, with a temperature gradient possibly leading to an electric field resulting in a contraction or expansion of the material. Nevertheless, these tests concluded that the samples could undergo the standard device fabrication process without any modification.

SAW resonators were thus fabricated on this material following the same procedure as for

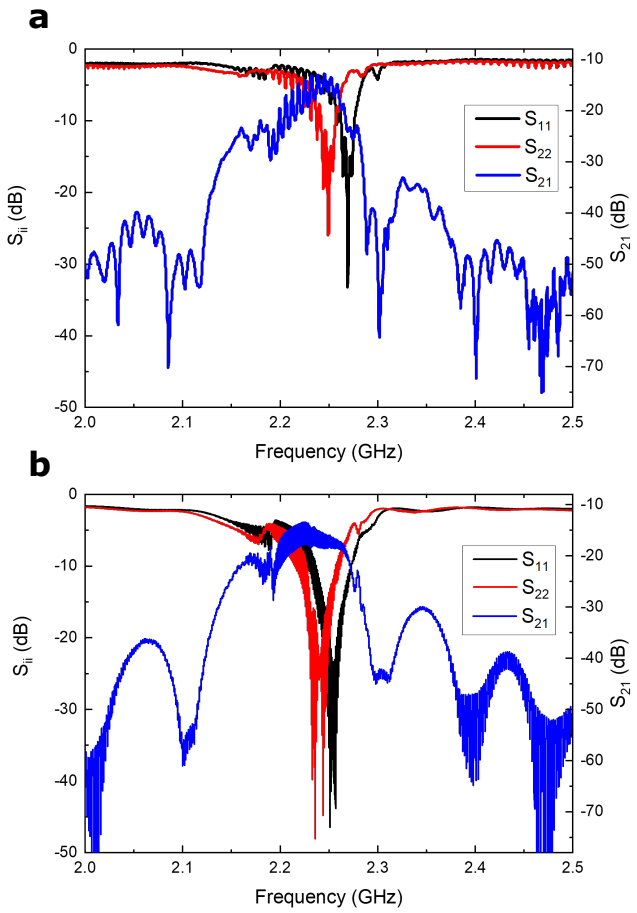

Figure 3.13: S parameters of a two-port SAW resonator with $\lambda_{SAW} = 1.6$ μm on **a** 5-μm-thick thin film $LiNbO_3$ on a Cr/Au/Cr/SiO_2/Si structure and on **b** bulk $LiNbO_3$.

bulk $LiNbO_3$. However, in order to preserve the low-loss performance of the SAW devices it was necessary to prevent the detrimental influence of the non-piezoelectric Si substrate underneath the $LiNbO_3$ film. Thus, $\lambda_{SAW} = 1.6$ μm has been the target wavelength. The magnitude of the S parameters of these devices, shown in Figure 3.13 (a), differs from those fabricated on the bulk material (Figure 3.13 (b)) by only ~ 2 dB, which was considered as a very good result taking into account the device-to-device variability and the benefits of this structure. A reduction of ~ 50 MHz is observed in the resonant frequency, presumably due to a difference in the sound velocity of both substrates. Therefore, there seem not to be any issues in the performance of the SAW devices due to the reduced thickness of the piezoelectric layer, approximately $3\lambda_{SAW}$, or the presence of the metal interlayer.

One last test was done to these structures concerning the capability to access the buried gold layer, as well as the range of tunability of the Fermi energy of graphene. With respect to the access to the gold layer, although it is visible from the edges of the wafer, its presence at the very edge of the diced samples cannot be taken for granted; thus a reliable method for accessing this layer was needed. The solution found consisted of polishing the sample from the edge at a certain angle, thus creating a bevel that exposed the gold layer at a certain

distance from the edge. Then, two large separated metal pads were defined on the bevel via EBL and metallisation along with the devices. By creating two different contacts in the bevel, the resistance between them can be determined and, if it is low, it means that both pads are connected through the buried gold layer, and thus they are suitable to probe it. A schematic of the final sample structure is shown in Figure 3.14.

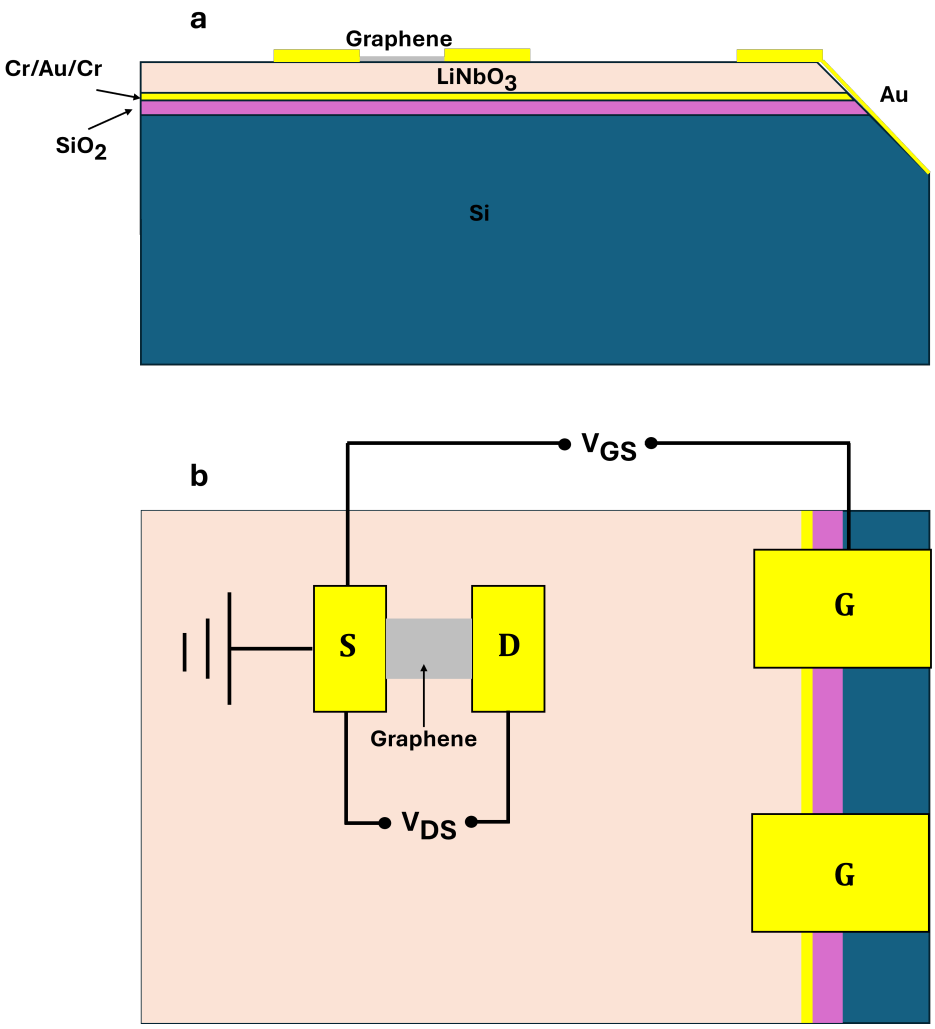

Figure 3.14: Schematic of the $LiNbO_3$/Cr/Au/Cr/SiO_2/Si structure with the bevel from **a** side and **b** top views, the latter including the schematic of the electrical connections to establish a drain (V_{DS}) and a gate (V_{GS}) voltage in the graphene devices.

Transmission Line Method (TLM) devices were fabricated on a sample with two bevels as a way to characterise the modulation of the Fermi energy of graphene, which was transferred and isolated from the bevel contacts by EBL and oxygen plasma etching, following the schematic shown in Figure 3.15. Two TLM contacts and the buried gate form a field-effect transistor (FET). The transfer characteristics of these FETs were measured. A 10 mV voltage was established between two metallic contacts and the voltage between the bevel contact (which acted as the bottom gate contact) and the source was swept from 0 to a certain value and back, so the final voltage between the gate and the drain is ensured to be 0 after the measurement.

The transfer characteristics shown in Figures 3.16, 3.17 and 3.18 were taken in a 3-μm-long channel. Note that, as shown in Figure 3.15, the mesa etch used in this case just isolates the whole set of TLM devices at the centre of the sample from the bevel contacts but the graphene channels between the contacts have not been defined, therefore there is a continuous layer of graphene connecting all TLM devices. Nevertheless, since graphene has a nonzero resistance, these devices can still be used as a first approximation to study the electrostatic doping of graphene avoiding another lithographic step.

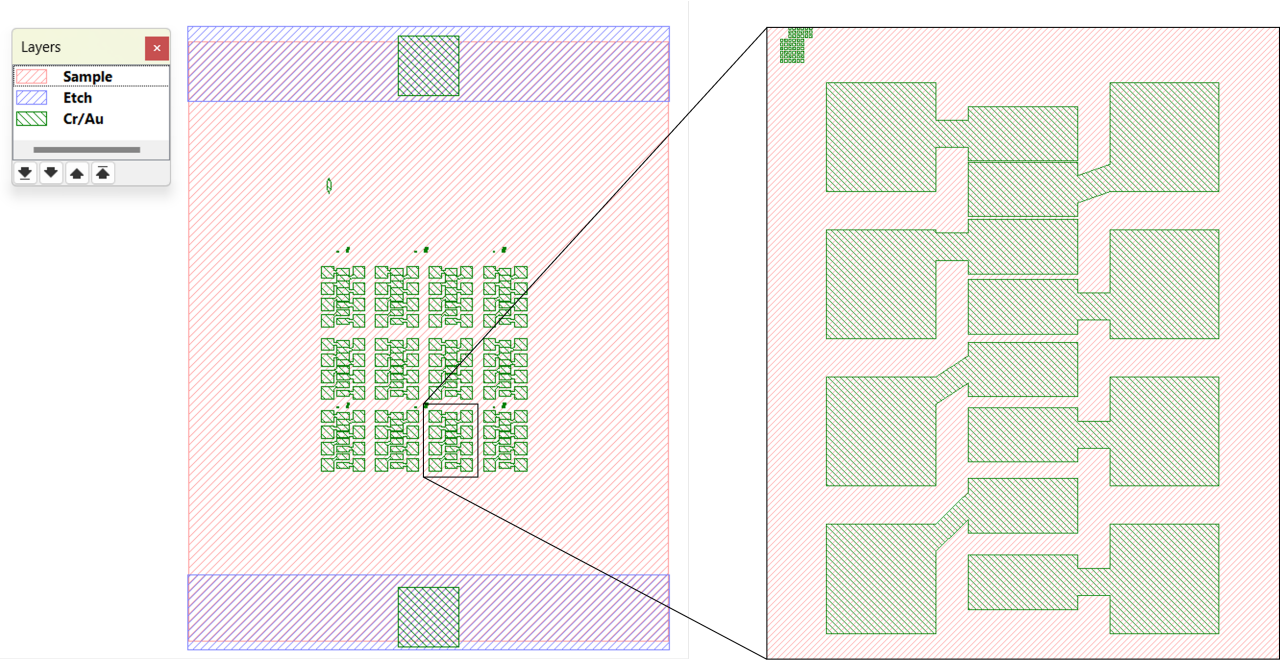

Figure 3.15: CAD of the TLM devices used to test the electrostatic carrier modulation in graphene on the $LiNbO_3$/Cr/Au/Cr/SiO_2/Si samples. The top and bottom electrodes contacting the Cr/Au/Cr layer are in bevels. The magnified view shows a detail of the TLM device.

At first, the gate voltage was scanned up to increasing maximum values ranging from 40 to 130 V, and back to 0 V, while both the drain current (I_{DS}) and the gate current (I_{GS}) were monitored. The first one was used to check whether the carrier density of graphene was being successfully modulated, whereas the second one allowed to check the current through the $LiNbO_3$ and prevent its dielectric breakdown. In these first measurements, as can be seen in Figure 3.16, a slight modulation of the carrier density with gate voltage can be observed as a decrease in the drain current. However, this modulation is still far from allowing access to the CNP, where the change from p- to n-type doping would be indicated by a minimum in the drain current. Furthermore, an increase in the gate current can be observed when the gate voltage increases, but this value is still below 250 nA for the first six cycles. However, upon reaching ~145 V (cycle #7), the gate current rapidly increases, reaching values 2 orders of magnitude higher than in previous measurements. It is thought that at this voltage the coercive field of $LiNbO_3$, which, for this crystal cut holds a value of 27 V/μm (Matic et al., 2017), has been overcome, leading to the polarisation of ferroelectric domains and conduction through the piezoelectric layer (Lu et al., 2019). Such high gate current suggests that the

Fermi level of graphene is not being modulated further. Therefore, the maximum modulation in the drain current achieved in this case is $\sim$ 18 % of its initial value over 130 V, achieved at the cycle #6.

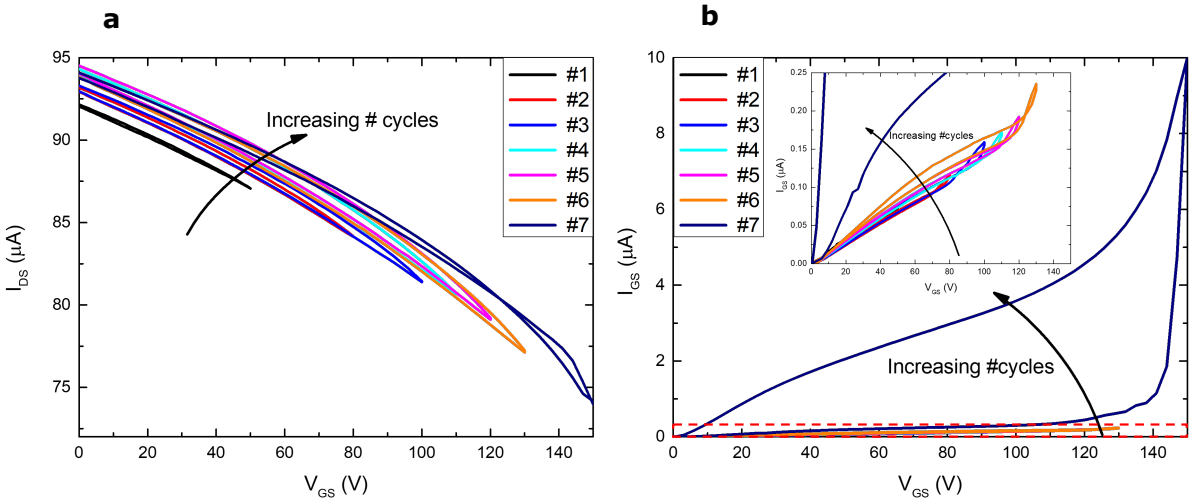

Figure 3.16: Change in the **a** drain current and in the **b** gate current with the gate voltage in successive cycles measured at room temperature. The inset in (b) represents a magnified view of the portion of the graph surrounded by red dashed lines, for visualising the details of the first 6 cycles.

As the sample experiences more cycles increasing the gate voltage, the drain current decreases faster but the gate current reaches higher values. This can be attributed to the exposure of the $LiNbO_3$ layer to higher electric field values. However, this decrease in the drain current cannot be attributed to a change in the conductivity of graphene. Instead, it can be ascribed to both drain and source contacts, connected through graphene and with a relatively small (10 mV) potential difference between them, acting as a sole contact. Therefore, this decrease in the drain current is attributed to an opposing current flowing from the drain to the gate. Furthermore, after continued exposure of the dielectric to electric fields beyond its coercive field (cycle in purple colour in Figure 3.17), the drain current changes sign, indicating not a change of the polarity of the carriers, which would keep the same current sign, but that the current flowing from drain to gate has finally overcome the current flowing from source to drain. Moreover, the polarisation of the ferroelectric domains is retained after the exposure to the electric field. Figure 3.18, compares the drain current in two identical cycles before and after exposure to high gate voltages, showing that the conduction through the ferroelectric is retained when the gate voltage is decreased.

In addition, two-port SAW resonators were fabricated with a set of electrical contacts in between IDTs using this structure, similar to those on bulk $LiNbO_3$, described in section 3.2, but with a shorter SAW wavelength (λ_{SAW} = 1.6 μm). Graphene was transferred on top of the sample and patterned into Hall bars in between the electrical contacts. Since the coercive fields increases strongly as the temperature decreases, the sample was then loaded into the cryostat to perform the transport measurements at low temperature and in vacuum. However, when the sample was cooled down, cracks appeared on its surface when a

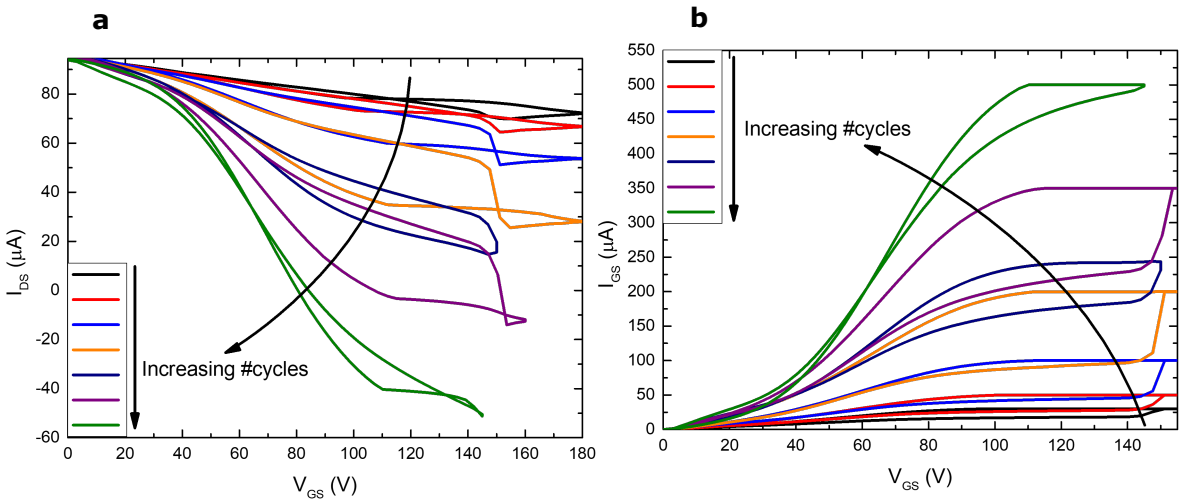

Figure 3.17: Change in the **a** drain current and in the **b** gate current with the gate voltage in successive cycles, measured at room temperature.

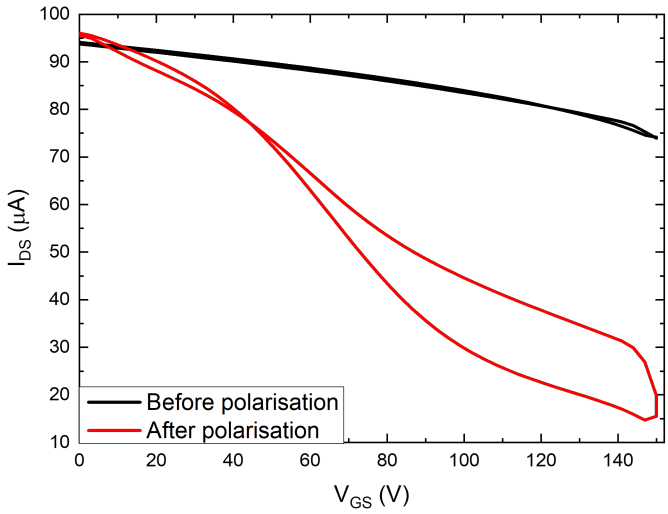

Figure 3.18: Change in the drain current in the $LiNbO_3$/Cr/Au/Cr/SiO_2/Si structure before and after the polarisation of ferroelectric domains, measured at room temperature.

temperature of $\sim$ 180 K was reached. Visually, these cracks appear sharp and parallel, in a direction perpendicular to the SAW propagation direction, as seen in Figure 3.19. Once the cracks appeared, it was no longer possible to excite SAWs in the IDTs. In order to check the likelihood of the occurrence of this issue, three unprocessed pieces of the same sample were introduced into the cryostat and cooled down. All of them presented cracks in the same range of temperature as the previous one. Due to the colour of the cracks, it seems that it is the top $LiNbO_3$ the layer that cracks, presumably along a cleavage crystal direction, exposing the gold layer underneath it. Two reasons are considered to be causing this effect: the combination of

the pyroelectric and piezoelectric effects of $LiNbO_3$, with which a temperature gradient would create an internal electric field that might stress the material; or the difference in the thermal expansion coefficients of $LiNbO_3$ along the direction perpendicular to the SAW propagation and of Si (which is the thickest layer of the heterostructure), which take values of 8.9 ppm/K (Mathews et al., 2019) and 2.6 ppm/K (Masolin et al., 2013), respectively. This difference in thermal expansion coefficients might result in an accumulation of mechanical stress that could be liberated in the form of cracks.

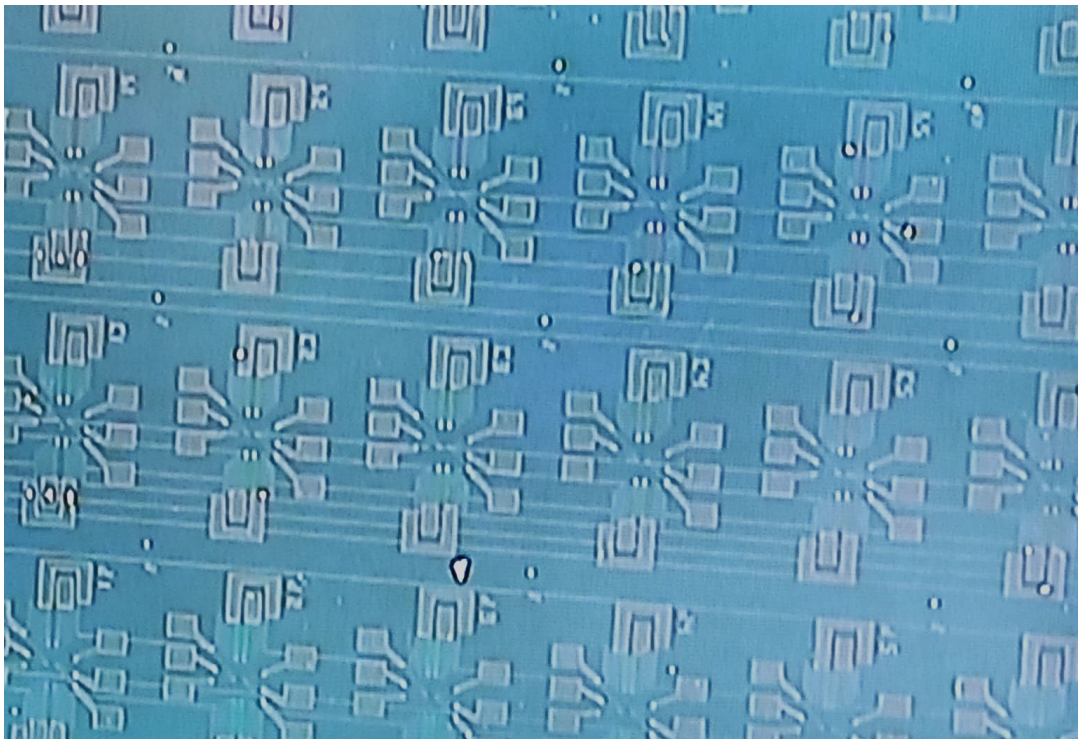

Figure 3.19: Cracks appeared in the $LiNbO_3$/Cr/Au/Cr/SiO_2/Si structure in the cryostat when cooling down the sample.

3.3.2 $LiNbO_3$/Cr/Au/Cr/b-$LiNbO_3$

With the objective of preventing the appearance of cracks at low temperature, the SiO_2/Si substrate was replaced by a 500 μm-thick black $LiNbO_3$ substrate. In this way, both thin film and substrate have the same thermal expansion coefficient, excluding one of the possible reasons for the appearance of cracks. This structure was shown to endure consecutive cycles of cooling down to 17 K and heating up to 500 K in the cryostat, either in a slow manner (with smooth temperature rates) or as fast as possible, as well as the heating up and cooling down steps of the device fabrication procedures. Thus, SAW devices were fabricated to test their performance on this substrate, which, as seen in Figure 3.20(a), does not present a significant disadvantage compared to those fabricated on bulk $LiNbO_3$ substrates.

Therefore, the electrostatic carrier modulation of graphene on this structure was subjected to test. In Figure 3.20(b), the effect on the drain current of several gate voltage cycles is shown. A modulation of up to 34% of the initial drain current is achieved in the first three cycles.

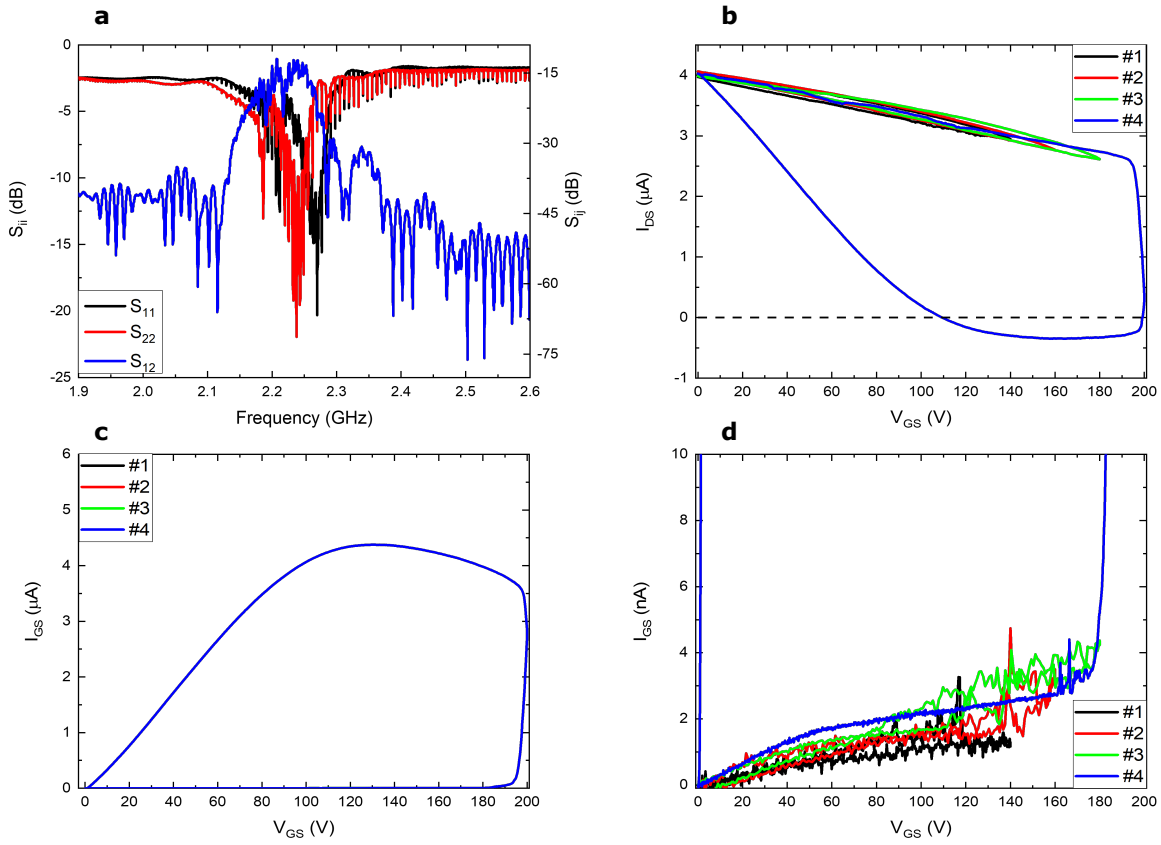

Figure 3.20: **a** S parameters of a two-port SAW resonator with λ_{SAW}= 1.6 μm. **b** Change in the drain current with the gate voltage in graphene Hall bars on the $LiNbO_3$/Cr/Au/Cr/b-$LiNbO_3$ structure. **c** Change in the gate current with the gate voltage in graphene Hall bars on the $LiNbO_3$/Cr/Au/Cr/b-$LiNbO_3$ structure. **d** Magnified view of (c) for a better view of the first 3 cycles. All measurements were taken at room temperature.

However, on the fourth cycle the coercive field for this structure at room temperature seems to have been overcome, leading to conduction through the $LiNbO_3$ layer, which is revealed by the change in the sign of the drain current, 3.20(c,d).

Nevertheless, a difference must be made between the conduction through the dielectric as a result of the polarisation of ferroelectric domains and the dielectric breakdown. In the first case, there is a current towards the gate coming from the drain and from the source, as shown in Figure 3.20; in the latter case, as shown in Figure 3.21, the drain current drops to 0, while a huge increase in the gate current is appreciated.

Devices comprising graphene Hall bars within two-port SAW resonators with a wavelength of 1.6 μm have been fabricated using the $LiNbO_3$/Cr/Au/Cr/b-$LiNbO_3$ structure. Figure 3.22 shows the acoustoelectric voltage generated in a graphene Hall bar 100 μm long and 75 μm wide under the action of SAWs generated with increasing RF power. Again, a linear relationship is found.

Nevertheless, these values of the acoustoelectric voltage shall not be compared directly with

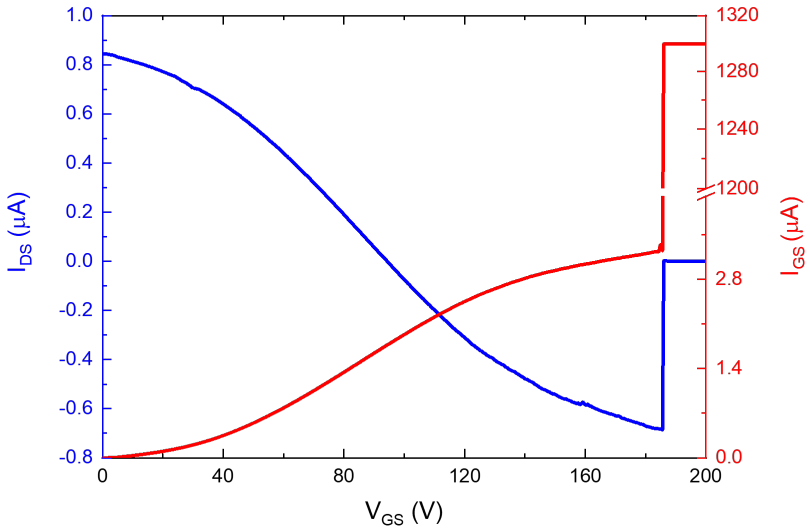

Figure 3.21: Dielectric breakdown of the top $LiNbO_3$ layer of the $LiNbO_3$/Cr/Au/Cr/b-$LiNbO_3$ structure, measured at room temperature.

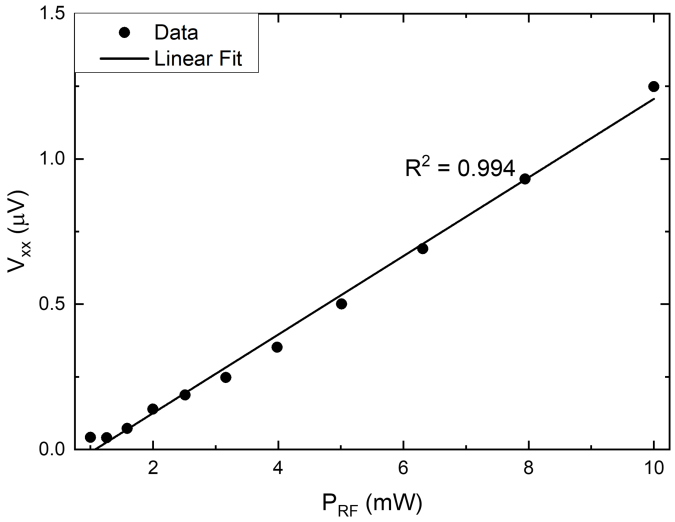

Figure 3.22: SAW driven acoustoelectric voltage (V_{xx}) in graphene on the $LiNbO_3$/Cr/Au/Cr/b-$LiNbO_3$ structure as a function of RF power (P_{RF}), measured at 16 K.

those of Figure 3.9, as a different measurement setup was used on this occasion. In order to perform a more precise measurement, a lock-in amplifier was used, instead of a SPA, to measure the acoustoelectric voltage. Figure 3.23 illustrates the two different experimental setups used. In this case, with the lock-in amplifier, the excitation signal fed to the IDTs was modulated with a square signal of a frequency of 350 kHz and 50% duty cycle using a signal generator and a switch. The modulation signal was used as a reference signal for the

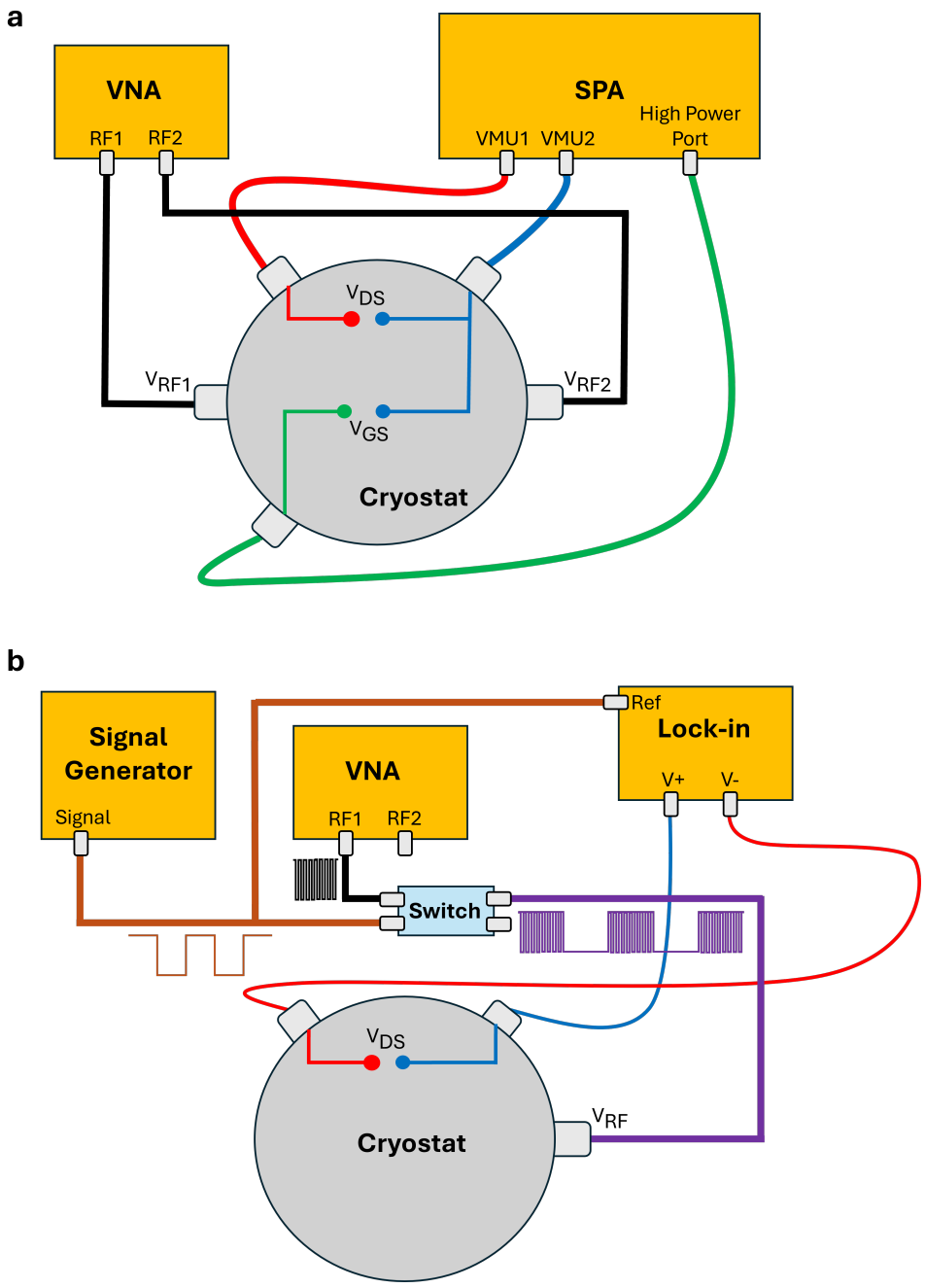

Figure 3.23: Illustration of the experimental setups used for the acoustoelectric measurements, using **a** an SPA or **b** a lock-in amplifier for voltage detection.

demodulation in the lock-in amplifier (see Figure 3.23(b)). Therefore, the measured signal was different due to the working principle of lock-in detection (ZurichInstruments, 2023). Furthermore, additional losses appear in this setup, as compared with the one with the SPA shown in Figure 3.23(a), produced by the switch. However, the noise in the measurement is reduced by means of two mechanisms: first, thermal instabilities are reduced because of the half period during which the SAW is not generated due to the modulation signal; and

second, because of the demodulation from the lock-in amplifier, which eliminates white noise by measuring signals of the same frequency as the one modulating the SAW.

Table 3.1 summarises the properties of the different $LiNbO_3$-based substrates used for performing acoustoelectric measurements in graphene, where partial field-effect E_F modulation indicates that there is a modulation of the conductivity of graphene, although it does not fulfill the initial objective of reaching the CNP. In conclusion, the $LiNbO_3$/Cr/Au/Cr/b-$LiNbO_3$ solves the issue with the endurance to low temperature, which is a desirable condition for the transport measurements as it reduces the electron scattering and thus enhances the signal-to-noise ratio. Nevertheless, further studies need to be done concerning the modulation of the Fermi level of graphene on the ferroelectric $LiNbO_3$ thin films.

Structure	**Low-loss SAW Generation**	**Field-effect E_F Modulation**	**Low Temperature Endurance**
b-$LiNbO_3$	Yes	No	Yes
$LiNbO_3$/Cr/Au/Cr/SiO_2/Si	Yes	Partial	No
$LiNbO_3$/Cr/Au/Cr/b-$LiNbO_3$	Yes	Partial	Yes

Table 3.1: Capabilities of the different $LiNbO_3$-based structures studied.

Chapter 4

SAW-driven Graphene Plasmons for Biosensing

In this chapter, a SAW-driven graphene-based plasmonic biosensor, as the one depicted in Figure 4.1, is discussed. The biosensor structure is designed to tailor the SPPs in the energy range required for fingerprinting biomolecules, while maintaining a SAW wavelength that can ensure a reliable device fabrication. Here, SAW devices with wavelengths in the sub-micrometre range (0.3-0.4 μm) have been considered, as they are still accessible through EBL and allow to generate polaritons in the frequency range where the resonances of the amide bands, that characterise the vibrations of proteins and peptides, lie. The performance of the biosensor is first tested with an organic polymer with sharp and intense absorption lines to facilitate the understanding of the sensing mechanisms. A coupled oscillators model is introduced to fit the calculated extinction curves and to quantify the SPP-analyte interaction. Finally, calculations of the biosensor performance fingerprinting ultrathin biolayers of significant biological substances with weaker and broader resonances such as protein bilayer and peptide monolayers (MLs) are presented.

4.1 Biosensor Design

Graphene, being a conductive material, supports surface plasmon polaritons in the mid-IR range that, because of the low slope of their dispersion curve, exhibit great wavelength confinement. In order to use graphene SPPs for fingerprinting organic molecules, it is necessary to access the spectral region in which most vibrational resonances of organic materials lie. In particular, biomolecules such as proteins and peptides are often characterised by their amide bands, which typically span in the range of 1500-1700 cm^{-1}. However, because of the low slope of the dispersion curve, a large wavevector mismatch is needed to be overcome to couple far-field light into graphene SPPs (Brar et al., 2013; Z. Fang et al., 2014).

A 2D system formed by two double layer graphene (DLG) stacks separated by h-BN (DLG/h-BN/DLG) is then placed in between the IDTs, so that a standing SAW is established across the van der Waals heterostructure. The SAW acts as a virtual diffraction grating providing the

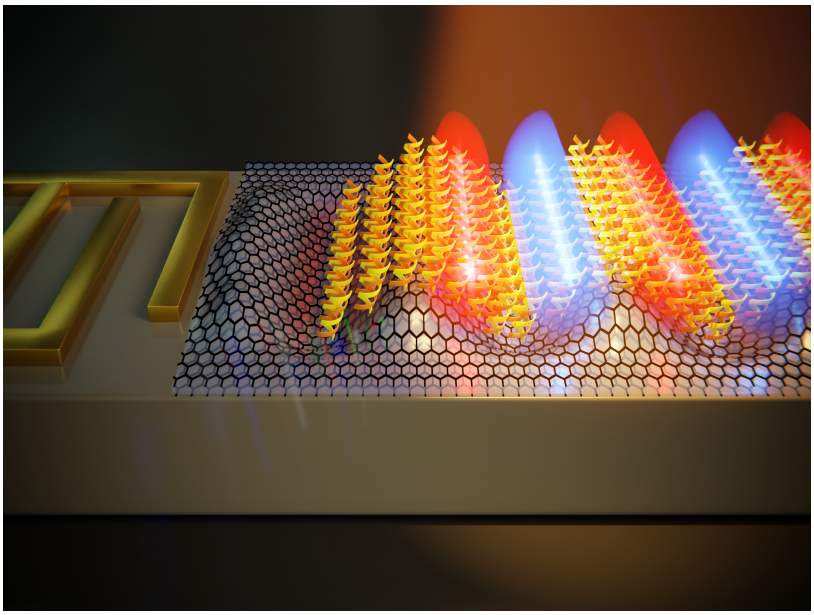

Figure 4.1: Artistic illustration of the SAW-assisted plasmonic biosensor ("Fingerprinting biomolecules with the help of sound", Last accessed 2024).

extra momentum necessary to couple far field TM-polarized light into the SPPPs supported by the 2D system. A quantum cascade laser can be used as the mid-infrared light source, since it permits to deliver coherent and polarised light with high spectral power density (Schwaighofer et al., 2018) concentrated in the active region of the sensor. The analyte is finally deposited on top forming an ultrathin layer. The sensor monitors the plasmonic response of the whole structure, which is modified by the coating, allowing the identification or fingerprinting of the analyte and the quantification of its thickness down to the single monolayer limit (Izquierdo-López et al., 2023).

Hence, the SAW, acting as an electrically-controlled virtual diffraction grating, can switch on and off the polariton, unlike in standard systems, such as patterned diffraction gratings, where the polariton is always present. This provides the proposed biosensor with an important advantage since the differential measurement is always made with the analyte already in place for the SAW ON and OFF conditions, instead of standard plasmonic biosensors using patterned gratings, where measurements need to be made before and after placing the analyte (unless the light polarization is rotated, which is a slow process), thus being potentially affected by other effects distinct from the mere analyte. Moreover, by avoiding the patterning of graphene, a higher carrier mobility is retained in graphene as compared as that of other techniques such as graphene nanoribbon fabrication (Li et al., 2014; H. Hu et al., 2016).

However, since reaching high wavevector values is highly challenging using SAWs, where the size of the fingers of the IDTs will be a quarter of the wavelength of the SPPs, the wavevector values considered in this study will be restricted to those below 2.5×10^7 m^{-1}, which corresponds to a wavelength of 250 nm. Figure 4.2 shows schematics of the 3D layout of the device (a) and the cross section of the van der Waals heterostructure that forms of the biosensor (b). In the following sections, the motivations behind this choice of heterostructure

and the strategies followed to increase the energy of the polaritons will be discussed.

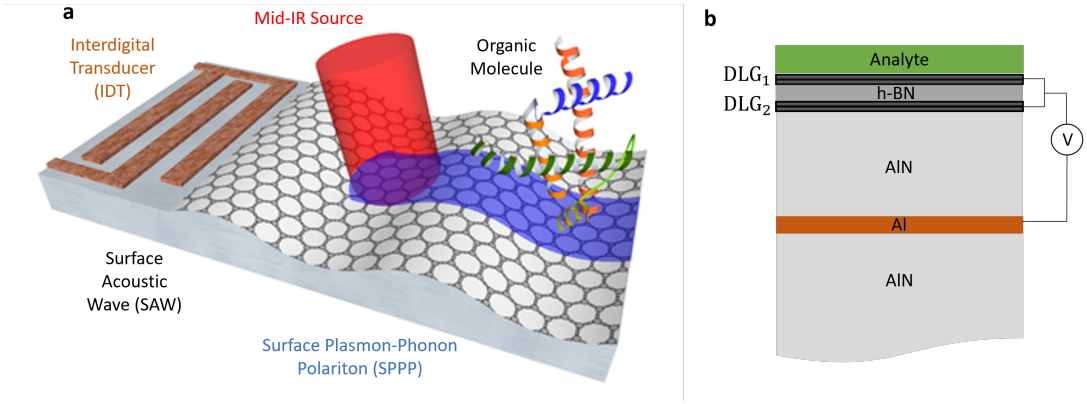

Figure 4.2: Schematics of the SAW-driven plasmonic biosensor proposed. **a** 3D layout of the device and **b** cross section of the material system composed of a van der Waals heterostructure on top of an AlN substrate with a buried Al gate that is used to bias the top and bottom DLG stacks.

4.1.1 Tailoring the Polariton Dispersion

A piezoelectric substrate is needed to generate the SAWs that will act as a virtual diffraction grating. The proposed biosensor consists of a two-port SAW resonator fabricated on a piezoelectric substrate. $LiNbO_3$, although employed in the previous chapter for acoustoelectric transport measurements, has been disregarded for plasmonic applications due its various phonon lines spanning the low-energy part of the mid-IR range (Barker and Loudon, 1967), which would hinder tailoring high-energy polariton modes to reach the fingerprinting range. Thus, AlN has been the material of choice as piezoelectric substrate because of its reduced number of phonon lines in the mid-IR range and the possibility of burying an Al electrode which can be used for the electrostatic doping of the graphene sheet. This Al electrode could be fabricated during the epitaxial growth or sputtering deposition of the material in the form of an AlN/Al/AlN stack. AlN exhibits surface optical phonons which, being a polar material, will interact with mid-IR radiation as well as with charge carriers in graphene, giving rise to hybrid radiation modes (Schiefele et al., 2013; Fandan et al., 2018). In this way, SPPPs will arise from the anticrossing between the SPPs and the AlN phonons at frequencies $\omega_{TO} = 669$ cm^{-1} and $\omega_{LO} = 895$ cm^{-1} (Kazan et al., 2009).

In Figure 4.3(a), the plasmon dispersion of a single layer graphene (SLG) on an AlN substrate is shown. In order to access the fingerprint region, wavevector values in the range of $6 - 10 \times 10^7 m^{-1}$ are needed, resulting in SAW wavelengths of 60-100 nm, which are extremely small for a reliable IDT fabrication. By restricting to wavevector values below $2.5 \times 10^7 m^{-1}$, the highest frequency available for the polariton would be 1110 cm^{-1} for the $SPPP_2$ branch, still far from the amide bands.

An approach to increase the slope of the plasmon dispersion consists in increasing the number of graphene layers. If these layers are CVD grown and transferred onto the substrate, there is no determined orientation between their crystal domains, and interactions resulting from a

specific type of stacking are avoided. Therefore, as shown by Rodrigo et al., 2017, a DLG can be thought of as an SLG with twice the Fermi energy, which would increase the slope of the dispersion curve compared to the one of an SLG. For comparison, Figure 4.3 compares the $SPPP_i$ dispersion of a SLG (a) and a DLG (b) on top of AlN. It is clear that the polariton branches are shifted towards higher frequencies in a DLG with respect to those of a SLG, in the same way as they would at increasing Fermi energies, while no extra branches appear.

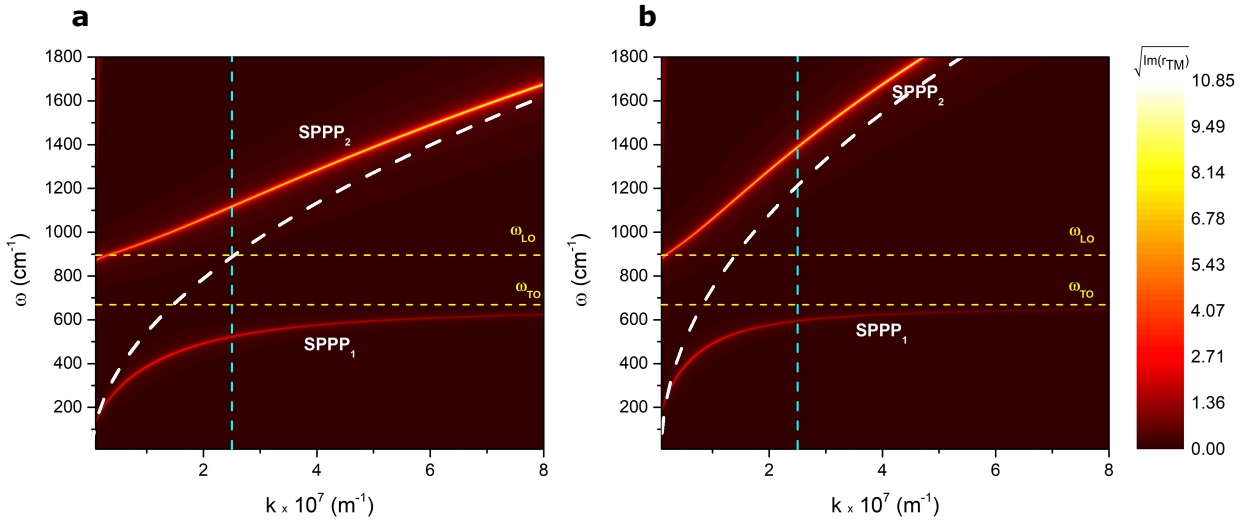

Figure 4.3: **a** Dispersion of surface plasmon-phonon polaritons $SPPP_i$ for a SLG on an AlN substrate. The Fermi energy of the graphene layer is 0.4 eV. For reference, the dispersion of a SLG on a substrate without phonons with the same static permittivity as AlN is shown as a white dashed line. **b** $SPPP_i$ dispersion of a DLG on an AlN substrate. A Fermi energy of 0.4 eV is assumed for each of the graphene layers. For reference, the dispersion of a DLG on a substrate without phonons with the same static permittivity as AlN is shown as a white dashed line. In both plots, horizontal yellow dashed lines are depicted at the frequencies of AlN phonons, as well as a vertical blue dashed line indicating the $k = 2.5 \times 10^7 m^{-1}$ value, which corresponds with a wavelength $\lambda = 250$ nm, which is the maximum wavevector considered in this work due to increasing lithographic issues beyond it. The maximum frequency achievable at this wavevector is $\omega \sim 1110$ and 1390 cm^{-1} for SLG and DLG, respectively.

Unlike AlN, h-BN is a strongly anisotropic material with two reststrahlen bands defined by its active phonon modes, the in-plane ($||$) A_{2u} phonons at $\omega_{TO,||} = 774$ cm^{-1} and $\omega_{LO,||} = 823$ cm^{-1} and the out-of-plane ($\perp$) E_{1u} phonons at $\omega_{TO,\perp} = 1363$ cm^{-1} and $\omega_{LO,\perp} = 1605$ cm^{-1} (Dai et al., 2014). Therefore, a thin h-BN layer may be deposited below the graphene sheet, not only increasing its mobility, but also enabling the appearance of SPPP modes in the fingerprinting region because of the frequency range of its upper reststrahlen band. Furthermore, by increasing the thickness of this h-BN layer, the polaritons will have a more intense phononic character, increasing the lifetime of the resulting modes due to the low damping rate of the phonons of h-BN. In addition, as the h-BN thickness increases, hyperbolic modes develop in the upper reststrahlen band (Fandan et al., 2018). This reduces the possibility of tuning the frequency of the most prominent modes via gate voltage, as the

polariton branches will be locked to the phonon frequencies.

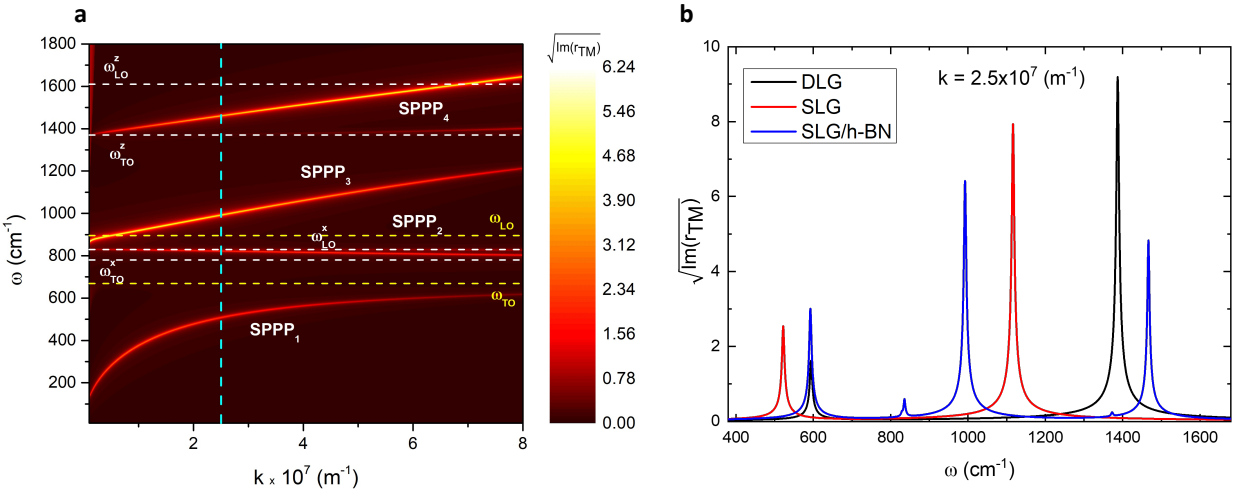

Figure 4.4: **a** Dispersion of surface plasmon-phonon polaritons $SPPP_i$ for a SLG/h-BN/AlN structure, where the h-BN thickness is 10 nm and the Fermi energy of graphene is 0.4 eV. Yellow and white dashed lines are displayed at the frequencies of AlN and h-BN phonons, respectively, while a blue dashed line marks $k = 2.5 \times 10^7 m^{-1}$. **b** Cross section of the dispersion plots of SLG/AlN, DLG/AlN and SLG/h-BN/AlN at $k = 2.5 \times 10^7 m^{-1}$.

A thin h-BN layer below the graphene not only creates hybrid SPPP modes (Figure 4.4(a)), but also allows to increase the frequency they span, as shown in Figure 4.4(b), which compares the cross-sections of the dispersion curves of the SLG/h-BN/AlN structure, SLG/AlN and DLG/AlN structures for a wavevector value of $k = 2.5 \times 10^7 m^{-1}$. This figure shows that the introduction of the h-BN interlayer allows to extend the SPPP frequency range up to ~ 1470 cm^{-1}, which, despite being close to the fingerprint regions, does not still reach the amide bands. However, the extinction of the peaks is lower than in the SLG/AlN and DLG/AlN structures.

Moreover, instead of consecutively transferring the two graphene layers of a DLG, a thin h-BN spacer layer can be transferred in between them. In this case, the resulting stack consists of two plasmon-supporting layers separated by a dielectric with polar phonons. Therefore, besides the optical modes, a set of acoustic modes will appear at higher wavevector vlues.

In figure 4.5, the SPPP dispersion of the SLG/h-BN/SLG/AlN and DLG/h-BN/DLG/AlN systems are plotted. Note that for the latter, a fingerprinting range of up to 1770 cm^{-1} is accessible at $k = 2.5 \times 10^7 m^{-1}$, covering both the Amide I and Amide II bands. Smaller wavevectors can be used to access other characteristic vibrational resonances of the fingerprinting region. A 2 nm h-BN thickness has been used to compute these dispersions, since calculations have revealed that this is the optimum value to probe the Amide I region. Note the appearance of acoustic ($SPPP_1^A$) as well as optical ($SPPP_i^O$) modes, which will be discussed later in this chapter.

With aims to electrostatically tune the Fermi energy of graphene and therefore the frequency

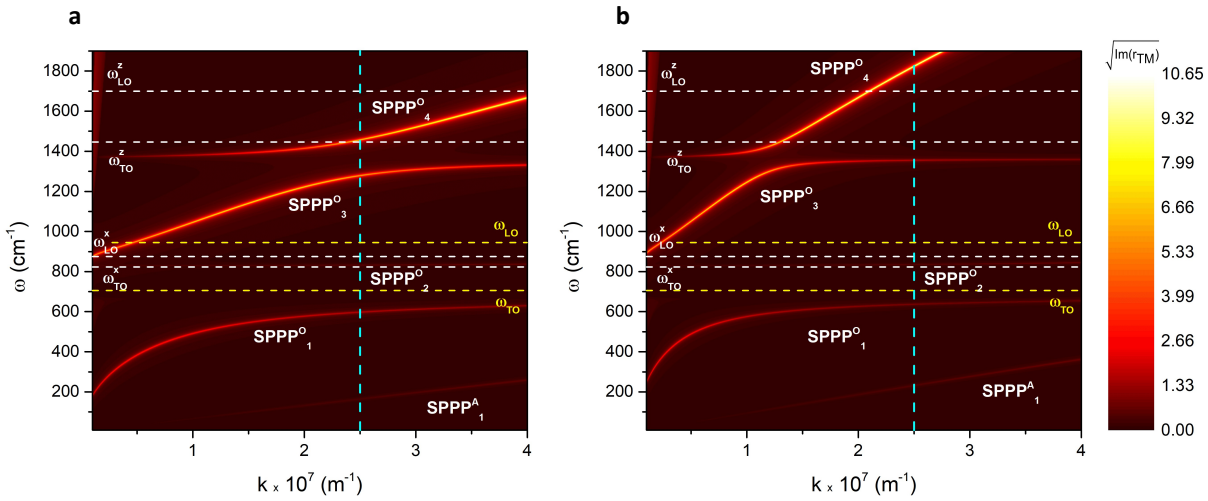

Figure 4.5: **a** Dispersion of surface plasmon-phonon polaritons $SPPP_i$ for a SLG/h-BN/SLG/AlN system. **b** Dispersion of $SPPP_i$ for a DLG/h-BN/DLG/AlN system. In both cases, the h-BN thickness is 2 nm and the Fermi energy of graphene is 0.4 eV. Yellow and white dashed lines are displayed at the frequencies of AlN and h-BN phonons, respectively, while a blue dashed line marks $k = 2.5 \times 10^7 m^{-1}$. At this wavevector value, the maximum frequency achievable is $\omega \sim 1450$ and 1800 cm^{-1} for the SLG- and DLG-based systems, respectively.

of the polariton, the AlN substrate can be replaced with an AlN/Al/AlN stack. The buried Al layer can act as a back gate electrode in a FET configuration, with the top AlN as the insulating layer. Figure 4.6 shows that, if the upper layer of AlN is sufficiently thick (500 nm), a thin (5 nm) Al layer can be introduced without distorting the polariton dispersion. This electrode will enable the polariton to be actively tuned, scanning a spectral region to probe several different vibrational resonances of the analyte for its fingerprinting. Moreover, since the dielectric constant of AlN has a value of 7.37, a 500-nm-thick AlN insulating layer in between the Al gate electrode and the graphene yields a capacitance similar to a 300-nm-thick SiO_2 dielectric layer, commonly used in graphene devices.

4.1.2 Optical and Acoustic SPPPs

Since the heterostructure includes two conductive systems separated by a spacer, its polariton dispersion will host two different sets of resonances, corresponding to the optical and acoustic modes arising, respectively, from the in-phase and out-of-phase coupling between the plasmons supported by both DLGs. Although in Figure 4.5 only the lowest-energy acoustic branch $SPPP_1^A$ is shown, more branches appear when depicting a broader wavevector range as a consequence of the interaction of graphene plasmons with the active phonons of AlN and h-BN.

Figure 4.7 depicts the dispersion of the surface plasmon-phonon polaritons $SPPP_i$ for the DLG/h-BN/DLG/AlN/Al/AlN system, as shown in Figure 4.5, but over an extended wavevector range so that all the acoustic $SPPP_i^A$ modes can be observed up to the fingerprint region.

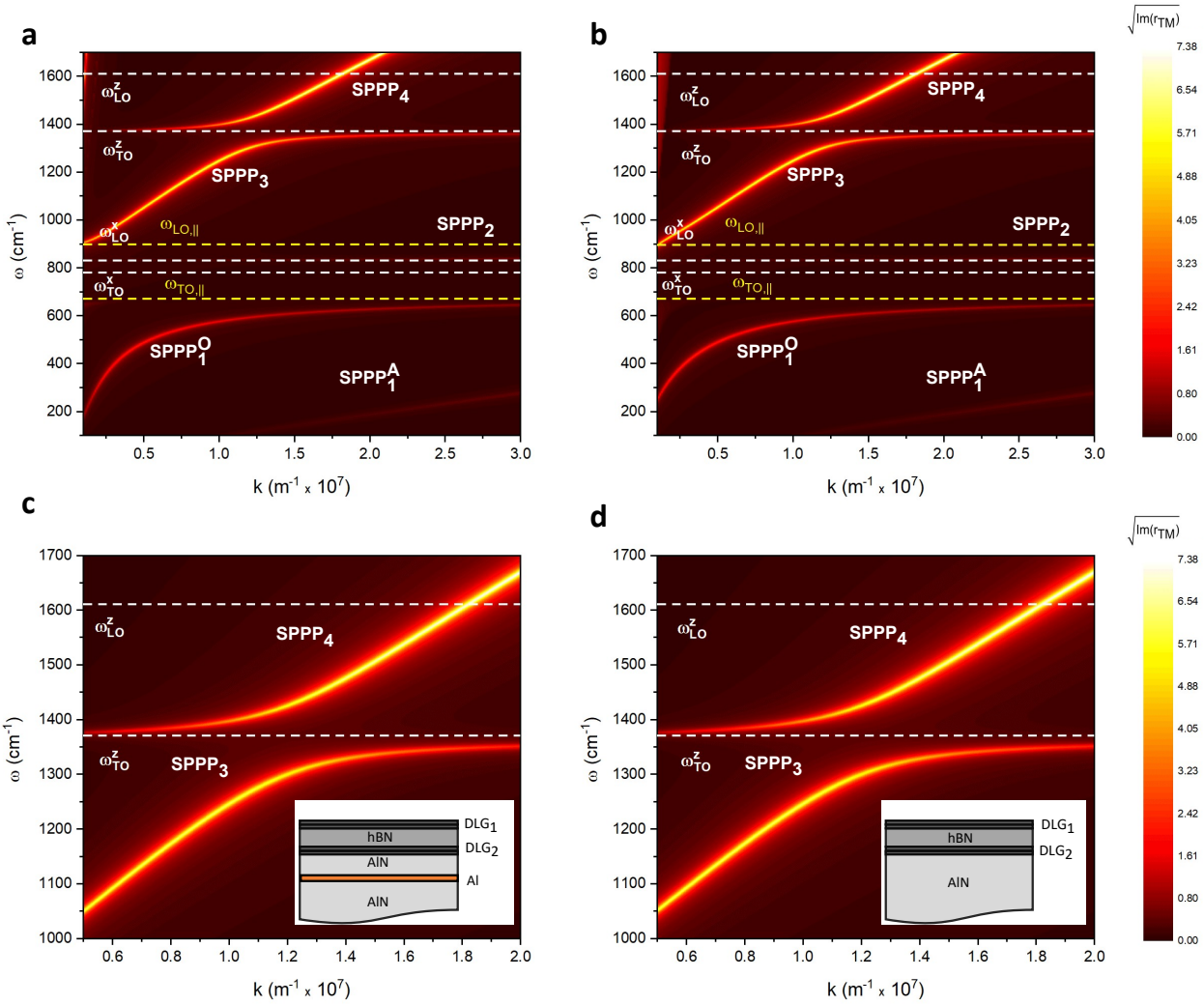

Figure 4.6: Dispersion of surface plasmon-phonon polaritons $SPPP_i$ for the DLG/h-BN/DLG/AlN/Al/AlN system with (**a**,**c**) and without (**b**,**d**) a 5 nm-thick Al electrode buried between 500 nm-thick (top) and semi-infinite (bottom) AlN layers. The Fermi levels of all graphene sheets is set to $E_F = 0.4$ eV and the h-BN layer is 2 nm thick. White and yellow dashed lines indicate the optical phonon frequencies of h-BN and AlN respectively. (c,d) are magnified views of (a,b), respectively, with an inset representing the heterostructure simulated in each case.

In particular, a wavevector $k = 15.3 \times 10^7 m^{-1}$, which would correspond to a SAW $\lambda_{SAW} \approx$ 40 nm, is needed to reach a frequency of 1500 cm^{-1} for the $SPPP_4^A$ mode. As discussed in Chapter 2, normal incidence is considered and thus the polariton wavelength takes the same value as the SAW wavelength.

On the one hand, acoustic modes, being present at larger wavevectors than the optical ones, have smaller wavelengths and therefore exhibit smaller mode volumes than their optical counterparts, locally increasing the energy density. In particular, the $SPPP_4^A$ mode presents a wavelength 10 times smaller than that of the $SPPP_4^O$ mode, but it demands a lithography

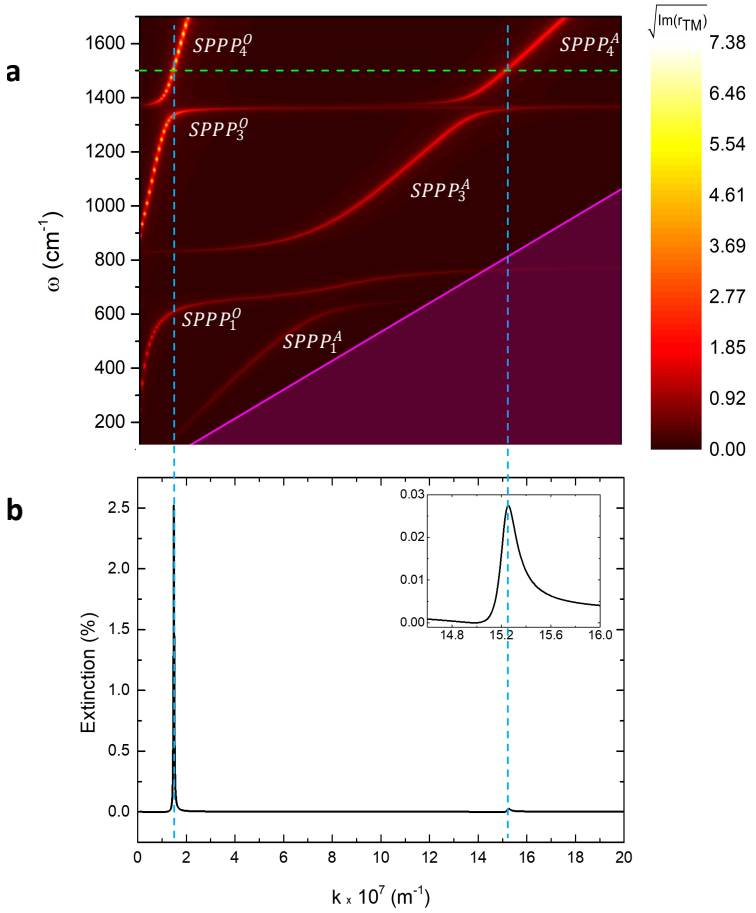

Figure 4.7: **a** Dispersion of the surface plasmon-phonon polaritons SPPP_i for the DLG/h-BN/DLG/AlN/Al/AlN system over an extended wavevector range. $\mathrm{SPPP}_i^{\mathrm{O}}$ and $\mathrm{SPPP}_i^{\mathrm{A}}$ denote the optical and acoustic modes, respectively. The green dashed line marks a frequency of 1500 cm^{-1} and the blue dashed lines indicate the wavevector values of the optical and acoustic branches at this frequency. The magenta-shaded region corresponds to the intraband transitions region of the dispersion. **b** Extinction as a function of the wavevector for the optical $\mathrm{SPPP}_4^{\mathrm{O}}$ and acoustic $\mathrm{SPPP}_4^{\mathrm{A}}$ modes at a frequency of 1500 cm^{-1}. The inset shows an enlarged view of the extinction of $\mathrm{SPPP}_4^{\mathrm{A}}$.

beyond the state-of-the-art resolution limit of an IDT, which is in the order of $\lambda_{\mathrm{SAW}} \approx 160$ nm nowadays. It should be noted that for standard (50%-metallisation ratio) IDTs with $\lambda_{\mathrm{SAW}} = 40$ nm, 10 nm features must be patterned. Although recent advances in lithographic technologies might pave the way towards such small dimensions in the near future (Cattoni et al., 2018; Chen et al., 2021), fabricating these devices will still pose a considerable challenge. On the other hand, due to the proximity of the acoustic branches to the intraband transitions region, they suffer from a strong Landau damping, as indicated by the decrease in the color-scale value of these branches in Figure 4.7(a). Note, for instance, a gradual fading of $\mathrm{SPPP}_1^{\mathrm{A}}$ when getting closer to the region dominated by intraband transitions ($k > k_F$ shaded in purple). In the particular case of the $\mathrm{SPPP}_4^{\mathrm{A}}$ mode, this turns into a 100-fold reduction in the extinction

at 1500 cm^{-1} compared to the $SPPP_4^O$ mode, as shown in in Figure 4.7(b).

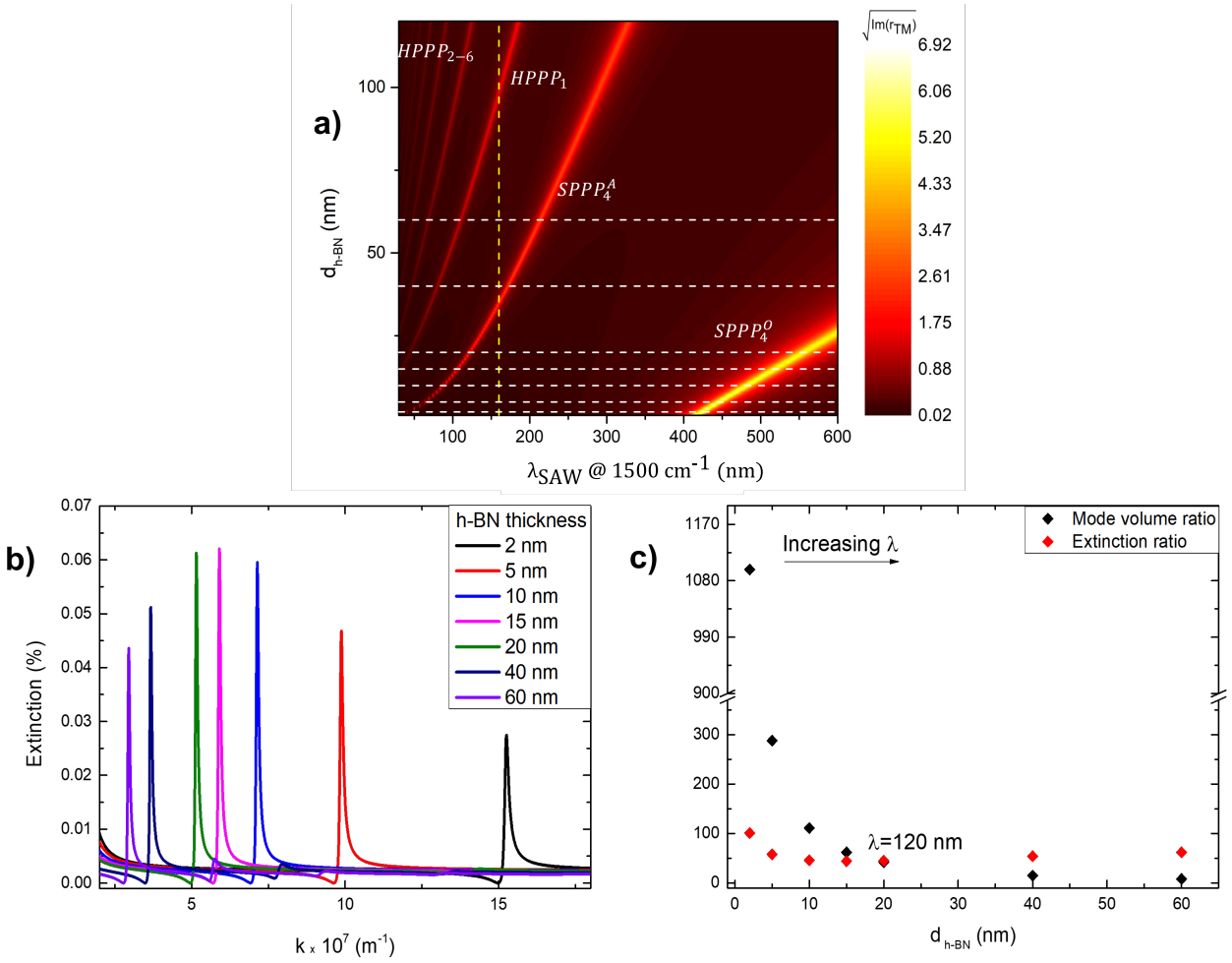

Figure 4.8: **a** Cross section of the polariton dispersion at a frequency of 1500 cm^{-1}. The horizontal white lines mark the h-BN thickness values presented in (b) whereas the vertical yellow line indicates a SAW wavelength of 160 nm, corresponding to the state-of-the-art resolution limit of an IDT. **b** Extinction of the $SPPP_4^A$ mode as a function of the wavevector at a frequency of 1500 cm^{-1} for different values of the h-BN thickness d_{h-BN}. **c** Plot of the mode volume and extinction ratios of the $SPPP_4^O$ mode used in the biosensor described in Section 4.1.3 (for $d_{h-BN} = 2$ nm) and the $SPPP_4^A$ mode achievable for different d_{h-BN} values. Note that the thicker the h-BN layer, the higher the wavelength at which the acoustic polariton is found and that a crossover of the ratios occurs at $\lambda = 120$ nm.

A possible alternative to avoid a drastic reduction in the SAW wavelength is to increase the thickness of the h-BN spacer layer, d_{h-BN}, which brings the acoustic and optical plasmon branches closer in the dispersion by raising the frequency of the former and lowering the frequency of the latter, thus allowing the $SPPP_4^A$ mode to reach 1500 cm^{-1} at a lower wavevector value. In Figure 4.8(a), a cross section of the polariton dispersion at a frequency of 1500 cm^{-1} is shown as a function of d_{h-BN} and the SAW wavelength. It can be clearly

seen that the optical branch $SPPP_4^O$ is far more intense than the branches corresponding to the acoustic $SPPP_4^A$ mode and than the even weaker hyperbolic modes ($HPPP_i$) that arise in the higher energy reststrahlen band of h-BN when increasing d_{h-BN}. The extinction spectra displayed in Figure 4.8(b) show that, by increasing d_{h-BN}, the $SPPP_4^A$ mode becomes more relevant as it shifts away from the intraband transition region. However, this effect reaches a maximum at around $d_{h-BN} = 15$ nm and reduces for higher d_{h-BN} values, since the overlap between the polaritons formed in both DLGs reduces as the distance between them increases. Figure 4.8(c) compares the $SPPP_4^O$ mode used in the biosensor structure discussed in Section 4.1.3 (that is, for $d_{h-BN} = 2$ nm) with the $SPPP_4^A$ modes that can be generated for different d_{h-BN} values. The comparison is based on the ratios of their mode volumes, estimated as $(\frac{\lambda_{optical(2nm)}}{\lambda_{acoustic(d_{h-BN})}})^3$, and of their extinctions, $\frac{Ext_{optical(2nm)}}{Ext_{acoustic(d_{h-BN})}}$. It can be noticed that, for a d_{h-BN} value larger than 20 nm (which leads to a SAW wavelength of $\sim$ 120 nm), the extinction ratio is greater than the mode volume ratio, indicating that the optical mode chosen is more convenient for $\lambda_{SAW} > 120$ nm, which is already below the above mentioned resolution limit for an IDT.

Therefore, since the $SPPP_4^O$ mode presents a higher extinction as compared to its acoustic counterpart within the state-of-the-art lithographic capabilities, only this mode will be considered to probe the vibrational resonances of the analytes.

4.1.3 SPPP-Assisted Fingerprinting

Once the structure of the biosensor has been optimized for operation in the 1500-1700 cm^{-1} frequency range, its performance fingerprinting a thin film of CBP has been simulated. CBP is an organic semiconductor that exhibits three sharp absorption lines in the targeted spectral range: $\omega_{CBP1} = 1449$ cm^{-1} and $\omega_{CBP2} = 1479$ cm^{-1}, related to the deformation modes of the C-H bond located mainly in the carbazole group ($\delta(C-H)_c$); and $\omega_{CBP3} = 1504$ cm^{-1}, originating from the deformation mode of the C-H bond in the biphenyl group ($\delta(C-H)_b$) and the stretching mode of the C-N bond ($\nu(C-N)$) (Huck et al., 2014). This makes CBP a good testbench analyte for the biosensor.

Figure 4.9 shows the dispersion curves for the bare DLG/h-BN/DLG/AlN/Al/AlN sensor heterostructure, (Figures 4.9(a) and (c)), and coated by a 5 nm-thick CBP layer (Figures 4.9(b) and (d)). The comparison of the magnified view of the upper reststrahlen band of h-BN with and without the CBP analyte, shown in Figures 4.9 (d) and (c), respectively, clearly shows anticrossing features proving the coupling between these vibrational resonances and the $SPPP_4^O$ mode (hereafter referred to as simply $SPPP_4$), which allows the biosensor to fingerprint the CBP.

Figure 4.10 describes the operation principle of the DLG/h-BN/DLG/AlN/Al/AlN sensor for fingerprinting the vibrational resonances of CBP. On the one hand, the deposition of CBP layers of increasing thickness leads to a polariton frequency shift induced by the associated change in the dielectric environment, as depicted in Figure 4.10(a) around the vibration $\delta(C\text{-}H)_c$. However, this mechanism only permits to infer the effective refractive index of the analyte (Y. Zhao et al., 2013) but lacks specificity. On the other hand, the interaction between the polariton and the vibrational resonance of CBP leads to small dips at the tails

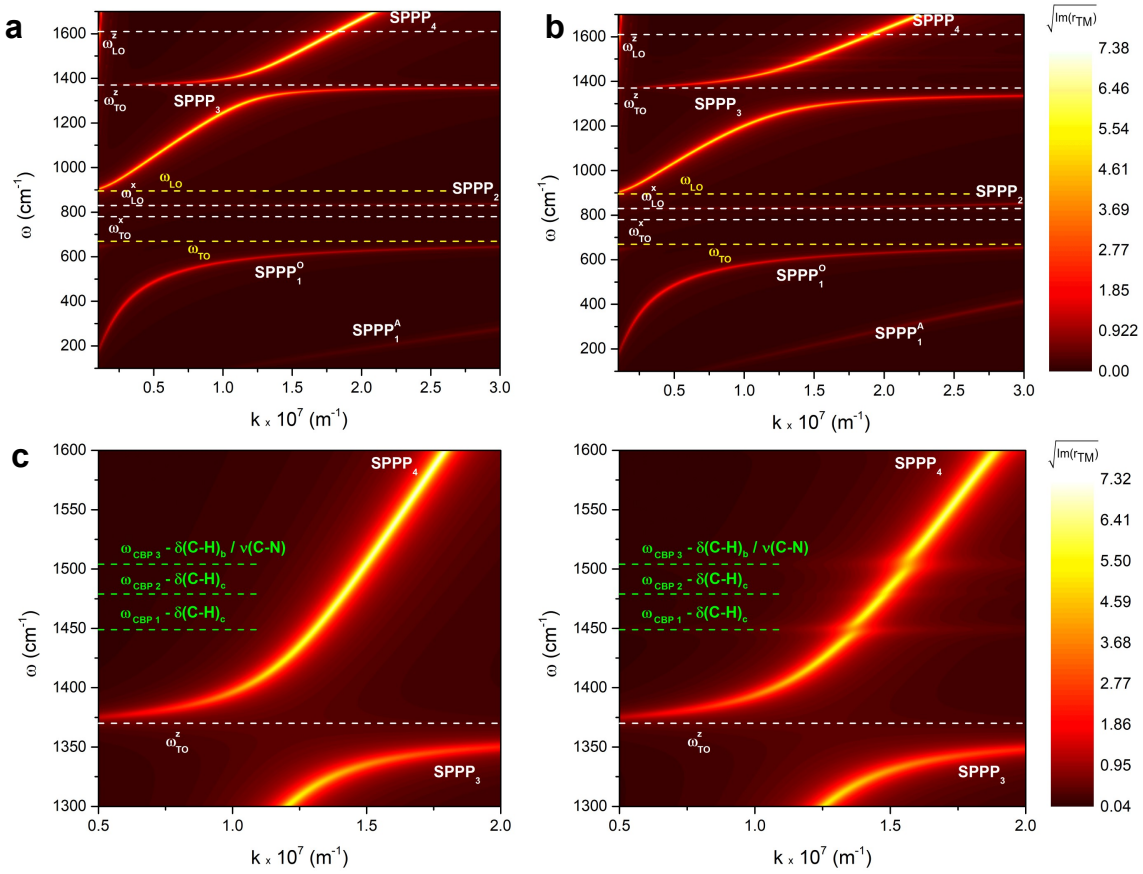

Figure 4.9: Dispersion of the surface plasmon-phonon polaritons $SPPP_i$ for the DLG/h-BN/DLG/AlN/Al/AlN system without **a,c** and with **b,d** a 5 nm-thick CBP layer on top. (c,d) show a magnified view of the CBP fingerprint region in (a,b), respectively. White and yellow dashed lines indicate the optical phonon frequencies of h-BN and AlN respectively, whereas green dashed lines are displayed at the frequencies of the vibrational resonances of CBP. The Fermi energy is $E_F = 0.4$ eV for all graphene sheets and the h-BN layer is 2 nm thick.

of the spectra. Nevertheless, these features are not strong enough to provide the required sensor sensitivity. The specificity, and hence the fingerprinting capability, together with the enhanced sensitivity of the proposed sensor rely on the tuning of the Fermi level of the DLGs via a gate bias, so that the polariton is continuously forced to overlap with the vibrational resonance of CBP, as shown in Figure 4.10(b) for the case of the vibration δ(C-H)$_c$. In this configuration, as the thickness of the analyte layer is increased, two different regimes can be distinguished. Initially, a broadening of the extinction peak is observed that gradually turns into the emergence of a transparency window within the extinction peak at around the frequency of the vibrational transition.

This latter transparency-window regime has been previously reported in different types of polaritonic systems such as metallic antennas (Vogt et al., 2015) and graphene (Li et al., 2014; H. Hu et al., 2016) or h-BN (Autore et al., 2018) nanoribbon arrays, among others